Università degli Studi di Ferrara

DOTTORATO DI RICERCA IN
Scienze dell’Ingegneria

CICLO XXI

COORDINATORE Prof. Stefano Trillo

ADVANCED VIBRATION PROCESSING TECHNIQUES FOR CONDITION MONITORING AND QUALITY CONTROL IN I.C. ENGINES AND HARVESTING MACHINES

Settore Scientifico Disciplinare ING-IND/13

Dottorando
Dott. Delvecchio Simone

Tutore
Prof. Dalpiaz Giorgio

Anni 2006/2008

Università degli Studi di Ferrara
Engineering Department in Ferrara

Dottorato di Ricerca in Scienze dell' Ingegneria
XXI ciclo

Doctoral Program: Engineering
Curriculum: Industrial Engineering
Branch of study: Mechanics of Machines

Title: Advanced vibration processing techniques for condition monitoring and quality control in I.C. engines and harvesting machines
Author: Ing. Simone Delvecchio
Supervisor: Prof. Giorgio Dalpiaz
Printed: March 2009

PhD Coordinator

Prof. Stefano Trillo	Università degli Studi di Ferrara

PhD Jury

Prof. Giorgio Dalpiaz	Università degli Studi di Ferrara, Italy
Prof. Alberto Tiziani	Università degli Studi di Padova, Italy
Ing. Denis Benasciutti	Università degli Studi di Udine, Italy
Prof. Dr. Ir. Paul Sas	Katholieke Universiteit Leuven, Belgium

Final exam
2009 March, 27th

To my grandfather, Bartolomeo,
and my grandmother, Angela.

“Imagination is more important than knowledge”

A. Einstein

Riassunto

L’argomento affrontato in questa tesi riguarda lo sviluppo e l’implementazione di tecniche avanzate di processamento del segnale di vibrazione per il monitoraggio e la diagnostica delle macchine. Due sono i campi di applicazione qui trattati: il controllo di qualità di motori a combustione interna attraverso test a freddo ed il monitoraggio del processo di trebbiatura in macchine mietitrebbie.

Il test a freddo viene condotto alla fine della linea d’assemblaggio del motore. Tale test permette il controllo di qualità finale del motore non acceso ma trascinato. Tecniche per il monitoraggio di motori basate sull’ analisi del segnale di vibrazione sono attualmente utilizzate. Tuttavia queste tecniche sono spesso applicate a segnali estratti da motori durante test a caldo. Questa tesi tratta l’utilizzo di strumenti di analisi del segnale di vibrazione acquisito durante prove a freddo.

Per quanto riguarda il controllo dello stato del motore, viene presentato un approccio basato sull’uso di pattern simmetrizzati per la caratterizzazione visiva dei segnali di vibrazione e per l’ottenimento di valori di soglia utili per discriminare la condizione difettosa da quella sana.

La diagnosi, ossia la localizzazione del difetto all’interno del cinematismo del motore, è affrontata attraverso l’utilizzo del modello ciclo-stazionario del segnale di vibrazione. La componente ciclostazionaria del primo ordine del segnale viene stimata attraverso il calcolo della media sincrona. Successivamente, la componente ciclostazionaria del secondo ordine viene analizzata attraverso la Distribuzione di Wigner-Ville (WVD), lo Spettro di Wigner Ville (WVS) e

la potenza media istantanea (MIP). Inoltre la Trasformata Wavelet continua (CWT) è presentata e comparata con le distribuzioni sopra descritte.

La scelta di diverse ‘mother wavelets’ e alcuni metodi per l’ottimizzazione della mappa tempo-frequenza ottenuta tramite CWT vengono ulteriormente considerati. Inoltre vengono discusse le potenzialità del segnale di velocità angolare istantanea (IAS) dell’albero motore nell’identificazione della presenza di difetti di assemblaggio.

I risultati sperimentali indicano che la correlazione tra immagini ottenute dai pattern simmetrizzati del segnale di vibrazione può essere considerata uno strumento utile per il miglioramento dell’efficienza del test a freddo nel riconoscimento di condizioni difettose.

Viene inoltre verificato che la componente ciclostazionaria del segnale di vibrazione è utile nel riconoscere la presenza del difetto ma non la sua localizzazione.

La componente ciclostazionaria del secondo ordine, invece, permette di superare questo inconveniente localizzando angolarmente il difetto all’interno della catena cinematica biella-manovella-pistone con l’ausilio del diagramma degli eventi del motore. Per quanto riguarda l’analisi tempo-frequenza, la distribuzione WVS e la Trasformata Wavelet calcolata utilizzando la ‘Morlet wavelet’ possono essere considerati utili strumenti di analisi del segnale per localizzare i transitori dovuti alla presenza del difetto nel dominio tempo-frequenza.

Grazie a questa ricerca è possibile capire quale delle tecniche sopra descritte è efficace per effettuare un controllo di qualità semplice e robusto di motori a combustione interna. Inoltre vengono evidenziati i limiti e le problematiche di ciascuna tecnica applicata.

La seconda parte della tesi affronta l’analisi delle relazioni che intercorrono tra le variabili che caratterizzano il processo di trebbiatura in macchine mietitrebbie e la risposta vibratoria delle macchine stesse. Parametri statistici comuni ed avanzati estratti da segnali vibro-acustici sono stati correlati con variabili di efficienza con l’obiettivo di definire un’ insieme ottimale di parametri abili nel monitorare il processo di trebbiatura. La Trasformata Wavelet Discreta (DWT) è stata utilizzata per trovare il range di frequenza di segnali vibratori caratterizzato da componenti impulsive. Vengono inoltre esposti alcuni risultati ottenuti attraverso l'analisi vibro-acustica condotta nel dominio angolare. Due differenti configurazioni di prova sono state messe a punto per acquisire segnali in diverse condizioni operative della macchina trebbiatrice. L'obiettivo è quello di valutare l'influenza di tali condizioni sulla risposta vibratoria della stessa. I risultati ottenuti possono essere utilizzati per capire come la generazione di vibrazione è connessa alla distribuzione del materiale processato dalla macchina durante il processo di trebbiatura.

Buone correlazioni sono state ottenute attraverso l'analisi del segnale misurato dall' accelerometro posto sulla gabbia che avvolge parzialmente il rotore che effettua la trebbiatura attraverso il confronto tra alcuni parametri statistici del segnale di vibrazione con indicatori di efficienza. Questi parametri statistici possono essere assunti come buoni indicatori per descrivere la distribuzione del materiale tra la gabbia ed il rotore e, conseguentemente, l'efficienza del processo.

Il principale ed originale contributo di questa seconda parte della ricerca riguarda l'uso del segnale di vibrazione come strumento efficace per il monitoraggio del processo di trebbiatura. Il segnale di vibrazione può essere considerato come un indicatore di qualità del processo utile all'operatore durante le operazioni di trebbiatura condotte su campo.

Abstract

The topic of this thesis is the development and the implementation of advanced vibration processing techniques for machine condition monitoring and diagnostics with two fields of applications: the quality control of I.C. engines by means of cold tests, and the monitoring and control of harvesting processes.

The cold test, i.e. the final test after the assembly line and before shipping the engine to the customer, consists of the final quality control of the engine in a non-combustion state. Techniques for engine condition monitoring based on the analysis of vibration signals are widely used. However, these techniques are often applied to engine tests in firing conditions. This thesis addresses the use of several signal processing tools as a means for the monitoring and the diagnosis of assembly faults through the cold test technology. Firstly, an approach based on the use of Symmetrized Dot Patterns for the visual characterization of vibration signatures is proposed in order to obtain reliable thresholds for the pass/fail decision after the cold test. Secondly, the fault identification is discussed on the basis of the cyclostationary modelling of the signals. The first-order cyclostationarity is exploited through the analysis of the Time Synchronous Average (TSA). Subsequently, second-order cyclostationarity is analysed by means of the Wigner-Ville Distribution (WVD), Wigner-Ville Spectrum (WVS) and Mean Instantaneous Power (MIP). Moreover, Continuous Wavelet Transform (CWT) is presented and compared with the WVD and WVS. The choice of different wavelet functions and some methods for the CWT map optimization (i.e. purification method and the average across the scale

method (TDAS)) are also considered. Moreover, the capabilities of the Instantaneous Angular Speed (IAS) in detecting assembly faults have been tested.

It is worth noting that the cyclostationary and time-frequency technique capabilities have been verified for both simulated and real signals.

The experimental results indicate that the image correlation of Symmetrised Dot Patterns is a good solution that can be used in the cold test technology in order to increase its efficiency and fault detection capability. Moreover, it will be proved that the first order cyclostationary analysis is able to identify the presence of assembly faults but it is not appropriate to localise the faults. The second order analysis overcomes this problem indicating the angular position of the mechanical part affected by the fault. This is achieved by means of a correlation between the results obtained from the cyclostationarity analysis and the angular position of the mechanical events. Concerning the time-frequency analysis, the WVS as well as the CWT, using both Morlet mother wavelet and TDAS method can be considered good tools to characterise the transients due to the fault events in the time-frequency domain. Thanks to this research study it is possible to understand which of the above-mentioned techniques is effective for an easy and fast quality control and for the diagnosis of the considered assembly faults. Moreover, the limits and drawbacks of both monitoring and diagnostic procedures are shown.

The originality of the first part of the research mainly concerns the use of vibration measurements for the quality control of engines at the end of the assembly line while the greater part of methods used for cold test applications focuses on pressure and torque measurements.

The second part of this thesis concerns the analysis of relationships between the harvesting process parameters relative to a non-conventional harvesting machine and its vibration response.

Common and uncommon features extracted from a segmentation analysis have been correlated with the harvesting process efficiency in order to define the optimal monitoring feature subset. Moreover, the Discrete Wavelet Transform method is performed in order to find the frequency range mostly characterised by impulsive components. In addition, some outlines obtained through the vibro-acoustic analysis performed in the angular domain are also given.

Two different indoor and outdoor test rigs have been built to test the machine under different setting conditions in order to evaluate their influence over the vibration response of the threshing unit. The test results are used to identify how the vibration generation is linked to the crop distribution during the threshing process.

Good correlations have been obtained by analysing the concave middle radial signal and by calculating the relationships that exist between some time domain features and the efficiency parameters. These features can be assumed as good indexes in explaining the crop distribution between the rotor and the concave and, consequently, the efficiency of the process. Moreover, it will be shown that the vibro-acoustic features selected are well-connected to the different sources of the concave excitation.

The main original contribution of this second part concerns the use of the vibration signal as an effective way to monitor the harvesting process. It can also be considered as a proper quality control indicator for the user during field operations.

Acknowledgements

I would like to give a special and sincere thanks to Prof. Ing. Giorgio Dalpiaz, my supervisor, for all his guidance, knowledge, and for the opportunity he gave me. I wish also to thank Apicom and VM Motori (Cento, Ferrara, Italy) and the engineers of these Companies for co-operation and assistance in the collection of engine data. This thesis has been partially developed within the laboratory of research and technology transfer InterMech (Division Acoustics and Vibrations - LAV) realized through the contribution of Regione Emilia Romagna - Assessorato Attivita' Produttive, Sviluppo Economico, Piano telematico, PRRIITT misura 3.4 azione A. The second part of the work is the result of a 9 months research period at Department of Mechanical Engineering at KUL (Katholieke Universiteit Leuven) in Leuven (Belgium) in the framework of the "Marie Curie Host Fellowship EDSVS". I would like to thank the European Commission for the grant received. I am sincerely thankful to Prof. Dr. Ir. Paul Sas for his support and trust he gave me for all the duration of the work. My acknowledgements also go to Dr. Ir. Bart Missotten from CNH and all the academic stuff from the Department of Biomechanics Engineering of KUL for their cooperation and helpfulness.

I am deeply grateful to all people I met during last three years and to my Italian and Belgian colleagues who enriched my experience. Friends, more than colleagues.

Simone,
Ferrara, March 2009.

Preface

In October 2005 I graduated in Mechanical Engineering and I discussed Machine Design in my thesis. I immediately started to work for a company producing forklift trucks. I was really surprised when I received the call from my current supervisor, Prof. Giorgio Dalpiaz, who suggested I followed a Ph.D. on the use of vibration analysis techniques for machines monitoring and diagnostic purposes. Although it was the first time that I had approached this subject, I decided to accept this opportunity without hesitation.

Just a short time was needed to realise the stimulating features of this research field. My new Ph.D. activity developed from the results published by Dalpiaz, Rivola and Rubini in 2000. Based on these results, concerning the comparison of the effectiveness and sensitivity of some vibration processing tools for local fault detection in gears, I first proposed the study of non-stationary processing techniques for the detection of assembly faults in I.C. engines by means of cold tests.

After reading some literature papers, I realised the originality of this application.

Hence, the common thread of the research was characterised at once by the study, application and assessment of some non-stationary signal processing techniques, with wavelet transform as the prime mover. This research activity, which has been carried out in cooperation with APICom and VM Motori (Cento, Ferrara, Italy), is described in the first part of this thesis and in the following publications:

[1] S. Delvecchio, G. Dalpiaz, O. Niculita, A. Rivola, *Condition monitoring in diesel engines for cold test applications. Part I: vibration analysis for pass/fail decision,* in Ana C V Veira et oth. editors, Proceedings of the 20th International Congress & Exhibition on Condition Monitoring and Diagnostic Engineering Management, Faro, Portugal, 2007 June 13-15, pp.197-206.

[2] S. Delvecchio, G. Dalpiaz, O. Niculita, A. Rivola, *Condition monitoring in diesel engines for cold test applications. Part II: comparison of vibration analysis techniques*, in Ana C. V. Veira et oth. editors, Proceedings of the 20th International Congress & Exhibition on Condition Monitoring and Diagnostic Engineering Management, Faro, Portugal, 2007 June 13-15, pp.197-206.

[3] O. Niculita, D. Zetu, S. Delvecchio, *Contribution regarding the link between total productive maintenance and product quality,* in Proceedings of International Conference "Modern Technologies, Quality and Restructuring-TMCR 2007", ISBN 978-9975-45-034-8, Chisinau, Moldova, May 31-June 3 2007.

[4] O. Niculita, D. Zetu, S. Delvecchio, *A methodology for diesel engines health monitoring,* in Proceedings of International Conference "Modern Technologies, Quality and Restructuring-TMCR 2007", ISBN 978-9975-45-034-8, Chisinau, Moldova, May 31-June 3 2007.

[5] O. Niculita, S. Delvecchio, D. Zetu, *Online diagnosis over internal combustion engines using visual dot patterns of vibration signals.* in Optimum technologic systems and materials in the machines building field, TSTM- No.12 , Volume II (2006) ISSN 1224-7499, University of Bacau, Romania, 2006.

[6] D. Zetu, O. Niculita, S. Delvecchio, *Implementation of image matching correlation of symmetrized dot pattern of vibration signals in fault diagnosis cold test method for diesel engines.* in Optimum technologic systems and materials in the machines building field, TSTM- No.12 , Volume II (2006) ISSN 1224-7499, University of Bacau, Romania, 2006.

[7] O. Niculita, S. Delvecchio, D. Zetu, *Effect of lag on the symmetrized dot pattern (SDP) displays of the vibration signal of diesel engines* in Optimum technologic systems and materials in the machines building field, TSTM- No.12 , Volume II (2006) ISSN 1224-7499, University of Bacau, Romania, 2006.

[8] S. Delvecchio, G. D'Elia, G. Dalpiaz, *Comparing Wigner Ville Distribution and Wavelet Transform for the vibration diagnosis of assembly faults in diesel engines,* in Proceedings of the 21th International Congress & Exhibition on Condition Monitoring and Diagnostic Engineering Management 2008, Prague, Czech Republic, 2008 June 11-13, pp. 125-134.

[9] S. Delvecchio, G. D'Elia, M. Cavallari, G. Dalpiaz, *Use of the cyclostationary modelling for the diagnosis of assembly faults in I.C. engine cold tests,* in P. Sas, B. Bergen editors Proceedings of ISMA2008 International Conference on Noise and Vibration Engineering, Leuven, Belgium, 2008 September 15-17, pp. 3191-3204.

[10] S. Delvecchio, G. D'Elia, G. Dalpiaz, *Application of advanced vibration signal processing techniques in I.C. engine cold tests*, in U. Meneghetti, A. Maggiore and V. Parenti Castelli editors Memorie della Seconda Giornata di Studio "Ettore Funaioli", Bologna, Italy, 2008 Luglio 18.

I spent a 9-month-research period at the Department of Mechanical Engineering at KUL (Katholieke Universiteit Leuven) in Leuven (Belgium) within the Noise and Vibration research group. The research activity I carried out during my stay in KUL concerned the use of vibro-acoustic techniques to evaluate the efficiency of the threshing process in non conventional harvesting machines. The idea was to evaluate the influence of the most important factors affecting the process on the vibro-acoustic response of the threshing unit. The objective was to define the best machine setting to improve the quality of the crop. The research to find some correlation among several vibro-acoustic features and "quality" parameters was another goal of this thesis. The methodology and the results of this activity are summarised in the second part of this thesis and in the following technical report:

[11] S. Delvecchio, *Condition monitoring of the threshing process in harvesting machines by means of vibro-acoustic analysis*. Technical Report, Katholieke Universiteit Leuven, Department of Mechanical Engineering, PMA Division, Noise and Vibration Group, (MOD), 2008 March 7.

Moreover I was involved in other research activities in the field of diagnostics of rotating machines by means of vibration analysis. These activities and the achievements obtained are described in the following papers:

[12] S. Delvecchio, G. Dalpiaz, E. Mucchi. *Condition monitoring of marine couplings through vibration analysis techniques*, in Proceedings of the Second World Congress on Engineering Asset Management and the Fourth International Conference on Condition Monitoring 2007, Harrogate, UK, 11-14 June 2007, pp. 506-515.

[13] G. D'Elia, S. Delvecchio, G. Dalpiaz, *Gear spall detection by non-stationary vibration signal analysis,* in P. Sas, B. Bergen editors Proceedings of ISMA2008 International Conference on Noise and Vibration Engineering, Leuven, Belgium, 2008 September 15-17, pp. 777-792.

The first paper shows the application of some processing techniques for the vibration analysis in working conditions of two different types of marine flexible couplings for boat propulsion. Due to the presence of impulses in the signals, Continuous (CWT) and Discrete Wavelet Transform (DWT) are applied and compared with the conventional time and frequency domain methods. In this thesis the wavelet analysis was used for impulsive component extraction and the choice of different wavelet functions was evaluated for this purpose. The results suggested that the wavelet transform techniques were effective in the indication of which type of coupling provided good vibrational behaviour, especially in working conditions when the angular speed of the propeller shaft was often inverted.

The second paper relates to the diagnosis of gear local faults by non-stationary signal analysis such as CWT, Wigner-Ville Distribution (WVD) and cyclostationary analysis. The results indicated the sensitivity of each technique to extract faults in simulated and real signals.

Finally, another activity that I carried out during my PhD course was the design of a test bench for the vibro-acoustic analysis of rotating machines for educational and research purposes, as described in:

[14] G. Dalpiaz, G. D'Elia, S. Delvecchio. *Design of a test bench for the vibro-acustical analysis and diagnostics of rotating machines.* In Proceedings of the Second World Congress on Engineering Asset Management and the Fourth International Conference on Condition Monitoring 2007, Harrogate, UK, 11-14 June 2007, pp.497-505.

The ability of the bench to change different configurations easily makes it useful to carry out a great number of experiments concerning the vibrations produced by gears and rolling bearings in sound conditions and with different types of faults, as well as misalignments between shafts, static and dynamic unbalance and critical speeds.

This thesis gathers and summarises the theories, results and considerations that I have draw in the three years of my Ph.D. course, on the topic of condition monitoring and quality control in I.C. engines and harvesting machines by means of advanced vibration processing techniques. I hope these theories, results and considerations will be useful for future students and other researchers working in the field of vibration signature analysis.

Ferrara, 27/3/2009

Simone Delvecchio

List of Abbreviations

AR	Autoregressive
AppEn	Approximate Entropy
CF	Crest Factor
CWT	Continuous Wavelet Transform
CRM	Faulty engine with wrong assembly of counter-rotating masses
CT	Correlation Threshold
BDC	Bottom Dead Centre
DSP	Digital Signal Processing
DWT	Discrete Wavelet Transform
FFT	Fast Fourier Transform
IAS	Instantaneous Angular Speed
IF	Impulse Factor

MIP	Mean Instantaneous Power
MOG	Material Other than Grain
PDF	Probability Density Function
PM	Phase Modulation
PSD	Power Spectral Density
RMS	Root Mean Square value
RC4	Faulty engine with rod without bearing cap
RS3	Faulty engine with rod not correctly pre-loaded
SCD	Spectral Correlation Density
SDP	Symmetrized Dot Pattern
SK	Spectral Kurtosis
SNR	Signal to Noise Ratio
STFT	Short Time Fourier Transformation
TDAS	Time Domain Across the Scales
TDC	Top Dead Centre
TK	Temporal Kurtosis
TSA	Time Synchronous Average
WV	Wigner Distribution
WVD	Wigner Ville Distribution
WVS	Wigner Ville Spectrum

CONTENTS

Chapter 1
INTRODUCTION

Chapter 2
SIGNAL PROCESSING TECHNIQUES

Chapter 3
CONDITION MONITORING AND DIAGNOSIS IN I.C. ENGINE COLD TESTS

Chapter 4
CONDITION MONITORING OF THE THRESHING PROCESS IN HARVESTING MACHINES

List of Figures

Chapter 1
INTRODUCTION

1.1 What is this thesis about?

This thesis deals with the problem of condition monitoring and diagnostics in I.C. engines and harvesting machines by means of vibration signature techniques.

Concerning the issue of I.C. (Internal Combustion) engine quality control, three main questions are posed:

- Are the vibration measurements obtained from the **cold tests** useful in **detecting** assembly faults in diesel engines?
- Is it possible to assess a fast and reliable **monitoring procedure** to make a correct pass/fail decision at the end of the engine assembly line?
- Which is the most effective technique to **diagnose** malfunctions (not common in literature) in engines by means of the analysis of vibration signals carried out in a non-combustion state?

Concerning the harvesting process condition monitoring, the three main questions are the following:

- What do the **concave vibrations** tell about the threshing process?

- How are the vibrations **correlated** to the threshing/separation process?
- Can we use information from vibrations to predict the **efficiency performances**?

1.2 Vibration condition monitoring and diagnostics

The purpose of condition monitoring is to use information extracted from the vibro-acoustic signature of a machine to detect faults or to define its state of health. A change in the vibration signature not only indicates a change in machine conditions but also points directly to the source of the signal alteration.

Fault diagnosis, condition monitoring and fault detection are different terms sometimes used improperly. Condition monitoring and fault detection refer to the evaluation of the state of a machine and the detection of the anomaly. Fault diagnosis could be separated from the others because it is more rigorous and requires the identification of the component or process that causes the machine's deviation from the normal state.

In each chapter of this thesis the term "signature' will be mentioned many times in order to stress its fundamental role in describing the state of the machine. Since it is impossible to quantify the amount of information collected in the vibration signature of a machine, the aim of this work is to extract and relate some of this information to the components or operational factors that produce significant alterations within the signal.

Because of its non-intrusive behaviour and ability in diagnosing a wide range of mechanical faults, the vibration monitoring techniques are commonly used by manufacturing companies. Moreover, the increase of computing power has helped the employment and development of signal processing techniques.

Firstly, the monitoring procedure involves the acquisition of vibration signals by means of piezo-electric accelerometers. Because of the critical selection of the acquisition parameters, the data acquisition step is not of minor importance. Sometimes, several operations, like correct selection of time histories, averaging and digital filtering are needed in order to separate the useful part of the signal from the noise (electrical an mechanical), which is often present in the industrial environments.

Secondly the signal processing techniques have to be implemented by taking into account the characteristics of the signal and the type of machine from which the signal is being measured (i.e. rotating or alternative machine with simple or complex mechanisms).

Eventually, several features have to be extracted in order to assess the physical state of the machine or to detect some incipient defects and to determine the causes of their presence.

Concerning the I.C. cold tests engine application the signature processing techniques can be used in order to obtain a reliable pass/fail decision for the quality control of the diesel engines at the end of the assembly line. Moreover, some vibration analysis tools can be considered useful in indicating the mechanical part affected by the defect.

Regarding the threshing process application, condition monitoring can be used for the following purposes: to extract not redundant features physically related to the nature of the signal measured on combine harvesters; obtaining meaningful correlations between the vibration features and efficiency parameters (i.e. losses and quality of the crop) in order to validate an automatic procedure of feature selection; achieve information about the influence of the operational parameters (i.e. rotor speed, concave distance and amount of crop processed) that mostly influence the process.

1.3 I.C engine cold tests

Nowadays, the main part of engine manufacturers test their engines by means of a “hot test”, i.e. a test in which the engine is firing. On the other hand, recently, some companies have instead chosen to introduce a “cold test”, but this method has to be further improved.

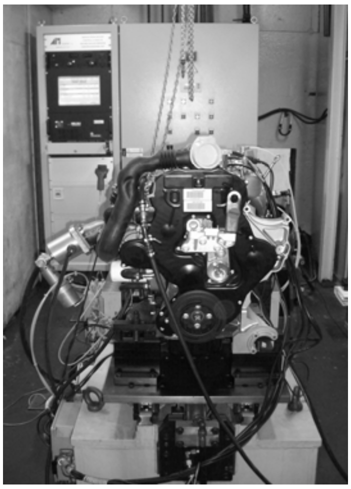

Fig. 1.1 – Cold test bench and data acquisition system.

The essential difference between these two methods is that the hot test aims at verifying the engine performance, while the cold test aims at verifying the anomalies by means of torque, pressure and vibration measurements.

It is worth noting that in the hot test only the main anomalies could be detected, while in the cold test the fault detection is more precise and effective, since no noise and vibration due to the firing are added.

In the “hot test”, each engine must be connected to a test bench. This test bench includes a brake, provides the cooling (water, oil) and connects to the other auxiliary services in working condition as fuel, gas and air. For this reason, a complete hot test procedure takes more than ten minutes. At present, the hot test technology only indicates to the manufacturer which engines are not good for customers, but does not give any more information regarding the causes of the fault producing the malfunction.

The introduction of this technology decreases the noise produced during the test as well as the number of personnel involved, which reduces the costs of testing and fast detection of faults and of their causes.

As it is well-known, mechanical faults in machines often show their presence through abnormal vibration signals, thus techniques for machine condition monitoring based on the analysis of these signals are widely used [1]-[8].

However, most of the studies have been carried out on simple mechanical parts, such as gears and rolling bearings, having well-determined dynamic characteristics. Therefore, gearbox condition monitoring and bearing defect analysis using vibration signatures are extensively reported [9]-[15]. Moreover, some works related to the condition monitoring of the drilling process are present in literature [16]-[18].

Vibration of reciprocating machinery such as internal combustion engines, compressors and pumps is far more complex and difficult to analyse. Moreover, the analysis of vibration signals of I.C. engines is affected by the complexity of the engine; some useful information can be deduced by Wowk [4] that "*excessive vibration on reciprocating engines can be caused by operational problems such as misfiring, piston slap, compression leaks, faulty fuel injection and valve clash*".

Therefore, each type of fault may produce a different vibration signature which can be detected by means of proper signal processing techniques.

Generally speaking, fault detection and the diagnosis of I.C. engines can be carried out using different strategies. One strategy can consist of modelling the whole mechanical system using lumped or finite element methods in order to simulate several faults and compare the results with those found through the experimental tests. Another strategy can adopt signal processing techniques in order to obtain features or maps that can be used to detect the presence of the defect. Concerning this, a decision algorithm is needed for a visual or automatic detection procedure. Moreover, the maps can also be also analysed for diagnostic purposes. This method is the most commonly used and well suited for the judgment of expert technicians.

Most of the work in literature, concerning the above-mentioned strategies, refers to engines in firing condition.

Kimmich et al. proposed a model-based diagnosis method [19]. Hugh Thomas et al. developed a diagnostic method to detect engine knock using pattern recognition with wavelet networks [20]. Molinaro et. al. used some pattern recognition detectors, such as cepstral coefficients and amplitude histograms, in order to improve knock recognition in spark engines [21]. Li et al. used the Independent Component Analysis to decompose noise signals into a number of independent components and, consequently, study each individual component separately [22].

Antoni et al. [23]-[24] proposed a methodology based on the properties of cyclostationarity that was applied to the malfunctions related to engines in firing (advance and delay of injections, misfires and knocks). In one of their papers they use the vibration signal to derive the cylinder pressure overcoming the issue of fixing pressure transducers to the engine. Zouari et al. applied the cyclostationary modelling to signals measured from reciprocating compressors [26].

The application of time-frequency distribution techniques is well suited for the analysis of non-stationary signals and has been widely applied to engine monitoring. The Short-Time Fourier Transform (STFT), the Wigner-Ville Distribution (WVD) and the Continuous Wavelet Transform (CWT) were used in order to distinguish faulty conditions from normal ones for practical fault diagnosis and not to obtain reliable parameters for an automatic procedure led by a data acquisition system [27]-[30]. In particular, Liu and Ling [31] proposed a novel method for extracting features from vibration signatures of a diesel engine using wavelet packets. They were able to extract the wavelets that contain maximum information about the induced fault condition.

Some approaches have been introduced by applying the measurement of instantaneous angular speed for detection of fuel leakage in engines in firing [32]. Yang et al. use the instantaneous angular speed to detect faults relating to the gas pressure in the cylinder [33].

All these techniques are often applied for tests on engines in firing conditions. Moreover, all these methods, based on standard and advanced techniques, are effective for the manual analysis based on meaningful comparisons among vibration signatures or patterns obtained from these signatures.

Accurate comparisons require extensive experience usually acquired at the cost of less production efficiency. Moreover, a degraded product quality may be obtained due to mistakes in judgments.

The use of vibration measurements for the purpose of condition monitoring in end-testing is most commonly practiced by gearbox manufacturers. Usually, as said before, the measurements are shown graphically and are analysed manually by a technician.

On the other hand, engine industrial manufacturing testing requires automatic analysis: vibration is measured and some features have to be set in order to classify a condition as pass/failure.

Hence, this thesis aims to investigates the problem of obtaining reliable features for the pass/ fail decision. Then it seeks to obtain a robust diagnostic procedure in order to detect the cause of the possible malfunction.

1.4 The threshing process in non-conventional harvesting machines

The combine harvester, or simply combine, is a machine which "combines" the tasks of harvesting, threshing and cleaning grain plants [34]. The desired result is the seed or grain (including corn, soybeans, flax, oats, wheat, or rye among others).

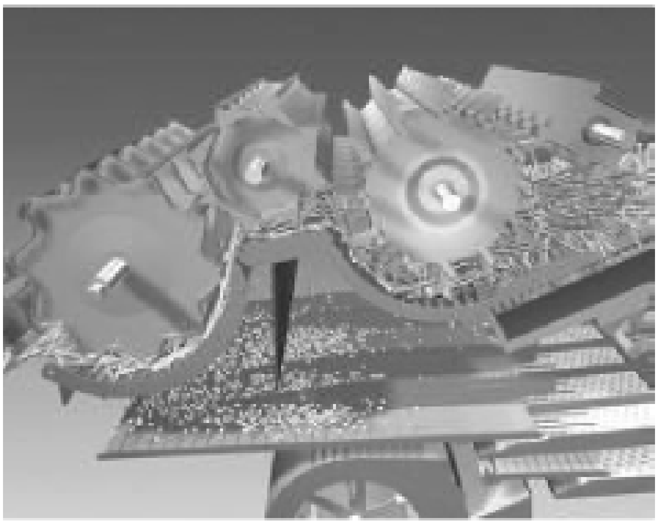

Fig. 1.2 – Frontal rotors in conventional combine harvesters.

For a considerable time, combine harvesters used the *conventional design*, in which three rotating cylinders at the front-end knocked the seeds out of the heads. The rest of the machine was used to separate the straw from the chaff, and the chaff from the kernels.

Since the threshing and separation processes are more related to the centrifugal force and less to gravity, the adoption of the *non-conventional design* was needed.

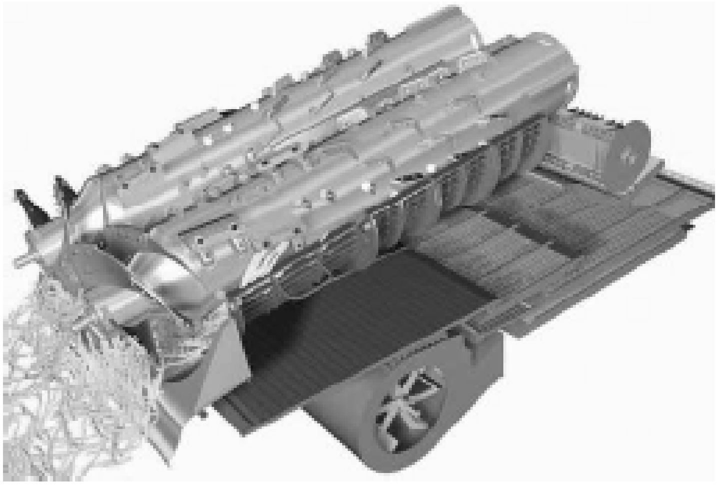

Fig. 1.3 – Longitudinal rotors in non-conventional combine harvesters.

By the early eighties, most major manufacturers had settled on the non-conventional design. More advantages were obtained in terms of faster grain harvesting and gentler treatment of fragile seeds. In fact the faster rotational speeds of the previous conventional threshing cylinders caused the kernels to break.

High threshing efficiency and better kernel separation are the major characteristics of the non-conventional "two rotor" technology (see Fig. 1.3).

The main basic functions performed by the non-conventional harvester are the following:

- The cutting of the crop and the collection of the moved crop material (1);
- The threshing (2) and separation (3) of kernels from the straw;
- The cleaning process (4) to separate kernels from other small particles such as chaff and short straw;
- The temporary storage of clean crop material in the grain bin (5).

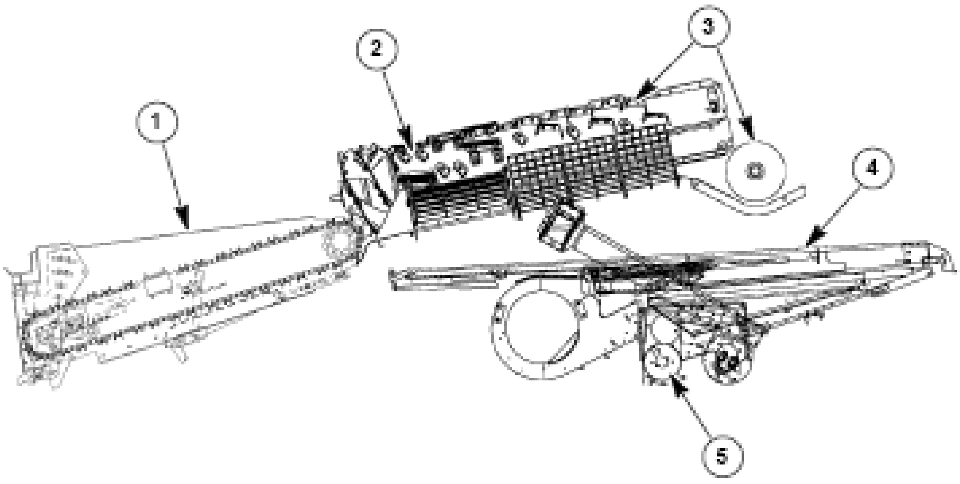

Fig. 1.4 – Five combine harvester functions.

As the crops enter between the rotors and the large concave, spirally mounted rasp bars rub the grains out.

An helicoidally flux of the crop is formed by the two rotors. It is worth noting that the threshing path is more than ten times multiplied more than the one obtained by means of the previous conventional technology.

The threshing process is given by two principal effects:

- the "grain to grain” effect (i.e. the threshing of the grain kernels among themselves);
- the threshing between the kernels and the concave.

The grain to grain effect allows high grain quality to be obtained with less broken kernel grains.

The rasp bars and the friction elements mounted on the rotors favour the friction of the crop against the concaves.

Moreover, the concave is huge and offers the possibility of continuous separation: repeated agitation of the crop by the rasp bars and friction elements offers an uninterrupted threshing process.

A more detailed explanation of the mechanical components and their function will be given in the next Chapter 4.

Several factors have relevant influence over the process. They can be summarised as follows:

- environmental crop conditions;
- crop variety;
- setting of cutter bar;
- grain to straw ratio (i.e. length of the plant);
- rotor speed;
- ground speed;
- concave clearance (radial distance between concave and rotor);
- total amount of crop material entering the machine (capacity).

In Chapter 4 a more specific description of the quality indicators for the threshing process and the procedure for their determination will be given.

So, it is easy to understand that since there is the "grain to grain effect" when capacity increases the threshing efficiency increases. Moreover, a faster rotor speed and a lower concave clearance assure a improved crop separation (the centrifugal force consequently increases) but make the threshing more aggressive, causing inferior crop quality.

In conclusion, we assume the following parameters as the most important useful indicators, which can be used for the evaluation of the quality of the threshing process.

- loss amount;
- kernel integrity;
- distribution of crop on the pan and upper sieve.

Most of the studies carried out in condition monitoring of industrial processes concern production processes, such as papers related to the classification of cutting tool wear and the monitoring of the mechanical assembly of parts, while applications on the threshing process do not exist in literature. Only [35] showed some results about conventional machines.

1.5 Aims and methodologies of the research

The first part of this thesis deals with the analysis of vibration signatures obtained from diesel engines during cold tests.

Since the cold test imposes a pass/fail decision comparing vibration features with proper threshold values, the effectiveness of some features obtained from image correlations of the Symmetrized Dot Pattern of the vibration signal (SDP) is discussed. By means of this method, the normalized time histories of the vibration signal can be represented as symmetrized dot graphs. In order to implement this technique in the cold test procedure for fault detection, an image correlation system has been developed, applying the algorithm of the edge detection that represents the most common approach for detecting meaningful discontinuities in intensity values. The basic idea behind the edge detection is to find the points where the intensity rapidly changes. The goal is to identify a reference pattern that represents the normal condition and then compare the images obtained from all the test engines with this ‘healthy pattern’ by means of a similarity parameter. Among many possibilities, this parameter, called correlation, was chosen as the percentage of common white pixels with respect to the total number of white pixels in the healthy engine pattern.

For fault diagnostic purposes the author seeks to obtain accurate event identification, taking the advantages of the cyclostationary modelling of the vibration signal. First of all, first-order cyclostationarity is exploited through the analysis of the Time Synchronous Average (TSA). Subsequently, second-order cyclostationarity is developed by means of Wigner-Ville Distribution (WVD), Wigner-Ville Spectrum (WVS) and Mean Instantaneous Power (MIP).

Additionally, a correlation between the results obtained from the cyclostationarity analysis and the angular position of the mechanical events is carried out in order to detect and localize the presence of the faults. In order to make quantitative evaluations about the cyclostationary analysis capabilities, a signal model, which mimics the realistic vibration signal measured from the cold test, has been analytically formulated.

Moreover, the Continuous Wavelet Transform (CWT) has been presented and compared with the Wigner Ville Distribution. Some CWT enhancements in terms of choice of different wavelet functions, purification method and Time Domain Average across the Scale (TDAS) have also been applied and discussed. The analysis of the Instantaneous Angular Speed (IAS) obtained after the synchronization with the crankshaft revolution has also been carried out in order to test its capabilities in assembly fault detection. The effectiveness and the limitations of the above-mentioned techniques and diagnostic procedures applied to the considered assembly faults have been compared and discussed on the basis of experimental results.

The second part of the thesis deals with the extraction of several features from vibration and microphone signals acquired from the threshing unit of a harvesting machine and the evaluation of their effectiveness in obtaining useful information for condition monitoring purposes. Thus, the aim of this part is the selection of appropriate features from different signals and their capability in explaining the mechanisms of the noise and vibration generation during the threshing process.

Some common and uncommon (i.e. impulse factor and approximate entropy) features have been extracted from several time blocks of the vibration signal. Some data pre-processing such as band-pass and multiband filtering of the time domain signals have been carried out in order to extract more reliable features.

In order to validate the effectiveness of these features and to point out the effects of the different source of excitations (turbulence due to grain on grain threshing and impacts between the kernels and the concave) the Discrete Wavelet Transform (DWT) has been used to filter the original signal: its capability in extracting impulsive components from the signal has been verified.

The rotor crop distribution and, consequently, the efficiency of the process is strongly influenced by a series of operational parameters. The factors that have the major influence on the process are: the environmental crop conditions, such as moisture, the variety of the crop (wheat and corn have been tested), the grain to straw ratio, the ground and rotor speed, the concave distance (radial distance between the concave and the rotor) and the capacity.

Therefore, the experimental tests have been carried out to obtain good correlation between the features, the above-mentioned operational parameters and threshing efficiency variables (total loss, separation and threshing loss, integrity of the kernels, distribution of the crop over the threshing zone). Some of the threshing efficiency variables have been obtained directly from measurements (i.e. losses), others from probability function calculations (i.e. distribution of the crop over the threshing zone).

Finally, the evaluation of the rasp bar actions (i.e. mechanical parts fixed to the rotor and used to reinforce the threshing action) is carried out by means of the angular domain analysis of the vibration signals measured from the rotor concave. The Hilbert Transform based frequency demodulation technique have also been applied and discussed.

1.6 Overview of the Thesis

Chapter 2 introduces the essential signal processing theoretical background exploiting the formulation of each techniques used in this thesis. Firstly, the mathematical definitions of the time domain features and their physical meaning are described in order to justify their use within the condition monitoring procedure.

Secondly, the well known method in relating the temporal and frequency structure of a signal based on the analytic signal derived using the Hilbert transform is formulated, pointing out its capability to reveal the amplitude modulation and instantaneous phase and frequency of a signal.

Thirdly, two time-frequency techniques, i.e. Continuous Wavelet Transform (CWT) and Wigner Ville Distribution (WVD), are explained, highlighting their effectiveness in overcoming the limitation in resolution of the Short Time Fourier Transform. Two types of mother wavelets are defined such as the Morlet wavelet and the Impulse wavelet. Moreover, the correlation purification method using Morlet and Impulse wavelets is explained: the CWT coefficients are weighted by a coefficient of correlation between the original signal and the sinusoidal function with the frequency corresponding to the wavelet scale. This technique allows a visual enhancement of the transform map.

The WVD is also considered as a cyclostationary analysis tool used to analyse the second order cyclostationary content of the raw signal. Its fundamental properties and some useful statistics extracted from it, such as the Mean Instantaneous Power (MIP), are highlighted.

Chapter 3 is devoted to the description of the results concerning the signature analysis carried out in cold tests on diesel engines. Firstly the characteristics of the cold test technology, the experimental apparatus, the test conditions, the data acquisition system and the artificially introduced faults are described. Then, the results achieved by means of the SDP detecting method, the application of the cyclostationary modelling to a synthesised signal and the comparison between the results obtained through CWT and WVD techniques are also given.

Finally, the cyclostationary capabilities in localising faults and several CWT enhancements (i.e. use of the Impulse mother wavelet, purification and TDAS methods) are discussed on the basis of controlled experimental tests.

Chapter 4 treats the results obtained from the vibration analysis carried out on the harvesting machine. First, the experimental setup designed in order to measure the vibro-acoustic response of the threshing unit is firstly presented. Then, the estimation of the efficiency parameters, such as threshing losses, separation losses, total losses, MOG (Material Other than Grain), distribution of the grain over the sieve and broken grain percentage is exploited. Finally, the results achieved in applying different signal processing tools and the discussion about how the signals are sensitive to the setting parameters and the process efficiency are outlined.

Chapter 5 summarises the achievements and the concluding remarks. The future perspectives are finally proposed.

Chapter 2

SIGNAL PROCESSING TECHNIQUES

2.1 Introduction

As shown in the Chapter 1, the literature on I.C. engine fault detection is quite rare although a lot of work was carried out in the area of rotating machinery fault detection.

As a matter of a fact, most of the studies have been carried out on simple mechanical parts, such as gears and rolling bearings and no applications to the monitoring of I.C. engine cold test exist. Similarly, there is not mention in literature about the use of the vibration signal to evaluate the efficiency of the threshing process in harvesting machines.

This thesis is an attempt to apply some basic and advanced signal processing techniques in order to study their limits and capabilities in extracting useful information from the vibration signal in hand.

In the next section, an overview of the theoretical background of all the techniques adopted in this work is presented.

The choice of the adopted techniques has been guided by the following questions:

- What is the nature of the measured vibration signal: does it exhibit periodicities or is it random in nature? Is it stationary or non-stationary?

- What techniques have been used conditionally to the nature of the signal? Which is the proper domain of study: time, frequency or joint time-frequency domain?
- Which information can be extracted from the signal by the use of each technique? How effective are the chosen techniques?

So, assumed that the type of signal to be analyzed has an influence on the type of analysis to be carried out, it is of relevant importance to examine the various types of signal that are encountered in practice.

Rigorously, random signals have been described mathematically by using the theory of probability, random variables, and stochastic processes, which are not the aim of this work, but a complete stochastic signal analysis can be found in [36] and [37].

The typical classification of signals considers [38][39]:

- Stationary signals;
- Non stationary signals.

The **stationary** signals are characterized by time-invariant averaged properties and thus independent of the particular sample record used to determine them. This applies to both *deterministic* and *random* signals. In particular, a *random* signal $x(t)$ is called wide-sense stationary if the first order (i.e. mean) and second order (i.e. covariance) statistics of its PDF (i.e. Probability Density Function) are time-independent. If all moments (or cumulants) of the PDF are time-independent, then the random signal $x(t)$ is strict-sense stationary.

Since a **non-stationary** *random* signal is a signal the statistical structure of which changes as a function of time, it can be defined as a signal which satisfies a non-property, the property of non-stationarity. Non-stationary signals may be divided into continuous non-stationary signals and transient signals which may be defined as those which start and finish at zero. It is interesting to look at another particular class of non-stationary signals that includes the so-called **cyclostationary** signals, recently investigated by Antoni in the area of condition monitoring of rotating machinery [89].

Analysis of stationary signals has largely been based on time domain techniques and on the Fourier Transform, which identifies the constituent frequency components within the signals. Sections 2.2 and 2.3 treat some concepts concerning the time and frequency domain analysis respectively.

Although the Fourier Transform can be used in analysing signals with periodic impulses (giving rise to uniformly spaced harmonics and sidebands), the time-averaging approach adopting in the Fourier Transform is ineffective in evaluating the time-dependent behaviour of the frequency components.

In contrast, time-frequency techniques decompose one-dimensional time-series signal into a two-dimensional plane by exposing the time-dependent variations of characteristic frequencies within the signal, thus presenting a valid and effective tool for non-stationary signal analysis than the Fourier Transform. In addition to the classical Short Time Fourier Transform (STFT) - which presents uniform resolution in both time and frequency domains - other time-frequency analysis techniques, such as Continuous Wavelet Transform (CWT), Discrete Wavelet Transform (DWT) and Wigner Ville Distribution (WVD) have been recently developed. The capabilities and the drawbacks of these techniques are explained in the Section 2.4. Then, the properties of the cyclostationary techniques are exploited in Section 2.5.

The last Section 2.6 includes the concept of Spectral Kurtosis (SK) applied to the extraction of non stationary components within a signal.

2.2 Time domain analysis

2.2.1. Time statistical parameters

The time series of a signal can yield a big amount of information. A visual inspection of the portions of the time domain waveform can reveal the nature of the signal (i.e. stationary or non-stationary) and the presence of some intrinsic periodicities.

Simple signal metrics applied to the measured time domain signal can give some useful information which cannot be extracted from other domain analyses. Moreover, time domain metrics are cheap and simple to implement and they can be determined through the Probability Density Function (PDF).

It is worth noting that they cannot be used to directly indicate the locations of the defect.

Hence, for fault detection purposes, we can refer to:

- energy parameters;
- peakedness parameters.

The Root Mean Square value (RMS) is a energy dimensional parameter reflecting the overall level of the signal.

The Crest Factor (CF), Temporal Kurtosis (TK) and Impulse Factor (IF) are non-dimensional parameters that indicate the peakedness of a signal.

The **Crest Factor** (CF) is equal to the peak amplitude of a waveform divided by the RMS value. It is defined as follows:

$$CF = \frac{Peak}{RMS} \tag{2.1}$$

The purpose of the CF calculation is to give a quick idea of how much impacting is occurring in a waveform. CF is a normalized measurement of the amplitude of the signal and is designed to increase in the presence of a small number of high amplitude peaks.

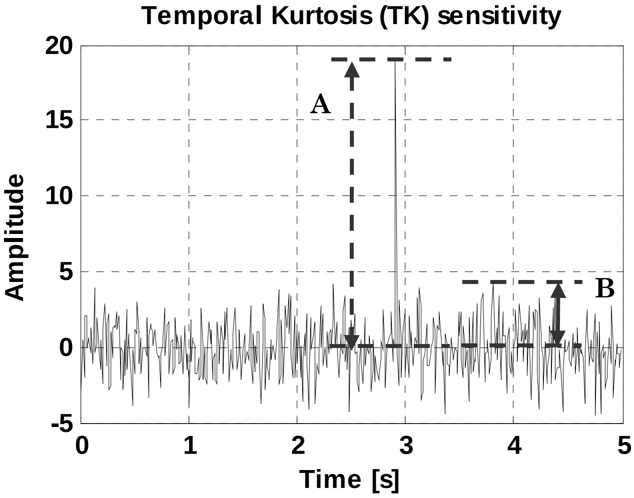

Fig. 2.1 – Example to illustrate TK sensitivity.

The **Temporal Kurtosis (TK)** is a measure of the peakedness of the PDF of a real-valued random variable. The kurtosis value is useful in identifying transients and spontaneous events within vibration signals and it is typically normalized by the square of the second moment as follows:

$$TK = \frac{1}{N}\sum_{i=1}^{N}\frac{(s(i)-\overline{s})^4}{\sigma^4} \tag{2.2}$$

where $s(i)$ is the instantaneous amplitude of the vibration signal, $\overline{s}$ is the average amplitude, σ^2 is the variance of the signal and N is the number of samples. The TK value is constant irrespective of the signal amplitude or frequency. As depicted in defining A the amplitude of a peak and B the amplitude of the uniformly distributed background noise, the higher is the ratio A/B the larger is the TK value. Increasing the number of such peaks introduced in the signal, while keeping the ratio A/B constant, reduces the kurtosis value.

The **Impulse Factor** (IF) is defined as follows:

$$IF = \frac{Peak}{\frac{1}{N}\sum_{i=1}^{N}\left|s(i)\right|} \tag{2.3}$$

where $s(i)$ is the instantaneous amplitude of the vibration signal and N is the number of samples.

This parameter has a similar meaning as CF but it assumes upper values. IF has been used by Sun [40] for the detection of faults in bearings because of its robustness to changing operating conditions.

2.2.2. Approximate Entropy (AppEn)

The **Approximate Entropy (AppEn)** parameter is a statistical measure that quantifies the regularity of a time series in multiple dimensions.

The theoretical background of the AppEn, that contains time-related information, is developed by Pincus in [41]. It has shown to be effective in the field of biomedical engineering, physiological data analysis and human motion. Recently, the application of AppEn has been extended to machine condition monitoring and fault diagnosis [42][43].

Yan and Gao [42] investigated the utility of AppEn as a measure for characterizing machine operation conditions and studied the effects of several parameters that are of key relevance for the calculation.

For a time series S containing N data points $\{x(1), x(2), ..., x(N)\}$, its “regularity” can be measured by AppEn in a multiple dimensional space, in which a series of vectors are constructed and expressed as

$$\begin{aligned} &X(1) = \{x(1), x(2), ..., x(m)\} \\ &X(2) = \{x(2), x(3), ..., x(m+1)\} \\ &... \\ &X(N-m+1) = \{x(N-m+1), x(N-m+2), ..., x(N)\}. \end{aligned} \tag{2.4}$$

In Eq.(2.4) each of the vectors is composed by m consecutive and discrete data points of the time series S.

The distance $d(X(i), X(j))$ between two vectors $X(i)$ and $X(j)$ can be defined as the maximum difference in their respective corresponding elements:

$$d(X(i), X(j)) = \max_{k=1,2...,m}(|x(i+k-1) - x(j+k-1)|), \tag{2.5}$$

where $i = 1,2..., N-m+1,\ j = 1,2..., N-m+1$.

For each vector $X(i)$, a measure that describes the similarity between the vector $X(i)$ and all other vectors $X(j)$, with $j = 1, 2, ..., N-m+1$ and $j \neq i$, can be constructed as follows:

$$C_i^m(r) = \frac{1}{N-(m-1)} \sum\nolimits_{j \neq i} \Theta\{r - d(X(i), X(j)]\}, \quad j = 1,2,\ldots, N-m+1,$$

where

$$\Theta\{x\} = \begin{cases} 1, x \geq 0 \\ 0, x < 0. \end{cases}$$

The symbol r represents a predetermined tolerance value defined as

$$r = k \cdot std(S)$$

where k is a constant (k>0), and $std(\bullet)$ represents the standard deviation of the time series.

By defining

$$\phi^m(r) = \frac{1}{N-m+1} \sum\nolimits_i \ln\left[C_i^m(r)\right], \quad i = 1,2,\ldots, N-m+1. \tag{2.6}$$

the AppEn value of a time series containing N data points can be calculated as

$$ApEn(m, r, N) = \phi^m(r) - \phi^{m+1}(r) \tag{2.7}$$

It is worth noting that, by definition, the AppEn value is greater than 0.

Specifically, a periodic time series containing only a single frequency component will have a low AppEn value (which approaches 0 but is greater than 0), due to the high regularity of the signal.

Complex time series containing multiple frequency components will have high AppEn values due to a low level of regularity.

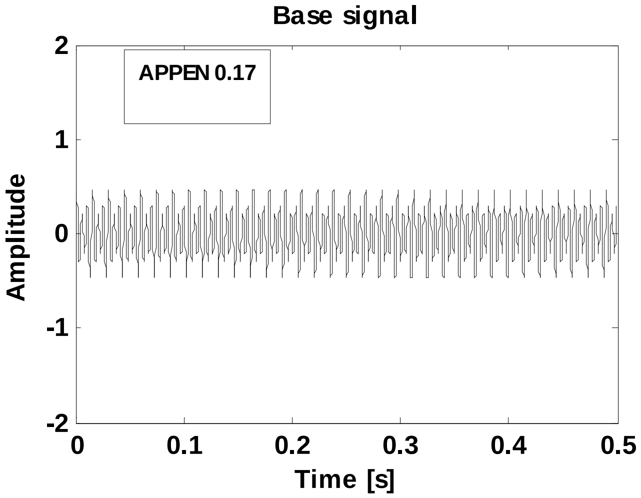

Fig. 2.2 – Periodic signal with 5 frequency components.

Fig. 2.2, Fig. 2.3 and Fig. 2.4 exemplify the influence of the signal-to-noise ratio (SNR) on the AppEn values for a synthesized periodic signal with five frequency components with and without adding noise. The test signal is given by:

$$x_t(t) = \sum_{i=1}^{N} A_i \sin[2\pi f_A(i)t] \tag{2.8}$$

with A_i and $f_A(i)$ representing the amplitude and the frequency of the i th sinusoidal element respectively. Specific values of these parameters are listed in Table 1.

Table 1- Parameters related to $x_t(t)$ test signal

	Sinusoidal component				
Parameter	1	2	3	4	5
A_i	0.016	0.112	0.325	0.029	0.016
$f_A(i)$ [Hz]	67.5	135	202.5	270	337.5

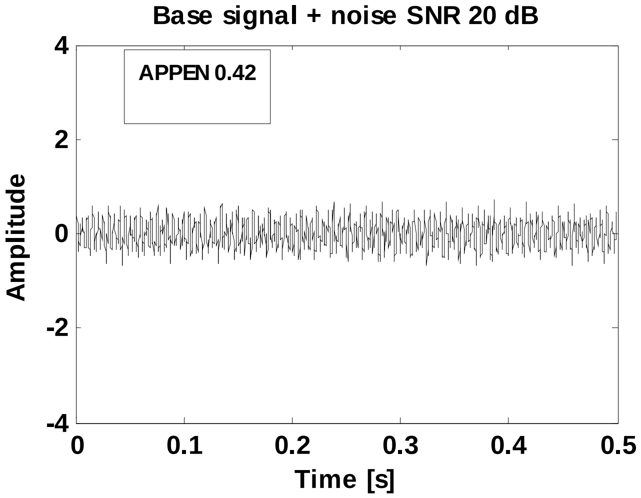

Fig. 2.3 – Periodic signal with 5 frequency components plus additive noise with SNR of 20 dB.

The choice of the acquisition parameters is made in order to reproduce the acquisition parameters of the actual signals extracted from the threshing machine:

$f_s = 6\,kHz$

$T = 0.5\,s$

where f_s is the sampling frequency and T the acquisition period.

To be based on the results found in [42], the number of sampling points $N = 3000$ of sampling points was considered sufficient for achieving stable and consistent AppEn values.

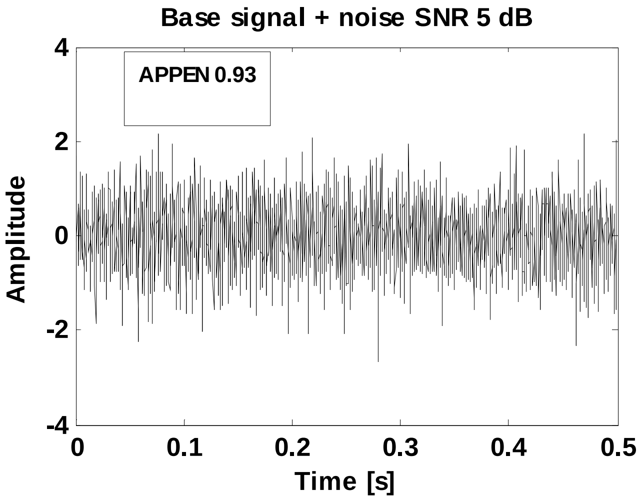

Fig. 2.4 – Periodic signal with 5 frequency components plus additive noise with SNR of 5 dB.

The tolerance value k and the dimension value m used for both test and actual signals are 0.4 and 2 respectively.

Concerning the test signal, it is evident that as the SNR decreases the AppEn increases.

2.2.3. Time Synchronous Average (TSA)

Time Synchronous Averaging (TSA) is a well adopted signal processing technique which enables periodic waveforms to be extracted from noisy signals.

By means of the above mentioned technique we can obtain the averaged angular signal after averaging several time histories in one machine cyclic period. In practice, the cyclic period will be 720 degrees for a 4-stroke IC engine, the angle necessary to have the same teeth in contact in a gearbox and so on.

In order to obtain an angular signal the order tracking, which samples the vibration signal at constant angular increments, is needed. Classically, this has been accomplished using a tachometer signal which delivers one pulse per revolution [44][45]. However an optical encoder (with multiple pulses per revolution) can also be used for a better angular resolution. Particular techniques have also been proposed for angular resampling of the vibration signal without the need of a speed sensor [46].

One recently proposed technique estimates the TSA from the instantaneous phase position of the shaft extracted from the phase demodulation of the vibration signal [47]. Other techniques use a DFT peak detection method in order to search the frequencies with the highest amplitude values in the time-frequency spectrogram [48].

Traditional order tracking directly samples the analog vibration signal at constant angular increments using a signal proportional to the machine speed to control the sampling rate. It will be shown that I.C. engine cold test applies this method by means of an encoder signal with 360 pulse/rev.

On the contrary, the computed order tracking method first records the data ad constant time increments, using conventional hardware and then resamples this signal to provide the desired data at constant angular increments.

This method is carried out by means of a keyphasor signal that is typically a once per shaft revolution event. This signal is used to measure the shaft speed and represents the reference for measuring the vibration phase angle.

This second method has been used for the TSA calculation for threshing machine signals. To determine the resample times it will be assumed that the shaft is undergoing constant angular acceleration. The corresponding amplitudes will be calculated by interpolating between the sampled data using a linear interpolation method.

2.2.4. Amplitude and phase/frequency demodulation

A generally modulated signal $x(t)$ can be expressed by the following form [38]:

$$x(t) = \mathrm{Re}\left\{A(t)e^{i\phi(t)}\right\} \tag{2.9}$$

where the amplitude $A(t)$ and instantaneous phase angle $\phi(t)$ are functions of time.

The instantaneous frequency is

$$f_x(t) = \frac{1}{2\pi}\frac{d\phi(t)}{dt} \tag{2.10}$$

and it is expressed in *Hz*.

The phase modulation can be carried out calculating the Hilbert Transform of the original signal in order to obtain the analytic signal. In fact, the analytic signal is a *complex* time signal whose real part is the original signal $x(t)$ and where imaginary part is the Hilbert transform of $x(t)$.

The analytic signal $c(t)$ is defined as follows:

$$c(t) = x(t) + i\tilde{x}(t) = \left|c(t)\right| \cdot e^{i\phi(t)} \tag{2.11}$$

with $\tilde{x}(t)$ the Hilbert Transform of the raw signal $x(t)$.

The phase $\phi(t)$ (expressed in radiant) can be obtained by the following formula

$$\phi(t) = \tan^{-1}\frac{\tilde{x}(t)}{x(t)} \tag{2.12}$$

For sake of clearness two test signals are formulated in order to depict the results of the amplitude ($x_{am}(t)$) and frequency ($x_{pm}(t)$) demodulations.

$$x_{am}(t) = (A + A_{am}\cos 2\pi f_{am}t)\sin 2\pi ft \tag{2.13}$$

$$x_{pm}(t) = A\cos(2\pi ft + A_{pm}\sin 2\pi f_{pm}t) \tag{2.14}$$

Fig. 2.5 and Fig. 2.6 show an amplitude modulated and a phase modulated signal respectively (see Table 2 and Table 3 for the test signal parameters).

Fig. 2.8 shows the unwrapped phase signal in which its slope has been removed by a “detrend” operation that makes the phase variation more clearer. Fig. 2.9 depicts the instantaneous frequency obtained by the differentiation of the detrended phase.

It is worth noting that the use of the analytic signal represents a first approach for analyzing how the frequency content of a signal varies with time. However the notion of instantaneous frequency assumes that, at each time instant, there exists only a single frequency component.

Table 2 – Amplitude modulated signal

Parameter	
A	1
f [Hz]	10
A_{am}	0.3
f_{am} [Hz]	5

Table 3 – Phase modulated signal

Parameter	
A	1
f [Hz]	10
A_{pm}	5
f_{pm} [Hz]	1

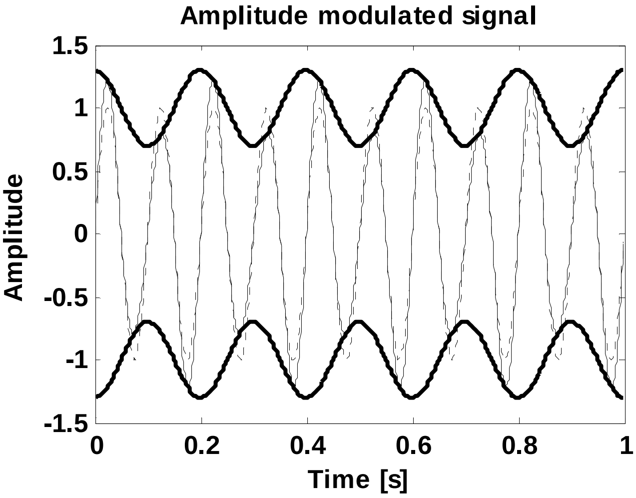

Fig. 2.5 – Original signal (dashed line); amplitude modulated signal (normal line); amplitude modulation signal (solid line).

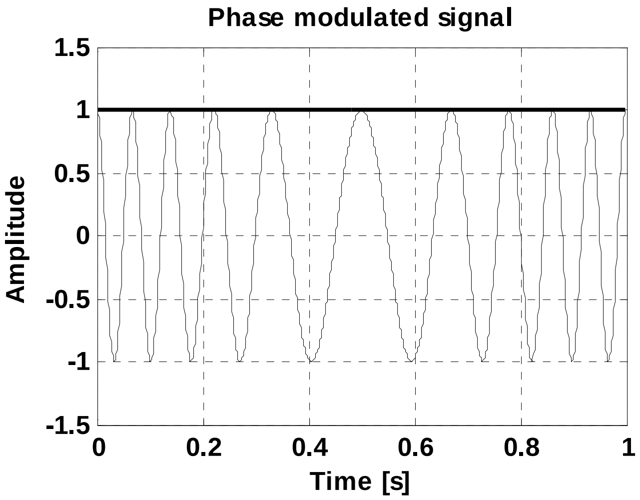

Fig. 2.6 – Phase modulated signal (normal line); amplitude modulation signal (solid line).

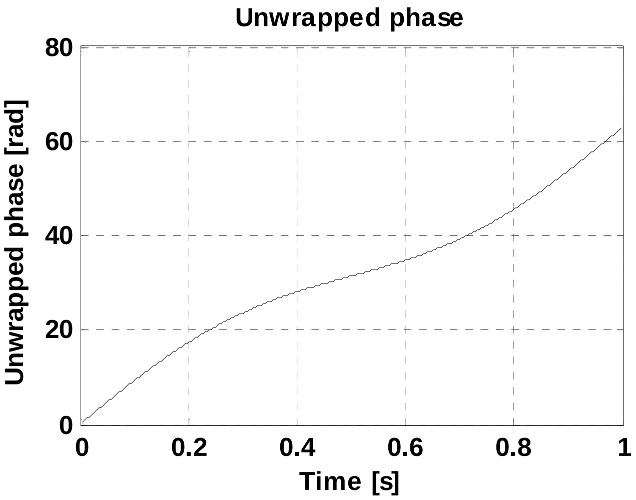

Fig. 2.7 – Unwrapped phase of the phase modulated signal depicted in Fig. 2.6.

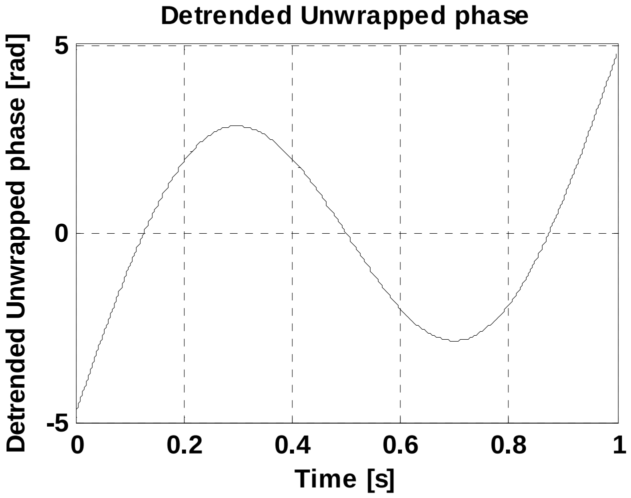

Fig. 2.8 – Detrend of the phase signal depicted in Fig. 2.7.

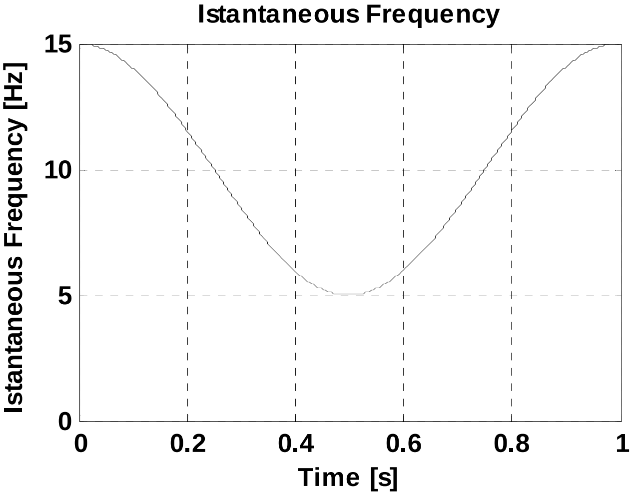

Fig. 2.9 – Instantaneous frequency of the phase modulated signal depicted in Fig. 2.6.

Obviously this assumption is not valid for most of the multi-component real signals, so the result obtained using the instantaneous frequency can be useless. For this reason two-dimensional representations, jointly in time and frequency domains, are needed: they capabilities will be described in the Section 2.4.

2.2.5. Symmetrized Dot Pattern method (SDP) and Image Correlation

As presented in [49], the normalized time histories of the vibration signal concerning diesel engines can be represented as symmetrized dot graphs. The formulation used for the transformation of the discrete signal *x(n)* to a polar coordinate graphs and the properties of this method are described in [50] and summarized as follows.

A point in the time waveform is mapped into a radial component, and the adjacent point is mapped to an angular component.

The transformation from the time waveform to symmetrized dot space can be written as:

$$x(n) \rightarrow S(r_j,\ \theta_{\mathrm{ij}},\ \phi_{\mathrm{ij}}) \tag{2.15}$$

where $x(n)$ is the digitized time waveform and S is the Symmetrized Dot Pattern (SDP).

Here S is a function of r, the radial vector in polar coordinates, and θ and ϕ are two angles on the polar space.

If we indicate the amplitude of a time waveform at time point j with F_j, the algorithm maps the amplitude at points j and $j + LAG$ directly into polar space (with subsequent reflection around various mirror planes) in the following manner:

$$r_j = \left(\frac{F_j - L}{H - L} \right) g \tag{2.16}$$

$$\theta_{ij} = \theta' + \left(\frac{F_{j+LAG} - L}{H - L} \right) g \tag{2.17}$$

$$\phi_{ij} = \theta' - \left(\frac{F_{j+LAG} - L}{H - L} \right) g \tag{2.18}$$

where

$$j = 1, 2, 3, \ldots, N-1,$$
$$\theta' = (360^\circ / m) i,$$
$$i = 1, 2, 3, \ldots, m.$$

Here N is the number of points in the waveform window, m is the number of mirror planes, g is the upper boundary used to normalize the gain of the input waveform, H is the highest value of the original waveform window, L is the lowest value of the original waveform window.

In this work the time lag (i.e. LAG) and the gain g present the following values: $LAG = 1$, $g = 50$. These values are selected according to the results shown in [49] in order to obtain a high degree of symmetry and a low computational cost.

The SDP transformation is depicted in Fig. 2.10 (a) and (b).

In order to implement this technique in the cold test procedure for fault detection, it is necessary to develop an image correlation system [51]. The author applied the algorithm of the edge detection, illustrated in [55], which represents the most common approach for detecting meaningful discontinuities in intensity values.

The basic idea behind the edge detection is to find the points where the intensity rapidly changes. For each case, by applying this edge detection algorithm on the image of the visual symmetrized dot polar graph, the result will be a logic matrix with 1's (represented as white pixels in the grey scale) at the locations where edge points were detected on the image, and 0's (black pixels) elsewhere (Fig. 2.10 (c)).

The goal is to identify a reference pattern that represents the normal condition and then compare the images obtained from all the test engines with this "healthy pattern" by means of a similarity parameter. Among many possibilities, this parameter, called correlation, was chosen as the percentage of common white pixels with respect to the total number of white pixels in the healthy engine pattern.

2.2.6. Instantaneous Angular Speed (IAS) analysis

Instantaneous-Angular-Speed(IAS)-based condition monitoring is a recent novel research area less known compared to the existing vibration-based condition monitoring methods.

The developed methods for the IAS measurement and all the problems related to its accuracy are well reported in [52] and [53].

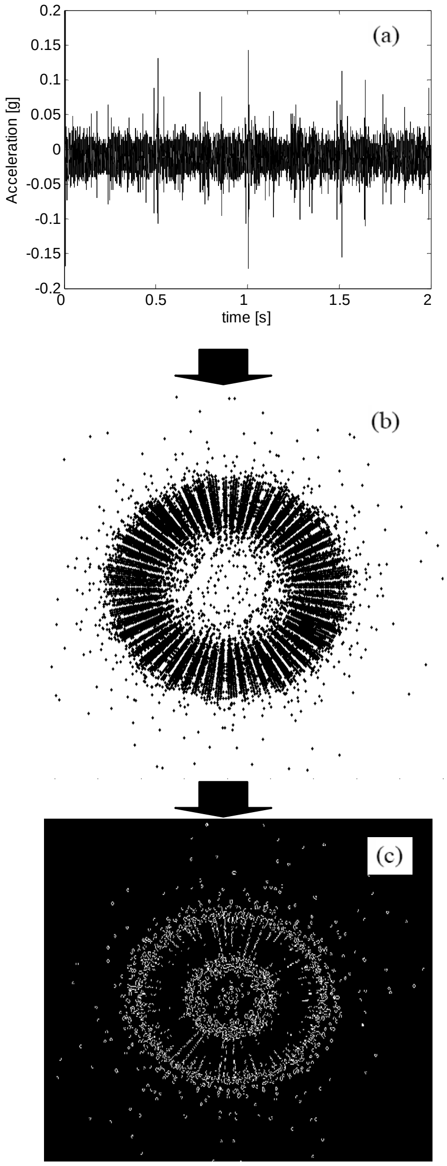

Fig. 2.10. – SDP method: (a) time input waveform; (b) symmetrized dot polar graph and (c) image obtained after the edge detection algorithm application.

Several applications of the IAS measurement can be found in literature. In [54] the IAS has been analysed as a means to monitor the condition of gears subjected to fluctuating load conditions. In [33] the

IAS waveforms have been studied in order to detect faults in diesel engines related to the gas pressure.

In this thesis, the IAS is calculated in order to evaluate its capabilities in detecting assembly faults in diesel engines through tests carried out without combustion. The calculation is accomplished by an encoder signal with 1024 pulse/rev.

Generally speaking, there are two conventional methods for translating the tacho signals into the rpm information:

- the counter method in which a high speed counter (i.e. hundreds of MHz) clocks the time intervals between the zero-crossing of the tacho signals;
- the frequency to voltage (F/V) converter method in which an analog circuit translates pulse voltage into an analog output voltage measuring the rpm deviation.

Then, the angle can be obtained performing an integration of the angular velocity.

In this work, the IAS has been obtained by a new method (defined “direct ADC” method by Li in [52]) in which the stream of the encoder pulses are converted to digital data and translated to the rpm information by means of an interpolation algorithm.

First, the data is up-sampled by a factor of two by a very accurate interpolation filter. The up-sampled data (5μs sample intervals) is then examined for zero-crossings. When such an interval is encountered, it is again interpolated by a factor of 32, using the very accurate Lagrange polynomial interpolation method. Finally, the Lagrange interpolated samples are again examined for a change of sign, after which a linear interpolation action is performed in order to determine the exact zero crossing. Therefore, this algorithm can assure an equivalent time resolution of several GHz.

2.3 Frequency domain analysis

The theoretical frequency spectrum of a signal $x(t)$ is usually described by its Fourier Transform given by:

$$X(f) = \int_{-\infty}^{+\infty} x(t) e^{-j2\pi ft} dt \tag{2.19}$$

with f is the frequency variable.

When implemented by DSP, the Fourier spectrum is usually approximated by the Discrete Fourier Transform (DFT).

The differences from the theoretical definition expressed by the Equation (2.19) are the following:

- the use of time-discrete sampled signals;
- the observation and summation over a finite time interval;
- the discrete nature of the frequency spectrum.

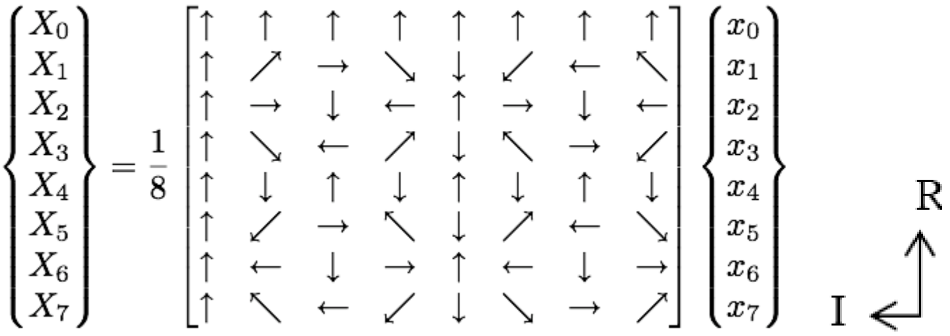

Fig. 2.11 – Matrix representation of the FFT algorithm

The FFT [55] is the fast algorithm for calculating DFT of a block *g(n)* of *N* samples data giving a spectrum *G(k)* of *N* frequency lines, using the formula:

$$G(k) = 1/N \sum_{n=0}^{N-1} g(n) \exp(-j2\pi kn/N) \tag{2.20}$$

Equation (2.20) assumes that *g(n)* is one period of a periodic signal, so that the spectrum is that of the corresponding Fourier series. The sample index number *n* represents time $n\Delta t$, where Δt is the reciprocal of the sampling frequency f_s. Similarly, the frequency index *k* represents frequency $k\Delta f$, where Δf is the spectral line spacing, the reciprocal of the record length ($= N\Delta t$). Because the time signal is sampled, the spectrum *G(k)* is also periodic, with a period equal to the sampling frequency f_s. When the signal *g(n)* is real, the negative frequency components are the complex conjugates of the positive frequency components, and there are thus only *N/2* independent complex spectrum values. Because of the periodicity of the spectrum, the second half (from $f_s/2$ to f_s) represents the negative frequency components (from $-f_s/2$ to zero). This explains why all frequencies in the original signal outside this range ($-f_s/2$ to $f_s/2$) must be removed by a low pass filter before digitization, as they would otherwise mix with the true components within this range causing “aliasing”.

Fig. 2.11 represents the matrix representation of the Eq. (2.20) for *N*=8. The matrix shows the orientation of the complex exponential components (unit vectors) for the various values of *k* (frequency index) and *n* (time index). Note the orientation of the real and imaginary axes (R and I); the first row represents zero frequency and the first column zero time.

As reported by Randall in [55] the FFT is a powerful tool when it is used with a harmonic and sidebands cursor in order to evaluate some amplitude/phase modulation effects.

2.4 Time-frequency analysis

As said before the problem of analysing measured signals in the frequency domain is solved by applying a DFT on the signals.

The main characteristics of this approach are that:

- only spectral results, which are an average for the duration T of the observation interval, are obtained;

- the frequency resolution Δf of the signal is limited by the length of the observation window.

When the nature of the signal is varying with the time, a repeated Fourier analysis for consequent time segments tries to describe the temporal variation of the signal spectrum. This well known technique is called Short Time Fourier Transform (STFT).

The principal limitations of this approach are:

- for each analysed time segment, only "average" results are obtained, requiring short analysis segments for a good time resolution;
- the shorter the analysed time segment is, the coarser the resulting frequency resolution will be;

A more rigorous explanation of the latter is the Uncertainty Principle or Bandwidth-Time product that is easily proved in [1] using the Parseval theorem and the Schwartz' s inequality. This Principle states that:

$$\Delta f \cdot \Delta t \geq \frac{1}{4\pi} \tag{2.21}$$

where Δf is the frequency resolution expressed in Hertz and Δt is the time resolution expressed in seconds.

It is not so difficult to understand that the (2.21) points out a limitations of the STFT analysis methods: a fine resolution in both time and frequency domains at the same time cannot be obtained.

Several techniques have been developed [56][57] to overcome this problem and to analyse different types of non-stationary signals.

As well reported in [56], one can distinguish three important class of non-stationary signals:

- Evolutionary Harmonic Signals related to a periodic phenomenon (i.e. rotation) of varying frequency;
- Evolutionary Broadband Signals with a broadband spectrum but with spectral content evolving with time (i.e. road noise);
- Transient Signals which show a very short time segment totally evolving in nature (i.e. door-slam acoustic response and diesel engine irregularity inside one combustion cycle).

Another important class of non-stationary signals is represented by the Cyclostationary Signals which will be described in the Section 2.5.

Since this work deals with Transient and Cyclostationary signals Wavelet analysis and Wigner-Ville Distributions have been proposed as proper analysis tools.

2.4.1. Continuous Wavelet Transform (CWT)

When referring to the definition of the Fourier Transform (2.19), it can be seen that this formulation describes the signal $x(t)$ by means of a set of functions $e^{j\omega t}$ forming a basis for signal expansion. These functions are continuous and of infinite duration. The spectrum corresponds to the expansion coefficients.

An alternative approach consists of decomposing the data in time-localised waveforms. Such waveforms are usually referred to as wavelets. In the last decades the theoretical background of the wavelet transform has extensively reported ([58]-[62]).

The Continuous Wavelet Transform (CWT) of the time signal *x(t)* is defined as:

$$CWT(a,b)=\frac{1}{\sqrt{a}}\int_{-\infty}^{+\infty}x(t)\psi^{*}\left(\frac{t-b}{a}\right)dt \tag{2.22}$$

with $a\in R^{+}-\{0\},b\in R$.

This is a linear transformation decomposing the original signal into elementary functions $\psi_{a,b}$:

$$\psi_{a,b}(t)=\frac{1}{\sqrt{a}}\psi\left(\frac{t-b}{a}\right) \tag{2.23}$$

which are determined by the translation (parameter *b*) and the dilation (parameter *a*) of a so called ‘mother (analyzing) wavelet’ $\psi(t)$.

The translation parameter *b* describes the time localization of the wavelet, while the dilation *a* determines the width or scale of the wavelet. It is worth noting that, by decreasing the scale parameter *a*, the oscillation frequency of the wavelet increases, but the duration of the oscillation decreases, so it can be noted that exactly the same number of cycles is contained within each wavelet.

Therefore, an important difference with classical Fourier Analysis, in which the time window remains constant, is that the time and frequency resolution now becomes dependent on the scale factor a. For the CWT, in fact, the width of the window in the time domain is proportional to a, while the bandwidth in the frequency domain is proportional to $1/a$. Thus, in the frequency domain, the WT has a good resolution for low frequencies and, in the time domain, good resolution for high frequencies; the latter property makes the CWT suitable for the detection of transient signals. Details and application of CWT can be found in literature ([63]-[70]).

In order to be classified as wavelet, a function must satisfy certain mathematical criteria:

- A wavelet must have finite energy:

$$E = \int_{-\infty}^{\infty} |\psi(t)|^2 dt < \infty \tag{2.24}$$

where E is the energy.

- If $\hat{\psi}(f)$ is the Fourier Transform of $\psi(t)$, then the following condition must hold:

$$C_g = \int_{0}^{\infty} \frac{|\hat{\psi}(f)|^2}{f} df < \infty \tag{2.25}$$

this implies that $\hat{\psi}(0) = 0$, so that the wavelet $\psi(t)$ must have a zero mean.

Equation (2.25) is known as the *admissibility condition* and C_g is called the *admissibility constant*. The value of C_g depends on the chosen mother wavelet.

- An additional criterion that must hold for complex wavelets is that the Fourier Transform must both be real and vanish for negative frequencies.

As with its Fourier counterpart, we can define the inverse wavelet transform as follows:

$$x(t) = \frac{1}{C_g} \int_{-\infty}^{+\infty} \int_{0}^{\infty} CWT(a,b) \psi_{a,b}(t) \frac{dadb}{a^2} \tag{2.26}$$

The inverse wavelet transform allows the original signal to be recovered from its wavelet transform by integrating over all scales a and dilations b. Note that for the inverse wavelet transform, the original wavelet transform is used rather than its conjugate that is used in the forward transformation. If we limit the integration over a range of scales it is possible to perform a filtering of the signal.
There are 2 kinds of mother wavelet:

- the above defined mother wavelets that can be described by analytical functions;
- mother wavelets obtained by means of an iteration procedure, like orthogonal wavelets, that are well suited to perform the Discrete Wavelet Transform (DWT) (see Section 2.4.2) [73].

Concerning the formers, one of the most interesting is the Morlet wavelet defined as:

$$\psi(t)_{morlet} = \frac{1}{\pi^{-1/4}} e^{-t^2/2} e^{i2\pi f_0 t} \tag{2.27}$$

where f_0 is the central frequency of the mother wavelet. The term $1/\pi^{-1/4}$ is a normalization factor which ensures that the wavelet has unit energy; the Gaussian envelope $e^{-t^2/2}$ modulates the complex sinusoidal waveform.
Since the Morlet wavelet is a complex mother wavelet, by using it we can separate the phase and amplitude components within any signal.

The result of the CWT is graphically represented in the time-scale plane, while in this thesis the maps have been displayed in the time-frequency domain, using the relationship $f = f_0 / a$ between the central frequency of the analyzing wavelet f_0 and the scale.

Moreover, when complex analyzing wavelets have been used, only the amplitude will be considered and represented using a linear scale.

Concerning the CWT implementation, the algorithm proposed by Wang and Mc Fadden [72] has been applied taking the advantages of the FFT algorithm.

2.4.1.1 CWT improvements

Several improvements have been taken into account in this work in order to improve the CWT power in detecting and localizing transients within a signal. These enhancements concern:

- the choice of the mother wavelet;
- the time-frequency map representation;
- the calculation of the CWT of the TSA.

Firstly, as a first improvement, the Impulse mother wavelet is taken into account in this work due to its capability for the analysis of impulses in vibration signals. It is defined as follows:

$$\psi(t)_{impulse} = \sqrt{2\pi} e^{2\pi i f_0 t - |2\pi t|} \cos\left(2\pi f_0 t\right) \tag{2.28}$$

where f_0 is the central frequency of the mother wavelets.

Its capabilities and the comparison between Morlet and Impulse mother wavelets in analysing transient signals are well reported in [76] and [77].

In this work the f_0 assumes the most common values found in literature: it is equal to 0.8125 Hz for Morlet mother wavelet and 20 Hz for the Impulse one.

Secondly, a purification method inspired to the work of Yang [78] has been considered in order to improve the accuracy of the CWT representation and trying to solve the problem of the frequency overlapping already reported in [79]. Yang applied the purification method using the Morlet wavelet while in this work the Impulse wavelet has also been taken into account.

By means of the purification methods, new CWT coefficients ($\widehat{CWT}$) are calculated through the following equation:

$$\widehat{CWT}(a,b,t) = \gamma(a,t) \cdot CWT(a,b,t) \tag{2.29}$$

The term $\gamma(a,t)$ is the coefficient of correlation between the original signal and the sinusoidal function with the frequency of the present

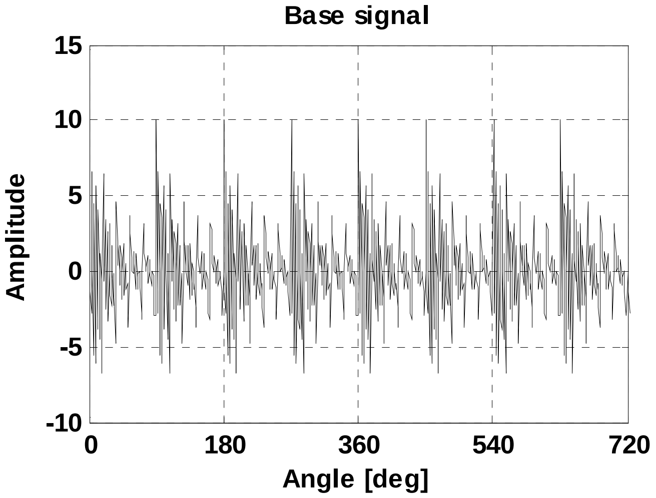

Fig. 2.12 – Simulated signal without additive noise.

wavelet scale given by ω_0 / a with ω_0 as the central frequency of the mother wavelet.

The correlation coefficient can be written as:

$$\gamma(a,t) = \left| \frac{\operatorname{cov}(x(T), H(a,T))}{\sigma_{f(T)}\sigma_{H(a,T)}} \right| \tag{2.30}$$

where T $\in [t - \tau/2; t + \tau/2]$, τ is time duration of the signal *x(t),* σ is the standard deviation, *H* is the sinusoidal function and *a* indicates the wavelet scale. The expression 'cov' means covariance and it is defined for two data histories x_1 and x_2 as:

$$Cov(x_1, x_2) = E\left[(x_1 - \mu_1)(x_2 - \mu_2) \right]$$

where E is the mathematical expectation and $\mu_1 = E[x_i]$.

It can be noted that the correlation between the signal and the sinusoid *H* is evaluated in a short time duration define by a time window with duration τ . Next, the time window is moved for the whole time duration of the signal. After several tests, the choice of the window time duration τ is based on a reliable compromise between the requirement of obtaining a higher correlation coefficient and the computational time needed for the correlation calculation.

A signal, simulating typical machine signals containing sinusoids and impulse responses, is formulated in order to evaluate the capabilities of this proposed method:

$$x(t) = 8e^{-\tau/0.015}\sin(\omega_0 \tau) + \sum_{1}^{4}\sin(\omega_i t) \tag{2.31}$$

with $\omega_0 = 2\pi f_0$, $\omega_i = 2\pi f_i$, and

$$\tau = \begin{cases} t & (0 \le t/t_0 < 1) \\ t - Nt_0 & (N \le t/t_0 < N+1) \end{cases}$$

with $f_0 = 600Hz$, $t_0 = 0.05$, $f_i = i \times 100$, N as a integer value.

In order to be consistent with the analysis carried out on the actual signals, the simulated signal is assumed to be extracted from a rotating machinery running at the constant speed of 5 Hz and resampled in the angular domain. In such resampling way we can obtain the signal depicted in Fig. 2.12.

From Fig. 2.13 and Fig. 2.14 it is obviously found that the purification method gives a more accurate separation of the frequency components within the CWT maps obtained by means of the Morlet wavelet. As the 600 Hz frequency component is clearly indicated, the other four components remain smeared.

Moreover, comparing the Morlet and Impulse wavelet capabilities, the superiority of the latter in distinguishing close frequency components it is observed from Fig. 2.15. It is worth noting that the Morlet wavelet seems to be more effective in angularly localizing the impulsive components.

It is also observed form Fig. 2.16 that the purification method applied to the CWT map using Impulse wavelet helps to remove the overlapping phenomenon clearly revealing the 600 Hz frequency of the impulses. Then it has shown that the others frequencies are not smeared anymore.

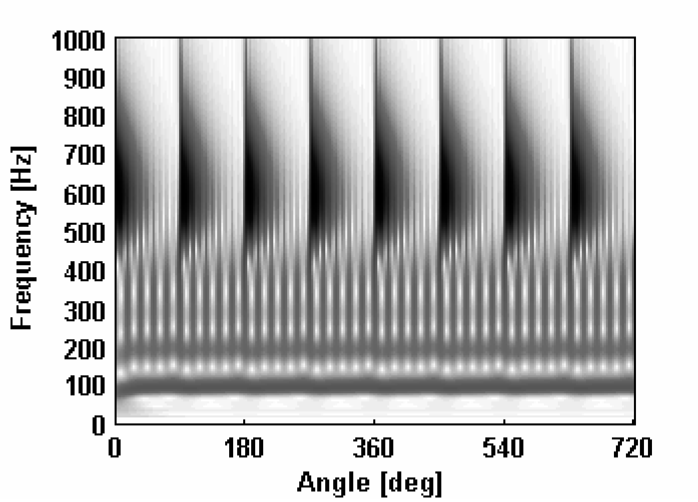

Fig. 2.13 – CWT (Morlet wavelet) of the simulated signal without noise: traditional method.

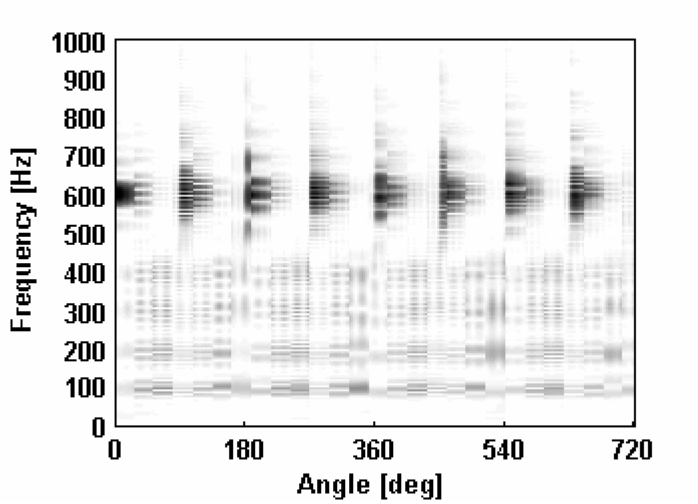

Fig. 2.14 – CWT (Morlet wavelet) of the simulated signal without noise: purification method.

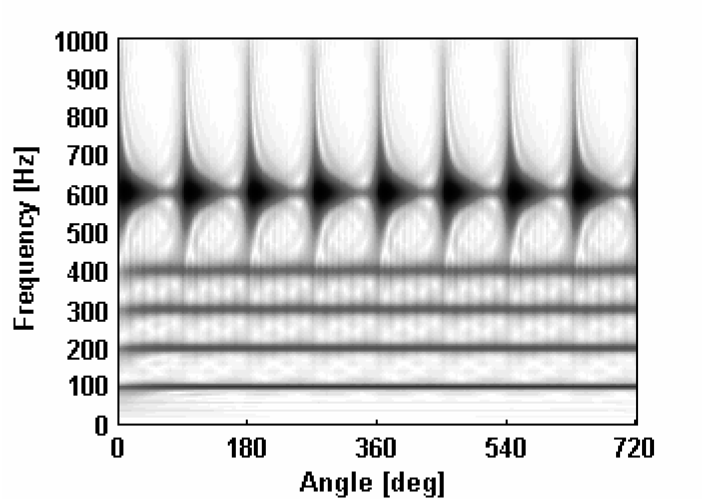

Fig. 2.15 – CWT (Impulse wavelet) of the simulated signal without noise: traditional method.

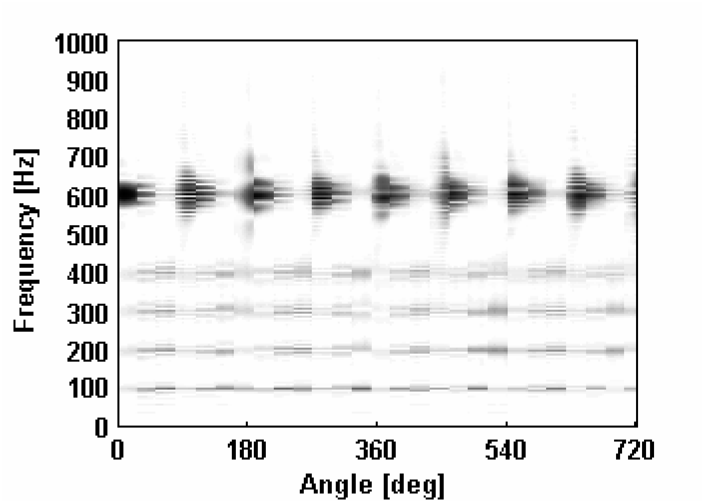

Fig. 2.16 – CWT (Impulse wavelet) of the simulated signal without noise: purification method.

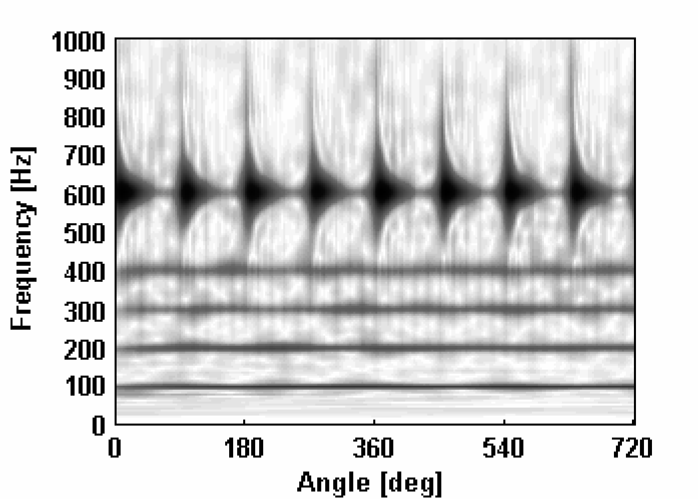

Fig. 2.17 – CWT (Impulse wavelet) of the simulated signal and additive noise (SNR 5dB): traditional method.

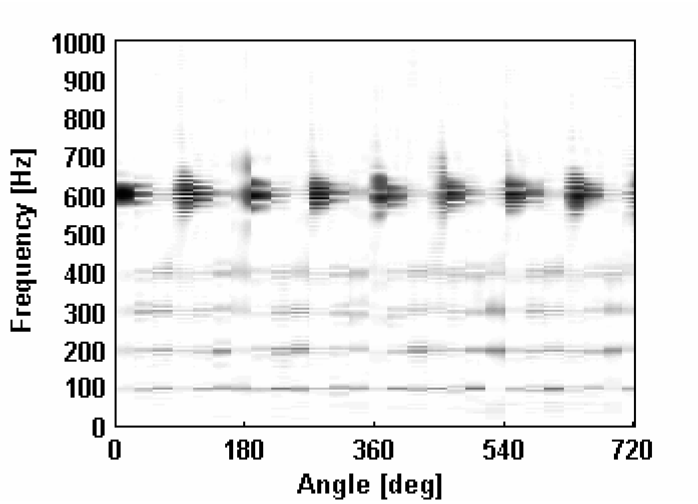

Fig. 2.18 – CWT (Impulse wavelet) of the simulated signal and additive noise (SNR 5 dB): purification method.

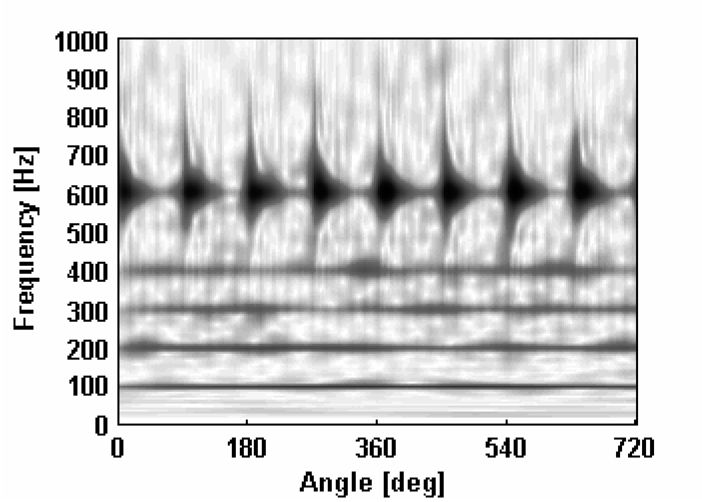

Fig. 2.19 - CWT (Impulse wavelet) of the simulated signal and additive noise (SNR 1 dB): traditional method.

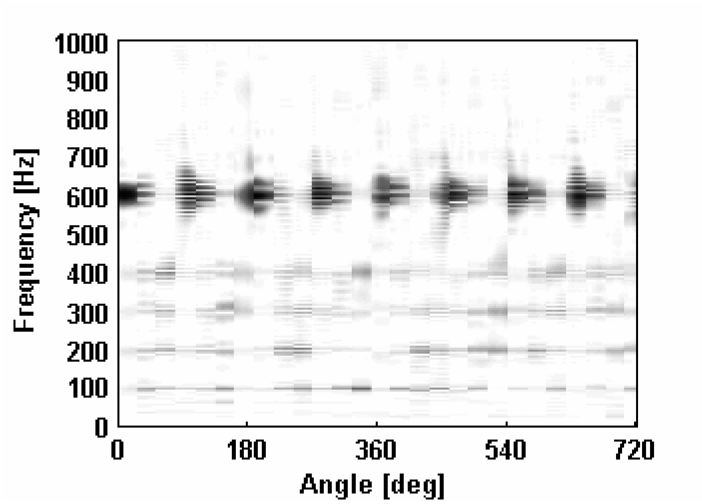

Fig. 2.20 – CWT (Impulse wavelet) of the simulated signal and additive noise (SNR 1 dB): purification method.

Subsequently a signal composed by the previous signal and additive noise is analyzed in order to evaluate the noise sensitivity of the purification method using Impulse wavelet. Even the Impulse wavelet is already a strong tool against the influence of the white noise, the purification method still continues to delete the overlapping phenomenon at both signal-to-noise ratio (SNR) levels.

A drawback of the purification method is represented by the choice of the correlation window length. A mistake in this selection can influence the smoothness and the continuity of the wavelet coefficients in the CWT map.

On the basis of these results it is expected that the CWT calculation over real signals using Impulse wavelet and purification method can give advantages in terms of energy distribution in the time-frequency domain in presence of close frequency components.

As the last CWT improvement a new method recently proposed by Halim [47] is applied in order to compute the angular domain averaging across all the scales (TDAS) after the CWT calculation. The application of this technique to simulated and real signals and the comparison with the CWT of the TSA calculated using the traditional method will be shown in Chapter 3.

2.4.2. Discrete Wavelet Transform (DWT)

2.4.2.1 Wavelet and scaling functions, details and approximations.

The Discrete Wavelet Transform (DWT) is a technique that permits to calculate discrete coefficients replacing the continuous coefficients obtained through CWT calculation [81]. Because of this fact the parameters a and b in Eq.(2.22) become powers of two:

$$a = 2^j, b = k2^j, j, k, \in Z \tag{2.32}$$

where j is called level, 2^j denoted the scale and $k2^j$ denotes the shift in the time direction.

The DWT is defined as:

$$c_{j,k} = \frac{1}{\sqrt{2^j}} \int_{-\infty}^{+\infty} x(t) \psi^* \left(2^{-j} t - k\right) dt \tag{2.33}$$

where the elementary function is

$$\psi_{j,k}(t) = 2^{-j/2} \psi\left(2^{-j} t - k\right) \tag{2.34}$$

and where $c_{j,k}$ are the wavelet coefficients or detail coefficients that represent the time-frequency map of the original signal *x(t)*.

This power-of-two logarithmic scaling of both the dilation and translation steps is known as the dyadic grid arrangement.

The dyadic grid can be considered the most efficient discretization and lends to the construction of an orthonormal wavelet basis. In fact, discrete dyadic grid wavelets are commonly chosen to be orthonormal, i.e. orthogonal to each other and normalized to have unit energy. This means that the information stored in a wavelet coefficient $c_{j,k}$ is not repeated elsewhere and allows for the complete regeneration of the original signal without redundancy.

Orthonormal dyadic discrete wavelets are associated with scaling functions $\phi_{j,k}(t)$. The scaling function has the same form as the wavelet, given by

$$\phi_{j,k}(t) = 2^{-j/2}\phi\left(2^{-j}t - k\right) \tag{2.35}$$

The scaling function is orthogonal to translation of itself, but not to dilations of itself.

By means of the scaling function it is possible to obtain the approximation coefficients $d_{j,k}$ with the same procedure done for the wavelet function (i.e. convolving the scaling function with the signal):

$$d_{j,k} = \frac{1}{\sqrt{2^j}}\int_{-\infty}^{+\infty} x(t)\phi^*\left(2^{-j}t - k\right)dt \tag{2.36}$$

It is important to make clear the distinct difference between the approximation coefficients $d_{j,k}$ and the scaling coefficients z_n used in the scaling equation (or dilation equation). The dilation equation permits to obtain the scaling function $\phi(t)$ by means of the following equation:

$$\phi(t) = \sum_n z_n \phi\left(2t - n\right) \tag{2.37}$$

where $\phi\left(2t - n\right)$ is a contracted version of $\phi(t)$ shifted along the time axis by an integer step n and factored by an associated scaling coefficient z_n.

As an example, the Haar wavelet is the simplest example of an orthonormal wavelet. Its scaling equation contains only two nonzero scaling coefficients and is given by

$$\phi(t) = \phi(2t) + \phi(2t-1) \tag{2.38}$$

that is, its scaling coefficients are $z_0 = z_1 = 1$.

We can write the same for the wavelet equation in which the same coefficients z_n are used in reverse with alternated sign. We can indicate these new coefficients (i.e. reordered z_n coefficients) with b_n . If we consider only wavelets with compact support which have a finite number of scaling coefficients N_k, we can write the homolog equation of the (2.37):

$$\psi(t) = \sum_{n=0}^{N_k-1} b_n \phi\left(2t-n\right) \tag{2.39}$$

Joining the Equations (2.35) and (2.37) and examining the wavelet at scale index *j+1* we can see that for an arbitrary integer value *j* is true:

$$\phi_{j+1,k}(t) = \frac{1}{\sqrt{2}} \sum_n z_n \phi_{j,2k+n}(t) \tag{2.40}$$

which means that the scaling function at an arbitrary scale is composed of a sequence of shifted scaling functions at the next smaller scale each factored by their respective scaling coefficients. Similarly for the wavelet function we can write:

$$\psi_{j+1,k}(t) = \frac{1}{\sqrt{2}} \sum_n b_n \psi_{j,2k+n}(t) \tag{2.41}$$

2.4.2.2 The multiresolution representation

A continuous approximation of the signal at scale *j* can be generated by summing a sequence of scaling functions at this scale factored by the approximation coefficients as follows:

$$x_j(t) = \sum_{k=-\infty}^{+\infty} d_{j,k} \phi_{j,k}(t) \tag{2.42}$$

where $x_j(t)$ is a smooth, scaling function dependent, version of the signal $x(t)$ at scale index j.

We can represent a signal $x(t)$ using a combined series expansion using both the approximation coefficients and the wavelet (detail) coefficients as follows:

$$x(t)=\sum_{k=-\infty}^{\infty} d_{j_0,k}\phi_{j_0,k}(t)+\sum_{j=-\infty}^{j_0}\sum_{n=-\infty}^{\infty} c_{j,k}\psi_{j,k}(t) \qquad (2.43)$$

If we define the signal detail at scale j as:

$$D_j(t)=\sum_{k=-\infty}^{+\infty} c_{j,k}\psi_{j,k}(t) \qquad (2.44)$$

hence we can write equation (2.43) in a clearer manner:

$$x(t)=x_{j_0}(t)+\sum_{j=-\infty}^{j_0} D_j(t) \qquad (2.45)$$

We can see from this equation that the original continuous signal is expressed as a combination of an approximation of itself at arbitrary scale j_0 (i.e. $x_{j_0}(t)$) added to a succession of signal details from scales j_0 down to negative infinity. This is called multiresolution representation.

2.4.2.3 Decomposition algorithm

In order to obtain the multiresolution representation of a generic signal $x(t)$ as indicated by the Eq. (2.45) we have to compute the wavelet coefficients.

The decomposition algorithm, which permits the multiresolution representation, is based on the link between the scaling coefficients and the approximation coefficients defined above.

From Eq. (2.36) the approximation coefficients at scale index $m+1$ are given by

$$d_{j+1,k}=\int_{-\infty}^{+\infty} x(t)\phi_{j+1,k}\left(t\right)dt \qquad (2.46)$$

Using Eq. (2.40) we can write the link given by:

$$d_{j+1,k} = \int_{-\infty}^{+\infty} x(t)\left[\frac{1}{\sqrt{2}}\sum_n z_n \phi_{j,2k+n}(t)\right]dt \tag{2.47}$$

rewritten in

$$d_{j+1,k} = \frac{1}{\sqrt{2}}\sum_n z_n \left[\int_{-\infty}^{+\infty} x(t)\phi_{j,2k+n}(t)dt\right] \tag{2.48}$$

The integral in brackets gives the approximation coefficients $d_{j,2k+n}$ for each n. We can therefore write this equation as

$$d_{j+1,k} = \frac{1}{\sqrt{2}}\sum_n z_n d_{j,2k+n} = \frac{1}{\sqrt{2}}\sum_n z_{n-2k} d_{j,k} \tag{2.49}$$

Hence, using this equation, we can generate the approximation coefficients at scale index $j+1$ using the scaling coefficients at the previous scale (i.e. z_n multiply $d_{j,2k+n}$) .

Similarly the wavelet coefficients can be found from the approximation coefficients at the previous scale using the reordered scaling coefficients b_n as follows:

$$c_{j+1,k} = \frac{1}{\sqrt{2}}\sum_n b_n d_{j,2k+n} = \frac{1}{\sqrt{2}}\sum_n b_{n-2k} d_{j,k} \tag{2.50}$$

We can see that, if we know the approximation coefficients $d_{j_0,k}$ at a specific scale j_0 then, through the repeated application of equations (2.49) and (2.50), we can generate the approximation and detail wavelet coefficients at all scales larger than j_0. These equations represent the decomposition algorithm. The vectors containing the sequences $(1/\sqrt{2})z_n$ and $(1/\sqrt{2})b_n$ represent the filters: $(1/\sqrt{2})z_n$ is the lowpass filter, letting through low signal frequencies and hence a smoothed version of the signal, and $(1/\sqrt{2})b_n$ is the highpass filter, letting through the high frequencies corresponding to the signal details.

If *x[n]* is the sampled version of original signal, the DWT computes wavelet coefficients and approximation coefficients for *j=1,…, J* given by:

$$c_{j,k} = \sum_{n} x[n] h_j [n - 2^j k] \tag{2.51}$$

and

$$d_{j,k} = \sum_{n} x[n] g_j [n - 2^j k] \tag{2.52}$$

where $h_j \; [n - 2^j k]$ is the analysis discrete wavelet, the discrete equivalent to (2.34) and $g_j \, [n - 2^j k]$ is the scaling sequence, the discrete equivalent to (2.35).

Several application of the decomposition algorithm can be found in literature for denoising purposes [73]-[75].

In particular the DWT decomposition technique [82] has been applied by the author to analyse the working conditions of two different types of marine flexible couplings for boat propulsion. In that work the spectral analysis has proved to be inadequate to show which type of coupling provides a better vibrational behaviour. Therefore, the signals where acquired when the gear was repeatedly changed, revealing a train of impulsive components. In order to localise the impulsive phenomena, the denoising of the signal was needed using the filtering power of the decomposition algorithm.

In this thesis the author applied the DWT algorithm in order to quickly calculate the Temporal Kurtosis of the harvesting machine vibration signature at different scales (frequencies).

2.4.3. Wigner-Ville Distribution (WVD)

Wigner Ville Distribution (WVD) is one of the most widely studied and applied time-frequency analysis methods. It was initially defined in the area of quantum mechanism by Wigner and later extended by Ville to the signal processing.

Let $x(t)$ be a continuous time signal, the Wigner Distribution (WD) of the signal is defined as:

$$W_x(t,f)=\int_{-\infty}^{+\infty} x\left(t+\frac{\tau}{2}\right)\cdot x\left(t-\frac{\tau}{2}\right)^{*}\cdot e^{-j2\pi\tau f}d\tau =$$

$$FT_{\tau\to f}\left\{x\left(t+\frac{\tau}{2}\right)\cdot x\left(t-\frac{\tau}{2}\right)^{*}\right\} \tag{2.53}$$

where FT refers to the Fourier Transform. It can be noted that the WD can be considered as the Fourier Transform of the autocorrelation function.

The WVD, i.e. the WD of the analytic signal, has a very high time-frequency resolution in all the time-frequency domain and has many desirable properties useful for signal analysis.

Some of them are reported below.

- Energy conservation property; the WVD integral over the time-frequency domain gives the signal energy E_x:

$$E_x=\int_{-\infty}^{+\infty}\int_{-\infty}^{+\infty} W_x(t,f)dtdf \tag{2.54}$$

- Marginal properties; the energy spectral density and the instantaneous power can be obtained by the marginal distribution of W_x:

$$\int_{-\infty}^{+\infty} W_x(t,f)dt=\left|X(f)\right|^2 \tag{2.55}$$

$$\int_{-\infty}^{+\infty} W_x(t,f)df=\left|x(t)\right|^2 \tag{2.56}$$

- Real value property; each W_x value in all the time-frequency domain is real;

$$W_x(t,f)\in\mathbb{R},\forall t,f \tag{2.57}$$

- Translation property; the WVD is time-frequency domain covariant:

$$y(t) = x(t - t_0) \Rightarrow W_y(t, f) = W_x(t - t_0, f)$$
$$y(t) = x(t)e^{j2\pi f_0 t} \Rightarrow W_y(t, f) = W_x(t, f - f_0)$$

Since the WVD is a bilinear function, the quadratic superimposition principle says that:

$$W_{x+y}(t, f) = W_x(t, f) + W_y(t, f) + 2\,\mathrm{Re}\left\{W_{x,y}(t, f)\right\} \tag{2.58}$$

where

$$W_{x,y}(t, f) = \int_{-\infty}^{+\infty} x\left(t + \frac{\tau}{2}\right) \cdot y*\left(t - \frac{\tau}{2}\right) \cdot e^{-j2\pi\tau f} d\tau \tag{2.59}$$

is the cross-WVD of the two terms x and y. This concept can be generalized for N components. The cross WVD, the so called cross-term, can hide the auto-terms, making difficult to understand the time-frequency map and invalidating some WVD properties.

In the past several decades, a lot of researchers have tried many methods to reduce the cross-terms interference while keeping the high resolution of WVD. The windowing technique is one of the most popular method to reduce the cross terms influence. Recently, Pachori [83] employed a novel effective technique, called Fourier Bessel Decomposition, in order to reduce the cross term interference.

2.4.4. Remarks

After explaining the theoretical background of the above-defined time-frequency techniques it can be possible to conclude that:

- the CWT technique permits a high resolution at high frequencies and it is a useful tool to detect the presence and the angular localization of the transients;
- the remarkable advantage of the DWT against the CWT is that discrete wavelets can be made orthogonal. This fact permits less redundancy in the DWT map compared with the CWT one;
- the WVD is the time-frequency distribution that presents the highest resolution in both time and frequency domains. So, it can permit a good localization of the time-events at low frequencies.

The main drawbacks concerns the presence of the cross-terms that can hide the auto-terms previously defined.

2.5 Cyclostationary analysis

As we said before, the **non-stationary** signals can be defined as the signals which satisfy a non-property, i.e. they do not satisfy the property of stationarity.

It is not possible to define a general theory which treats non-stationary signals. The non-stationary behavior of each signal has to be individually evaluated.

As already shown, the time-frequency analysis can be considered an useful tool to analyze the amplitude and frequency non-stationarities within a signal. Moreover, the envelope analysis is effective to study the non-stationarities due to the energy variation within a signal.

In that case that a signal presents periodic energy variations and synchronous with the machine cycle a particular class of non-stationary signals can be defined: the cyclostationarity signals.

The theory of the cyclostationarity is developed by Gardner [84] in the telecommunication field and by Antoni in the mechanical field for the diagnosis of rotating machines [23] [85]-[90]. Moreover McCormick et al. gave their contribution in treating signals from rotating machines as cyclostationary [91].

Mathematically, a signal $x(t)$ that satisfies the periodicity of the first two moments, can be considered as a wide sense cyclostationary process:

- first order cyclostationarity

$$m_x(t) = E\{x(t)\} = m_x(t+T) \tag{2.60}$$

- second order cyclostationarity

$$R_{xx}(t_1, t_2) = E\{x(t_1)x^*(t_2)\} = R_{xx}(t_1+T, t_2+T) \tag{2.61}$$

where $E\{\cdot\}$ stands for the expected value and T is the time period.

Since this periodicity is linked with the existence of a basis cycle [89] in rotating machinery, it is more convenient to refer to a cyclic period θ in the angular domain.

Therefore, the equations (2.60) and (2.61) can be expressed in the angular domain as follows:

$$m_x(\vartheta) = E\left\{x(\vartheta)\right\} = m_x(\vartheta+\theta) \tag{2.62}$$

$$R_{xx}(\vartheta_1,\vartheta_2) = E\left\{x(\vartheta_1)x^*(\vartheta_2)\right\} = R_{xx}(\vartheta_1+\theta,\vartheta_2+\theta) \tag{2.63}$$

Each cycle can be considered as a realization of a random process. In order to do so, each realization must begin at an identical angular position.

Then, it is possible to compute an ensemble average (i.e. the average amplitude for a given angle ϑ). that we have previously defined as TSA (i.e. the average amplitude for a given angle ϑ). The TSA permits to extract the "periodic part" (first cyclostationarity order) of the signal and so it is an estimation of the $m_x(\vartheta)$ as follows:

$$\widehat{m}_x(\vartheta) = \frac{1}{N}\sum_{i=0}^{N-1} x(\vartheta+i\theta) \tag{2.64}$$

where $N\theta$ is the length of the signal, N the number of cycles present in the signal.

The quantity

$$\begin{aligned} WVS_x(\vartheta, f) &= E\left\{FT_{\tau\to f}\left\{x\left(\vartheta+\frac{\tau}{2}\right)\cdot x\left(\vartheta-\frac{\tau}{2}\right)^*\right\}\right\} = \\ &= FT_{\tau\to f}\left\{E\left\{x\left(\vartheta+\frac{\tau}{2}\right)\cdot x\left(\vartheta-\frac{\tau}{2}\right)^*\right\}\right\} \end{aligned} \tag{2.65}$$

defines an angular-frequency energy distribution (*FT* refers to the Fourier Transform and *E* is the "ensemble averaging operator") for cyclostationary signals known as the Wigner-Ville Spectrum (WVS).

It can be noted that, the WVS is related to the expected value of the Wigner Ville Distribution (WVD) that was previously defined for a time domain signal.

The main advantage of the WVS over the WVD is that it helps in reducing interference terms.

As previously said, if the components of a signal are deterministic, the WVD exhibits the cross-WVD (i.e. interference terms) between the different frequency components due to its bilinear nature. If now the components are taken as stochastic and independent (i.e. second order cyclostationary), it is easy to prove that the cross-Wigner-Ville Spectrum is identically zero. So, the WVS can be considered a linear operator.

In addition, the suppression of the interference between the different signal components removes most of the possible negative values of the distribution. Hence interferences are also smoothed out by the “ensemble average” while preserving the angular-frequency resolution intact.

Antoni [23] interprets the WVS (under the assumption of non-negativity) as the Probability Density Function (PDF) of the frequency random variable v vs. the angular position variable ϑ.

Because of this, the WVS can be described by its “spectral” moments.

The *n*th spectral moment is defined as:

$$m_n^x(\vartheta) = \int_0^\infty WVS_x(\vartheta, \nu)\nu^n d\nu \tag{2.66}$$

Antoni proves [92] that the spectral moments can be obtained from the following formulation

$$m_n^x(\vartheta) = (2\pi j)^{-n} \frac{\partial^n \ln K}{(\partial \tau)^n}(\vartheta, 0) \tag{2.67}$$

where *K* is the autocovariance function of the analyzed signal

The estimated sampled Mean Instantaneous Power (MIP) can be obtained directly from the angular sampled signal:

$$\hat{m}_0^x[m] = \left\langle \left| X_a[m] \right|^2 \right\rangle_N^I \qquad m = 0, \ldots, N-1 \tag{2.68}$$

with X_a the analytic signal where $\langle |\cdot| \rangle_N^I$ means averaging over I cycles of length N samples of a single measurement.

In order to make quantitative evaluations about capabilities of the cyclostationary analysis in processing signals derived from I.C. engines, a synthesised signal is analytically formulated and presented in Chapter 3.

2.6 Non stationary component extraction using Spectral Kurtosis (SK)

The characterization of non-stationary components within a faulty signal is usually achieved by means of statistical indicators that are sensitive to the peakedness of the signal. For instance the Temporal Kurtosis (TK) and the Crest Factor (CF) are particularly well suited to this purpose. This is in contrast to the RMS value, for example, which can only characterize the mean level of the signal but does not provide information on the temporal variations of its envelope.

As mentioned in [93], the Temporal Kurtosis (TK) takes (i) high values in the presence of impacts whereas (ii) it is ideally zero when only background noise is present. The first condition (i) is true when the impulse responses generated by the impacts are sufficiently well separated and when the signal to noise ratio is sufficiently high. The second condition (ii) is true whenever the background noise can be assumed Gaussian as a result of the superposition of a large number of independent (stationary) sources. In practice these conditions are rarely satisfied.

The Spectral Kurtosis (SK) is a spectral statistic which helpfully supplements the classical PSD: it ideally takes zero values at those frequencies where only the stationary Gaussian noise is present, high positive values at those frequencies where the transient occurs, negative values in presence of harmonic components.

Therefore the SK seems to be an useful tool to detect non-stationary components hidden by the background noise.

The idea is very simple: computing the SK and checking in each frequency band for abnormally high values which may suggest the presence of a non-stationary component.

The Spectral Kurtosis was first introduced by Dwyer as a statistical tool which “can indicate not only non-Gaussian components in a signal, but also their locations in the frequency domain”. Dwyer originally defined the SK as the normalised fourth-order moment of the real part of the STFT.

A more formal definition of SK in light of the theory of higher-order statistics. Capdeville defined the SK as the normalised fourth-order cumulant of the Fourier transform and used it as a measure of a distance of a process from Gaussianity.

Other investigations were carried out by Vabrie [94], who proposed some interesting applications to the characterization of harmonic processes.

The SK of **non-stationary** processes was formalized by Antoni by means of the Wold-Cramer decomposition of ‘conditionally non-stationary” processes [96].

De la Rosa et al. [97] used the SK in order to detect the termite emissions.

Antoni establishes to which extent the SK is capable of detecting transients in the presence of strong additive noise and propose a STFT based estimator of the SK which helps to link theoretical concepts with practical applications.

The estimator proposed by Antoni, that is deduced from a time-frequency approach, shares close similarities with the historical definition of the SK of Dwyer and it is also very similar to the estimator proposed by Vabrie. The estimator proposed by Vabrie is defined as follows:

$$\widehat{K}_x(m) = \frac{M}{M-1}\left[\frac{(M+1)\sum_{i=1}^{M}\left|X_i(m)\right|^4}{(\sum_{i=1}^{M}\left|X_i(m)\right|^2)^2} - 2\right] \tag{2.69}$$

The signal is divided into *M* blocks with 75% of overlap, each of length *N*. The percentage of overlap of 75% can be considered the correct setting to safely remove bias in the computation of the SK. A *N*-

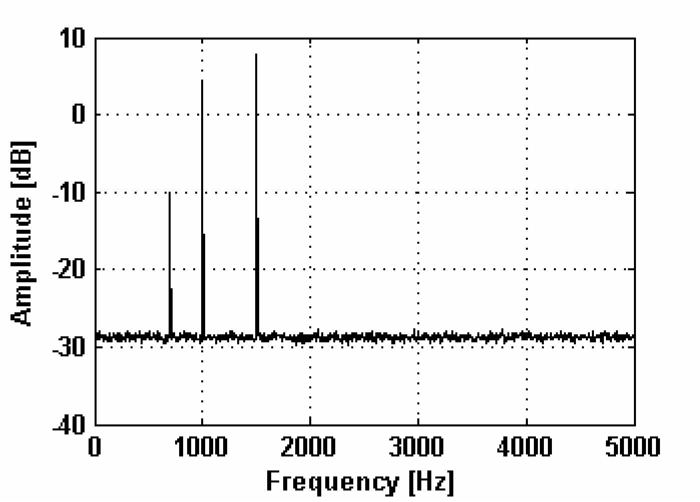

Fig. 2.21 – PSD of the test signal.

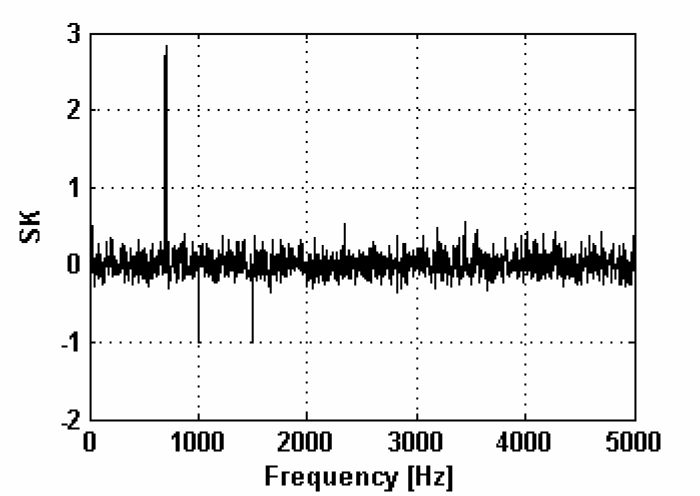

Fig. 2.22 – SK of the test signal.

point DFT is performed on each segment giving the random variable $X_i(m)$, *(i=1,…,M)* that is the DFT amplitude at the frequency *m*.

The main problem regarding the application of the SK estimation for a real case is the choice of the time window length N.

In order to overcome these limitations, Antoni and Randall [93] proposed the application of the so called "kurtogram" that is the map formed by the STFT-based SK as a function of f (central frequency of the narrow band filter) and N_w (length of the time window).

However, the original algorithm used for estimated the kurtogram had a prohibitive computational cost and hence offered limited industrial potential.

Because of this fact, Antoni [98] proposed a fast computation of the kurtogram based on a particular filter-bank structure.

In order to show the capabilities of the SK formulated in (2.69) a test signal has been formulated. It is composed by the following components:

- two sine wave of frequency 1000 and 1500 Hz;
- a non stationary component consisting of a sine wave of frequency 700 Hz with a zero mean Gaussian amplitude modulation;
- a white Gaussian noise.

These different components can be visualized in the PSD and the corresponding SK, respectively shown in Fig. 2.21 and Fig. 2.22. These two spectral quantities were calculated by using N = 3000-points DFT calculation and M = 200 unoverlapped blocks.

As expected, the SK estimator is a function of the nature of the signal. As clearly depicted in Fig. 2.22, it assumes positive values at the frequency of the non-stationary component (i.e. 700 Hz) and negative values at the frequency of the stationary ones (pure sine waves at 1000 and 1500 Hz).

Chapter 3

CONDITION MONITORING AND DIAGNOSIS IN I.C. ENGINE COLD TESTS

3.1 Introduction

This Chapter addresses the use of several signal processing tools as a means for the monitoring and the diagnosis of assembly faults in I.C. engines through the cold test technology. Firstly, an approach based on the use of symmetrized dot patterns for the visual characterization of vibration signatures is proposed. This method is applied in order to obtain reliable thresholds for the pass/fail decision after the cold test. Secondly, the fault identification is discussed on the basis of the cyclostationary modelling of the signals. First of all, first-order cyclostationarity is exploited through the analysis of the Time Synchronous Average (TSA). Subsequently, second-order cyclostationarity is developed by means of the mean instantaneous power, Wigner-Ville Distribution (WVD) and Wigner-Ville Spectrum (WVS). Thirdly, the Continuous Wavelet Transform (CWT) is presented and compared with the Wigner Ville Distribution. Eventually, an approach based on the analysis of the Instantaneous Speed (IAS) is discussed. The effectiveness and the limitations of the above-mentioned techniques and diagnostic procedures applied to three considered assembly faults are compared and discussed on the basis of experimental results.

The Chapter is organized as follows. Section 3.2 describes the experimental apparatus, the test conditions and the artificially introduced faults. Furthermore the characteristics of the engine vibration are introduced. Section 3.3 considers a simplified dynamic model of a mono-cylinder engine in a non-combustion state in order to estimate the forces acting on the rod during one engine cycle. Section 3.4 concerns the application of the image correlation method in order to find reliable thresholds for the pass-fail decision. Section 3.5 shows the cyclostationary model capabilities in localizing the assembly faults under study. Section 3.6 illustrates some achievements obtained by means of the Instantaneous Angular Speed analysis.

3.2 Experimental apparatus and test conditions

Experimental investigations are carried out on a 2.8 L engine produced by VM Motori, 4-cylinder 4-stroke with four-valve-per-cylinder, turbocharged with an exhaust-driven turbo-compressor. The engine has the following technical specifications:

As previously said, the measurements are carried out through the cold test technology in which the engine is driven by an electric motor via a coupling unit and therefore it is maintained in a non-combustion state.

The results presented in this thesis deal with two different crankshaft speeds: the PSD calculation and the image correlation method was applied to signals extracted at 120 rpm while the cyclostationary and time-frequency analysis have been carried out on signals extracted at 1000 rpm. The vibration signal is measured by means of a piezoelectric general purpose accelerometer (MTN 1020; frequency range: 2-13 kHz) mounted on the engine block (turbocharger side) close to the bearing support of the crankshaft. The sample frequency was 14 kHz and the duration of the vibration signal acquisition was 2 s. The tachometer signal which measures the

Table 4 – Diesel engine technical specifications.

	2.8 L diesel engine		
Piston rod length	L	[m]	0.159
Crank radius	r	[m]	0.05
Piston mass	m_s	[kg]	1.11
Piston rod mass	m_b	[kg]	1.2
Cylinder bore	D	[m]	0.094
Compression ratio			17.5
Rotating speeds		[rpm]	120 and 1000
Firing order			1-3-4-2

rotational position of the engine is generated using an encoder with 360 pulse/rev mounted between the coupling unit and the clasp.

During the acquisition, the vibration signal is resampled with an angular resolution of 1 degree. Since the instantaneous speed has some fluctuations around the mean, the number of time samples varies from cycle to cycle, while the angular resampled signal is independent of the speed variations and can be used to compute the Time Synchronous Average (TSA) over 16 time histories, each corresponding to two crankshaft rotations (720^{o}), in order to respect the periodicity of a 4-stroke engine.

In order to evaluate the vibration signal diagnostic capabilities tests were carried out with different types of fault.

In this thesis three specific faulty conditions are discussed and compared:

- Piston rod with screw pre-load of only 3 kgm, instead of the correct torque of 9 kgm (RS3 engine) – Fig. 3.1 (a). This fault causes an irregular rotation of the rod and, consequently, an incorrect stroke of the piston, this affecting the engine operations. The faulty rod is connected to the piston 3.

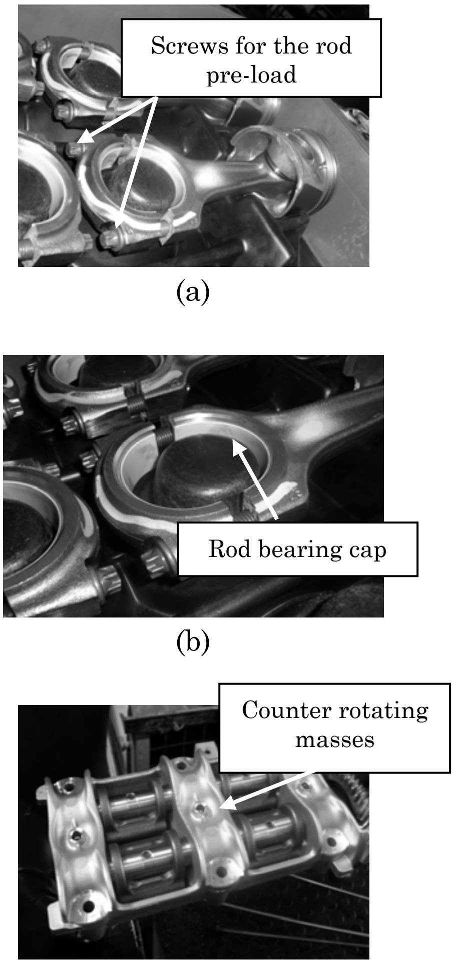

(a)

(b)

(c)

Fig. 3.1 – Mechanical devices involved in 3 faulty conditions under study.

- <u>Piston rod without a bearing cap (RC4 engine)</u> – Fig. 3.1 (b). The absence of the bearing cap causes big hits and an irregular rotation of the piston rod. The faulty rod is connected to the piston 4.
- <u>Counter-rotating masses mounted with a phase lag (CRM engine)</u> – Fig. 3.1 (c). The counter-rotating masses may be assembled with a 180 degrees phase distortion. It is worth noting

that the correct phase position of the counter rotating weights is necessary for the correct balance of the inertial forces due to the motion of the piston.

Experiments were performed over engines in sound and faulty conditions by means of two different investigations in two different days: for the second test investigation the accelerometer position was slightly changed but still close to the crankshaft bearing support.

The engines with faulty rods have been tested during the first investigation whilst the engine with the wrong assembled masses has been tested during the second investigation.

3.3 Dynamic model of a mono-cylinder engine in a non-combustion state

This Section is devoted to the analysis of the dynamics of a single-cylinder engine. This kind of analysis has been carried out in order to calculate the piston rod forces against the crankpin.

As a simplification, it is assumed that:

- the engine is running at a constant crankshaft speed;
- the gravitational forces and friction forces can be neglected in comparison to the dynamic forces effects;
- the cold test conditions allow us to neglect the gas forces and only consider the forces due to the pressurization when both the intake and exhaust valves are closed.

We can designate the crank angle as $\alpha = \omega t$, taken positive in the clock-wise direction, and the piston rod angle as γ, also taken positive in the clock-wise direction.

The crank angle α is assumed positive starting from the TDC at the beginning of the intake stroke.

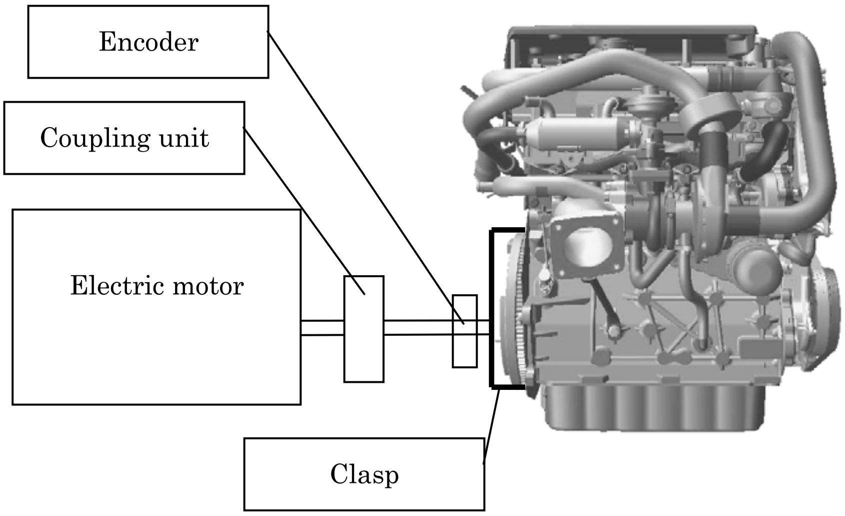

Fig. 3.2 – Cold test bench and data acquisition system.

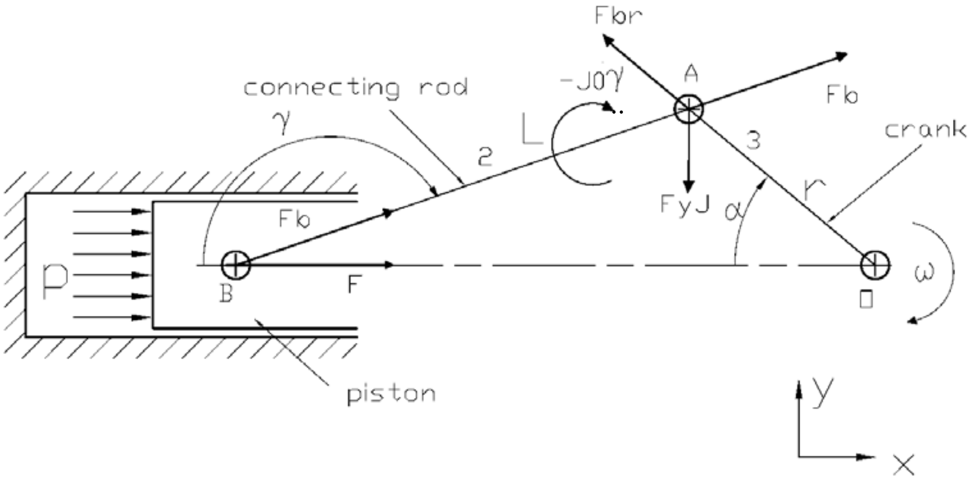

Fig. 3.3 – Dynamic model of a single-cylinder engine: global coordinate system *x-y*.

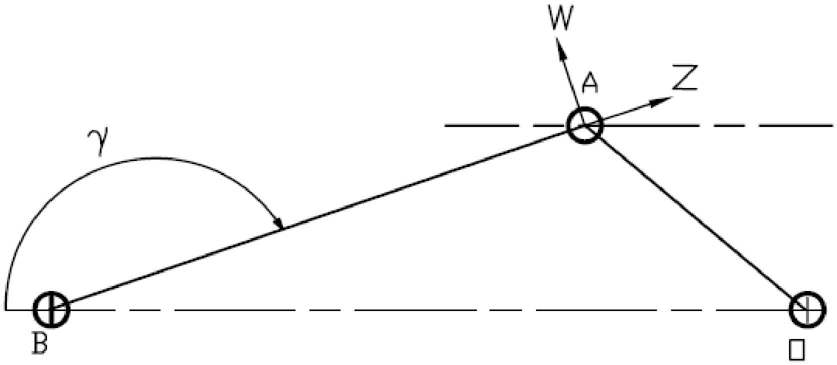

Fig. 3.4 – Local coordinate system (*z-w*) integral with the piston rod.

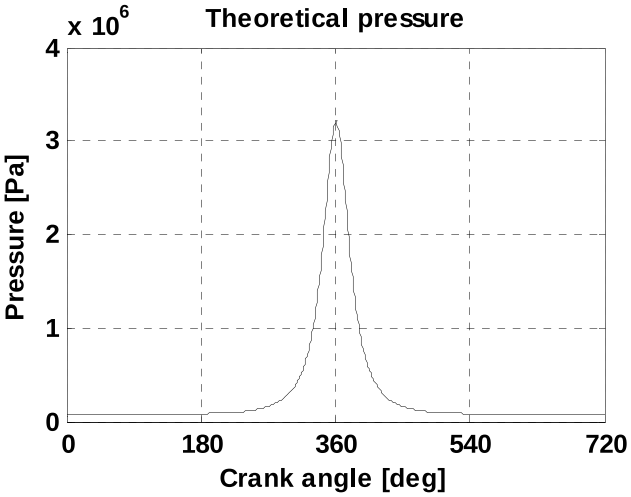

Fig. 3.5 – Theoretical air pressure within the combustion chamber.

The relation existing between these two angles can be observed from the Fig. 3.3:

$$L \sin \gamma = r \sin \omega t \tag{3.1}$$

where $\lambda = \frac{r}{L}$.

The pressurization force acting against the piston is:

$$F_p = (p_p(\alpha) - p_0)\frac{\pi D^2}{4} \tag{3.2}$$

where D is the cylinder bore, p_0 is the pressure inside the engine block (supposed as the atmospheric pressure) and $p_p(\alpha)$ is the theoretical pressurization in the combustion chamber calculated through the polytrophic process law:

$$pv^n = \text{cost} \tag{3.3}$$

with p as the pressure, v the volume and n the polytrophic index. In this work we will assume $n = 1.27$. The theoretical pressure is depicted in Fig. 3.5.

The inertial forces acting on the rod can be divided in alternative and rotating inertial forces:

- the alternative inertial force is given by:

$$F_a = -m_a a \tag{3.4}$$

with $m_a = m_s + m_{ba}$ where m_s is the piston mass and m_{ba} is the rod equivalent alternative mass supposed located at the wrist pin. The explicit relation after calculating the acceleration is given by the following expression:

$$F_a = F_a^{'} + F_a^{''} = -m_a \omega^2 r(\cos\alpha + \lambda\cos 2\alpha) \tag{3.5}$$

with $F_a^{'}$ as the first order inertial force term and $F_a^{''}$ is the second order inertial force term. It can be noted that the latter varies at twice the crankshaft speed.

- the rotating inertial force is given by:

$$F_{br} = m_{br}\omega^2 r \tag{3.6}$$

with m_{br} the piston rod equivalent mass supposed located at the crankpin.

Referring to a **global coordinate system** depicted in Fig. 3.3 the *x* and *y* components of the rotating inertial force are:

$$F_{brx} = -F_{br}\cos\alpha \tag{3.7}$$

$$F_{bry} = F_{br}\sin\alpha \tag{3.8}$$

- the rod inertial torque $-J_0\ddot{\gamma}$ is due to the equivalent moment of inertia J_0, computed in order to obtain an inertial system (m_{ba}, m_{mr}, J_0) dynamically equivalent to the rod inertia; it can be represented by a couple of forces in y directions applied to the rod in A and in B; in particular, considering $\ddot{\gamma} \cong \omega^2 \lambda \sin\alpha$, the force applied in A is:

$$F_{Jy} = -\omega^2 r \frac{J_0}{L^2} \frac{\sin\alpha}{\cos\gamma} \tag{3.9}$$

The inertial system equivalent to the rod inertia is approximately computed as $m_{ba} = m_{br} = \frac{m_b}{2}$, $J_0 = -\frac{m_b L^2}{6}$, where m_b is the rod mass.

Referring to a **local coordinate system** integral with the p rod (see Fig. 3.4**)**, the *z* and *w* components of the total force transmitted by the piston rod against the crankpin are given by:

$$\begin{aligned} F_z &= -F_{brx}\cos\gamma + F_{bry}\sin\gamma - \frac{F}{\cos\gamma} + F_{Jy}\sin\gamma \\ &= -F_{brx}\cos\gamma + F_{bry}\sin\gamma + F_b + F_{Jy}\sin\gamma \end{aligned} \tag{3.10}$$

$$F_w = -F_{brx}\sin\gamma - F_{bry}\cos\gamma - F_{Jy}\cos\gamma \tag{3.11}$$

where $F = F_a + F_p$ and is $F_b = F/(-\cos\gamma)$ the component of F acting on the rod and directed as *z*-axis. Therefore the resultant force in the **local system** is:

$$R_{zw} = \sqrt{F_z^2 + F_w^2} \tag{3.12}$$

and it is plotted in Fig. 3.6.

Table 5 – Crank angles in the position indicated in Fig. 3.6 and Fig. 3.7.

Points	Crank angle values α [deg]
A	0
1	80
B	180
C	360
2	640

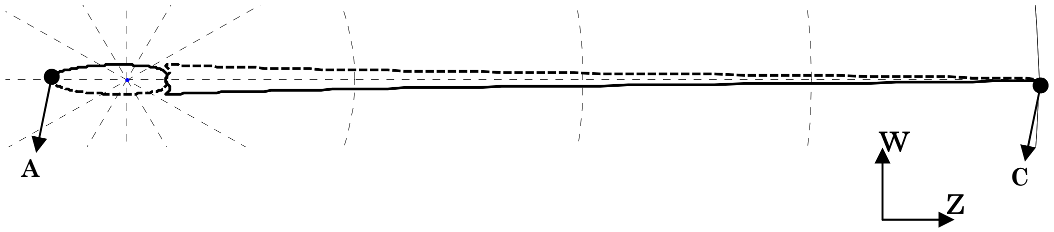

Fig. 3.6 – Polar graph of the R_{zw} force transmitted by the rod against the crankpin during two crankshaft revolutions: first crankshaft revolution (solid line) and second crankshaft revolution (dashed line).

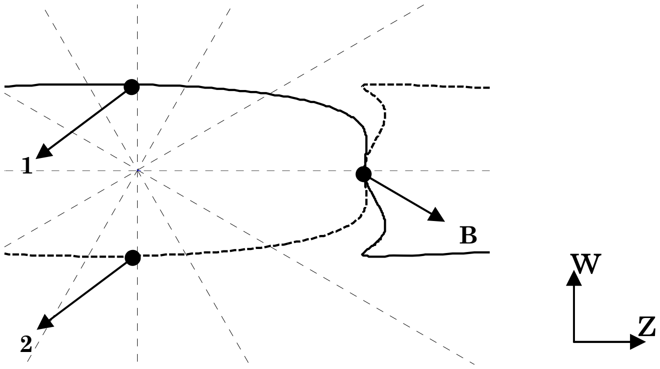

Fig. 3.7 – Zoom of the polar graph depicted in Fig. 3.6.

Table 5 indicates the correspondent crank angle references. We call B the point at $\alpha = 180^\circ$ when the intake valve closure happens during the first crankshaft revolution.

It can be noted that the z component of the resulting force changes its direction two times during 2 crankshaft revolutions ad assumes the highest amplitude in the positive z –axis direction at $\alpha = 360^\circ$ when the highest value of the air pressure in the combustion chamber is reached.

3.4 Condition monitoring

3.4.1. Frequency domain

The commercial online monitoring and diagnostic systems exhibit implemented techniques in the frequency domain for processing vibration signals in order to obtain reliable cold-test pass/fail procedures. This is because the analysis are easy to understand by a majority of vibration experts who are practice than theory oriented. Because of this fact the capabilities of a basic frequency domain technique has been verified.

For each signal the PSD spectra is obtained by averaging the PSD amplitudes on 7 sets with Hanning window, using bandwidth of 5580 Hz and frequency resolution of 3.48 Hz. Then, the mean value of the PSD in the highest amplitude range is calculated and compared for both sound and faulty signals.

As an example, observing Fig. 3.8, one can notice the clear differences in amplitudes between normal and faulty conditions in the range 4000-5000 Hz for runs carried out at 120 rpm where the background noise is less relevant.

Table 6 and Table 7 show the PSD mean values in the range 4000-5000 Hz for both experimental investigations.

As a result this parameter seems to be an effective monitoring feature for all three faulty conditions. Concerning the first investigation 21 healthy engines have been tested. Therefore the mean value and standard deviation were calculated averaging over 21 values. Regarding the second investigation, it is worth noting that only a healthy engine is tested and so the 3 sigma confidence level is not available.

It can be concluded that if PSD's presenting low background noise and a clear resonance band can be obtained, the mean value calculated over the highest amplitude range can be considered as an useful monitoring tool.

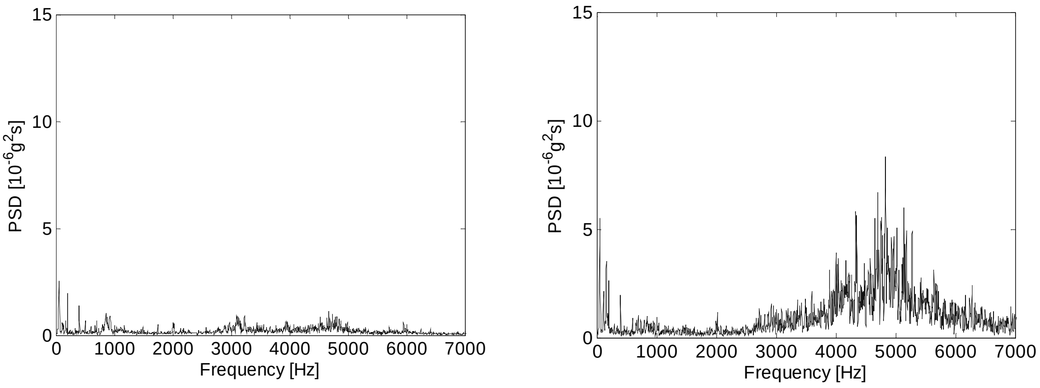

(a) (b)

Fig. 3.8 – First experimental investigation (120 rpm); PSD of the engine block acceleration in (a) healthy and (b) faulty condition (RS3 engine).

Table 6 – First experimental investigation: PSD mean value.

Engine	PSD mean value in 4000-5000 Hz [$10^{-6}g^2s$] 120 rpm
Mean + 3 Sigma for normal engines	0.51
Faulty RS3 engine	**2.45**
Faulty RC4 engine	**0.93**

Table 7 – Second experimental investigation: PSD mean value.

Engine	PSD mean value in 4000-5000 Hz [$10^{-6}g^2s$] 120 rpm
Normal engine	0.23
Faulty CRM engine	**13.50**

3.4.2. Symmetrized Dot Pattern (SDP) method

As was mentioned in Chapter 2, the SDP method transforms one time domain signal in a highly symmetrized image in order to develop a simple pattern recognition technique. The goal is to identify a reference pattern that represents the normal engine condition and then compare it with the images obtained from all the tested engines. The final purpose is to identify a similarity parameter, called correlation, that has been chosen as the percentage of common white pixels with respect to the total number of white pixels in the healthy engine pattern. This was carried out by using the edge detection algorithm described in Chapter 2.

In order to set the detection threshold for the correlation, first of all this parameter is calculated for all couples of engines among a group of 21 healthy engines: the engine that presents the minimum correlation with each other is assumed as the reference pattern, unique for all investigations. The corresponding minimum correlation of 25.08% is fixed as the correlation threshold (CT).

This pattern is compared with the images obtained from different faulty engines and so the correlations are calculated, verifying if they are lower than the CT in order to discriminate the faulty condition from the normal one. Fig. 3.9 and Fig. 3.10 show the images obtained for the reference pattern and for the RS3 engine respectively.

The results concerning the fault detection for the three faulty engines analyzed and collected in Table 8 show that all the faulty engines give a percentage of common white pixels lower than the CT. Actually, it seems that this technique exhibits high sensitivity to the fault detection presenting some advantages: fast computational implementation and easy output evaluation. Compared to the PSD technique, the SDP technique does not need to calculate the spectra of the signal and it consists in a comparison between two images without any difficult for a technician in computing and interpreting a spectra. Moreover the technician does not have to check if the background noise

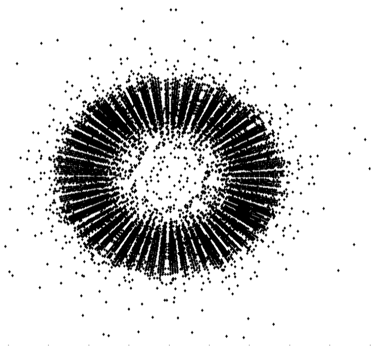

Fig. 3.9 – Symmetrized Dot Polar graph: Healthy engine (reference pattern).

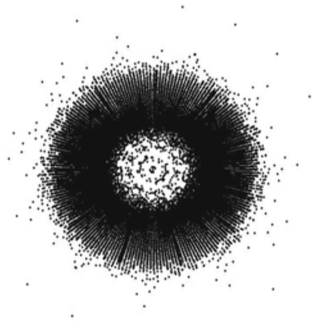

Fig. 3.10 – Symmetrized Dot Polar graph: faulty engine (pre-loaded rod: RS3).

is present as he has to do for the analysis of the highest-amplitude PSD band.

Table 8 – Symmetrized patterns: correlation values.

Comparison between symmetrized patterns	Percentage of common white pixels [%]
Healthy engine - Healthy engine	25.08 (CT)
Healthy engine - Faulty RS3 engine	10.80
Healthy engine - Faulty RC4 engine	21.83
Healthy engine - Faulty CRM engine	22.07

3.5 Fault diagnosis

3.5.1. Cyclostationary and time-frequency analyses

3.5.1.1 Cyclostationary techniques: application to a signal model

In order to make quantitative considerations about the cyclostationary analysis capabilities, a signal model, that realistically mimics the vibration signal measured from the cold test, is firstly analytically formulated:

$$x(t) = x_d(t) + x_{nd}(t) + x_s(t) \tag{3.13}$$

where $x_d(t)$ and $x_{nd}(t)$ are respectively the deterministic and the non-deterministic part.

The non-deterministic part $x_{nd}(t)$ considers the random fluctuations around $x_d(t)$, while $x_s(t)$ takes into account the background noise.

The deterministic part $x_d(t)$ is first-order cyclostationary:

$$x_d(t) = x_d(t+T) \tag{3.14}$$

and $x_{nd}(t)$ is set to be second-order cyclostationary respecting the following condition expressed in terms of autocovariance function $K_{x_{nd}x_{nd}}$:

$$K_{x_{nd}x_{nd}}(t,\tau) = K_{x_{nd}x_{nd}}(t+T,\tau)$$

where T is the non-random period.

The autocovariance function is expressed by:

$$\begin{aligned} K_{x_{nd}x_{nd}}(t,\tau) &= E\left\{x_{nd}(t+\tau/2)x_{nd}(t-\tau/2)\right\} - \\ &-\mu_{nd}(t+\tau/2)\mu_{nd}(t-\tau/2) \end{aligned} \tag{3.15}$$

where μ_{nd} is the mean of the non deterministic part $x_{nd}(t)$.

The deterministic part can be modelled as a series of impulse response functions such as:

$$x_d(t) = \sum_{k=1}^{N} x_{dk}(t) \tag{3.16}$$

$$\text{with} \begin{cases} t < t_{impk} \rightarrow x_{dk}(t) = 0 \\ t \geq t_{impk} \rightarrow x_{dk}(t) = e^{-(t-t_{impk})/\sigma_k} X_{dk} \cos[2\pi f_{impk}(t - t_{impk})] \end{cases}$$

where X_{dk} and t_{impk} define respectively the amplitude and the time of the k^{th} engine event, whilst σ_k is the time constant related to the damping factor of the k^{th} impulse response.

The non-deterministic signal counterpart is modelled as a cyclic impulse modulated noise, such as:

$$x_{nd}(t) = \sum_{k=1}^{N} x_{ndk}(t) \tag{3.17}$$

$$\text{with} \begin{cases} t < t_{impk}, t > t_{imp(k+1)} \rightarrow x_{ndk}(t) = 0 \\ t_{impk} \leq t < t_{imp(k+1)} \rightarrow x_{ndk}(t) = X_{ndk} e^{-(t-t_{impk})/\sigma_k} n(t) \end{cases}$$

where *n(t)* is a normally distributed random noise of zero mean and standard deviation one, whilst t_{impk} and σ_k are defined as above; $x_s(t)$ is still modeled as a normally distributed random noise with zero mean and standard deviation one.

The specific values of the parameters used in the signal model synthesis are listed in Table 9 and Table 10.

It can be noted that the physical periodicity of the engine events really belongs to the crankshaft angle and not to time. Therefore the angular signal is well suited for the cyclostationary modelling. So, the vibration signal model of Eq. (3.13) can be expressed as follows:

$$x(\theta) = x_d(\theta) + x_{nd}(\theta) + x_s(\theta) \tag{3.18}$$

where θ is the crankshaft angular position.

Following this model, the WVD and WVS will be applied in the angle domain, although the above-reported formulation has been treated in the time domain.

Moreover both representations will be plotted scaling frequency in Hz rather then in deg^{-1}. This fact makes sense because a constant engine speed is assumed (1000 rpm).

Table 9 - Vibration signal model: deterministic part.

k	**1**	**2**	**3**	**4**
X_{dk}	2	2	2	2
σ_k [s]	0.0017	0.0017	0.0017	0.0017
t_{impk} [s]	0	0.031	0.062	0.093
f_{impk} [Hz]	4000	4000	4000	4000

Table 10 - Vibration signal model: non-deterministic part.

k	**1**	**2**	**3**	**4**	**5**
X_{ndk}	0.5	2	0.5	0.5	0.5
σ_k [s]	0.0017	0.0017	0.0017	0.0017	0.0017
t_{impk} [s]	0	0.0155	0.031	0.062	0.093

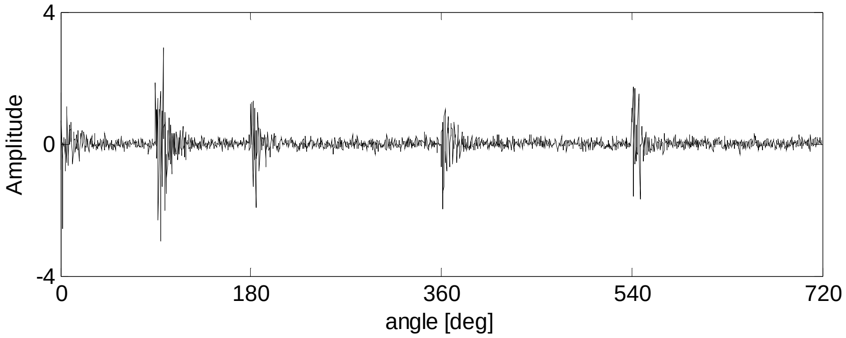

Fig. 3.11 – IC engine vibration signal model considering only pressurization, inertial forces and an impulsive component.

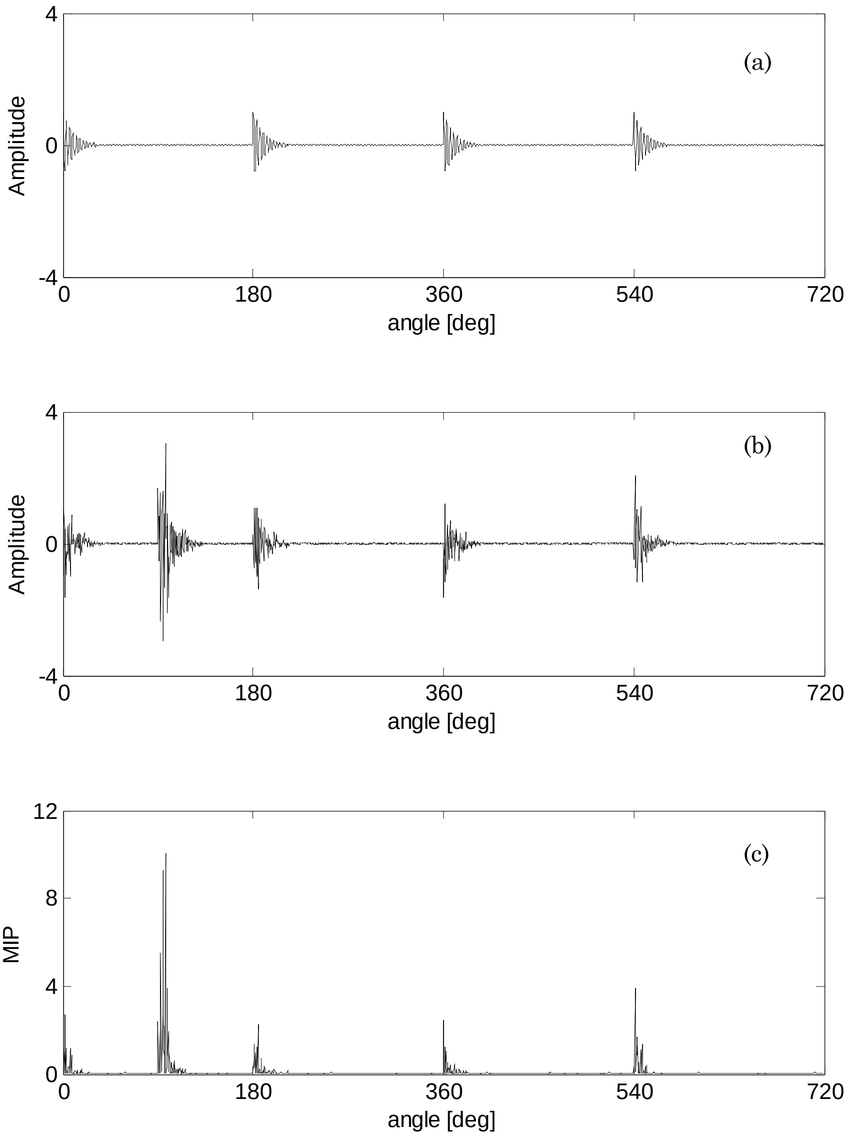

Fig. 3.12 – Model of I.C. engine vibration signal, considering only pressurization, inertial forces and an impulsive component: (a) deterministic part; (b) cyclostationary part; (c) mean instantaneous power of the residual signal.

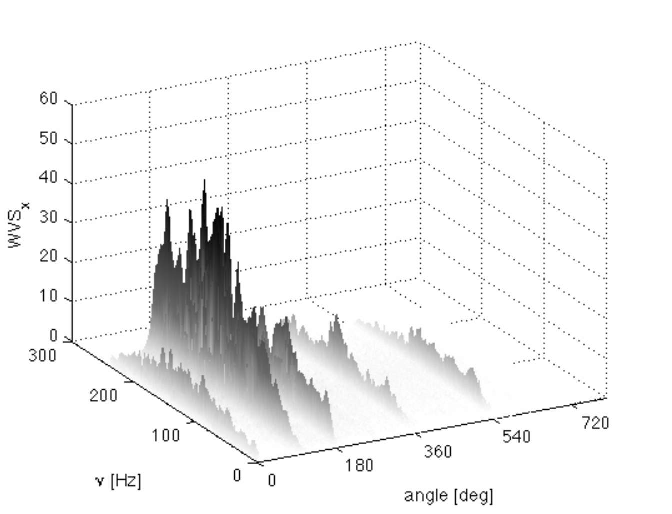

Fig. 3.13 – WVS of the cyclostationary part depicted in Fig. 3.12 (b).

Due to the fact that the measurements are carried out in a non-combustion state, the vibration signal model only considers the engine pressurization and inertial forces in healthy conditions.

In order to simulate a faulty condition, an impulsive component is added to the non-stationary signal counterpart and simulated as an impulse response (see Table 10, k=2). The result is shown in Fig. 3.11.

The signal model (see Fig. 3.12) was considered satisfactory to point out the different contributions of the deterministic and cyclostationary parts on the total signal.

Moreover the computation of the mean instantaneous power of the residual signal seems to be effective in highlighting the presence and the angular location of a generic fault.

3.5.1.2 CWT optimization using TDAS: application to a signal model

This Section is devoted to the application of the TDAS (Time Domain Across the Scales) method on the same simulated signal previously used to illustrate the cyclostationary analysis capabilities. The TDAS is a technique developed by Halim [47] that combines both wavelet analysis and angular domain average in order to improve the time-frequency representation of the TSA of a signal. While the traditional method consists in taking wavelet transform of the Time Synchronous Average, this new method performs the wavelet transformation first and then takes the time synchronous averages obtaining the so-called TDAS distribution. Assuming that the period of a time series is P and the time series has exactly M periods, the number of the total time samples is $N=P$ x M. If the number of wavelet scales s is S the wavelet transformation of the time series generates the complex matrix CWT (because both complex Morlet and Impulse mother wavelets have been used in this work) of S x N dimensions. It can be noted that each row of the absolute value of the CWT matrix is a time series corresponding to one scale s with period P. If each of these time series is synchronously averaged (based on the period of the time series) the average of all the time series across all scales can be computed obtained the final TDAS matrix. Each of the row of the TDAS matrix represents the time synchronous average of the time series located at each scale.

This method has the following advantages:

- it permits a powerful detection of close frequencies due to the fact that the absolute value of the complex number obtained after the wavelet transformation has been obtained before the averaging. In fact frequency detailed information could be lost if the wavelet transformation is computed after the averaging process;
- it permits a higher noise reduction due to the improvement of the matching mechanism of the wavelet transform operator;
- it gives a higher wavelet transformation resolution due to the higher number of samples processed since the transformation is computed over the entire time series.

On the basis of these considerations, this method appears to be helpful when a lower number of averages is available.

It is worth noting that Halim obtained the TDAS matrix using a geometric average and the Morlet wavelet as a basis. In this work, the effectiveness of the method using the Impulse mother wavelet is verified and the linear average is also taken into account in order to be consistent with the traditional method.

Hereafter the influence of the background noise over the time-frequency representation will also be considered. This aspect was not previously considered when the WVS of the signal model was calculated.

In order to evaluate the TDAS method capabilities a time series having 16 periods is generated. Each signal period contains the same vibration components of the signal model formulated by Eq. (3.18). Next, this signal has been corrupted by adding noise such that the signal to noise ratio is 1 dB.

Concerning the traditional method, it can be shown from Fig. 3.14 that the CWT of the TSA by using the Impulse mother wavelet clearly indicates the four deterministic peaks due to the four pressurizations within the engine cycle. Moreover it is possible to observe the peak due to the occurrence of the fault even if it appears less clear than the others. The appearance of this peak, that is basically stochastic, can be probably due to the very close angular occurrences of the peak in different angular periods. Moreover the low number of averages computed to perform the TSA can be not considered sufficient to neglect that stochastic impulse component. By observing Fig. 3.15 it can be noted that the traditional method is very sensitive to the presence of background noise since all the events are masked by the noise. On the contrary, Fig. 3.16 clearly shows the existence of the transient due to the fault occurrence: it spans within all the frequency range.

By means of TDAS, that performs a time synchronous average at each scale, the fine details of the frequency information can not be lost. Because of this fact the TDAS clearly detects the presence of the fault in the entire frequency range analyzed.

Fig. 3.17, Fig. 3.18 and Fig. 3.19 show the comparison between the traditional and TDAS methods obtained using the Morlet Wavelet. Concerning the robustness to the noise and the frequency resolution of the 3D map the same results obtained using the Impulse wavelet can be achieved.

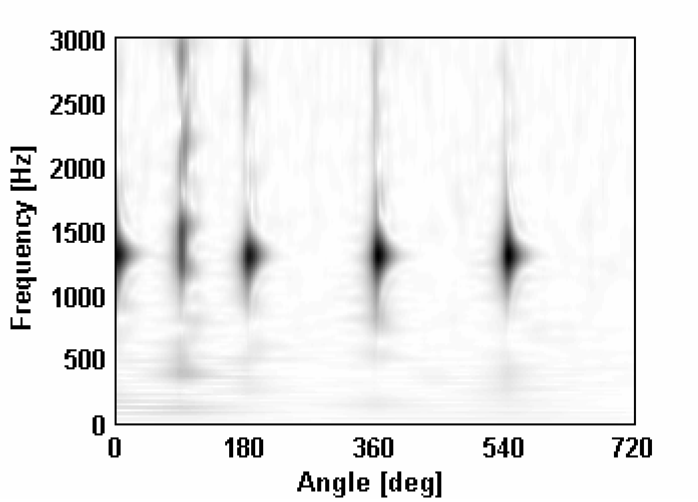

Fig. 3.14 – CWT (traditional method - impulse wavelet) of the TSA (16 averages) of the raw signal model.

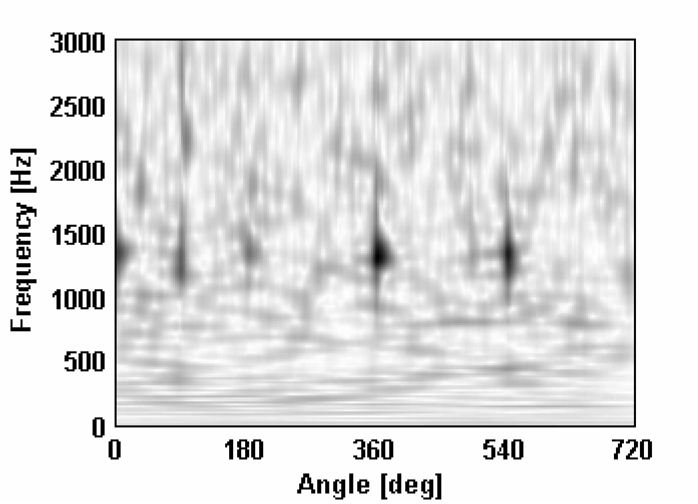

Fig. 3.15 – CWT (traditional method - impulse wavelet) of the TSA (16 averages) of the raw signal model after adding noise (SNR=1 dB).

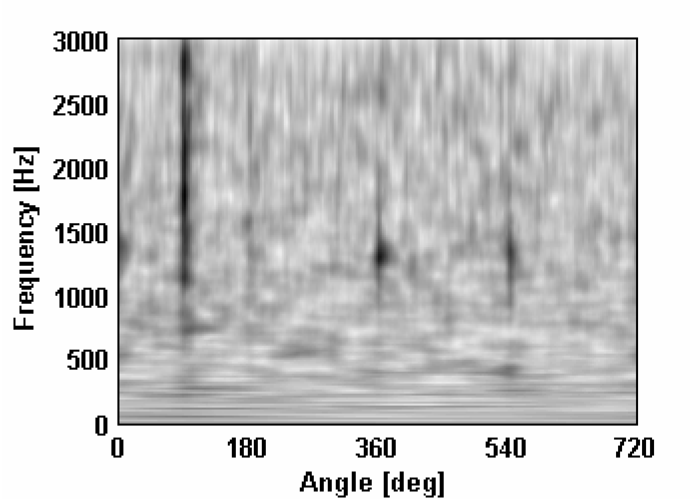

Fig. 3.16 – TDAS using linear average (impulse wavelet) of the raw signal model after adding noise (SNR=1 dB).

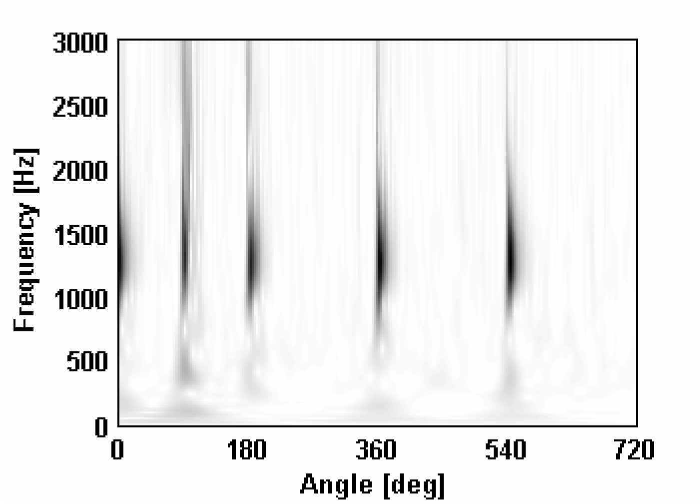

Fig. 3.17 – CWT (traditional method - morlet wavelet) of the TSA (16 averages) of the raw signal model.

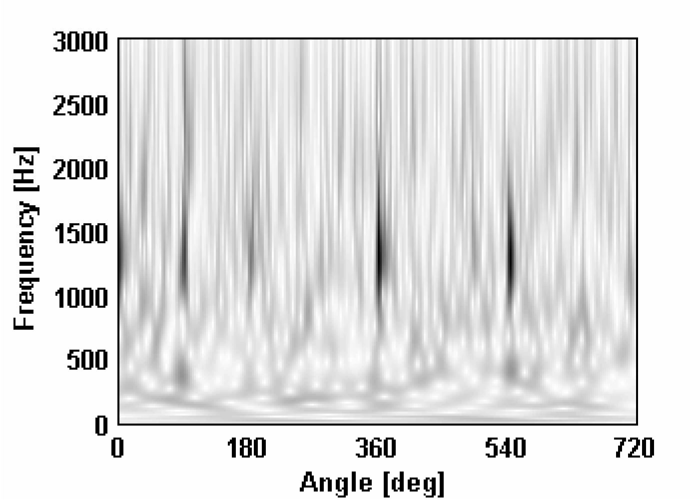

Fig. 3.18 – CWT (traditional method - morlet wavelet) of the TSA (16 averages) of the raw signal model after adding noise (SNR=1 dB).

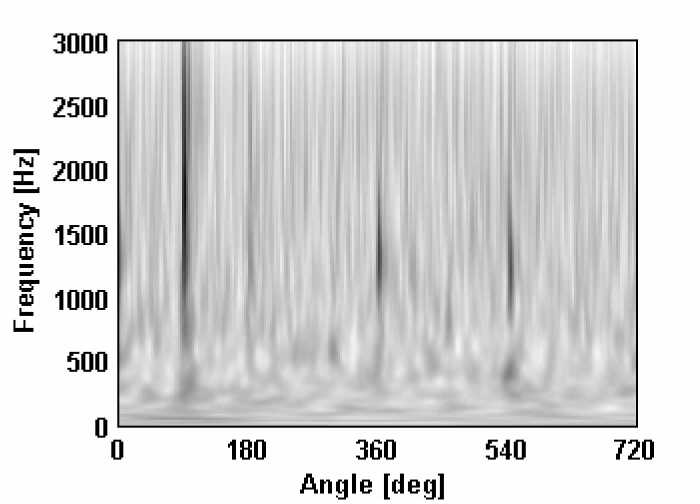

Fig. 3.19 – TDAS using linear average (morlet wavelet) of the raw signal model after adding noise (SNR=1 dB).

Nevertheless it is clear evident that the Morlet wavelet assures a more accurate time event resolution if compared to the Impulse one. This important feature assured by the Morlet wavelet is strongly required in order to localize the events within the entire engine cycle. It should be noted that although the transient events are spread in a wide scale range because of a low frequency resolution, this cannot be considered a drawbacks as the main purpose here is to identify and localize the transient within the engine cycle.

3.5.1.3 Experimental results

Pre-loaded rod

In order to carry out the cyclostationarity analysis, the time signal is synchronously resampled and the time synchronous average (TSA) is computed over two crankshaft rotations (Fig. 3.20 (a)). As indicated by Table 11, the comparison among healthy and faulty RMS and Peak values does not reveal the presence of any defect. As it happens both faulty RMS and Peak signal values are below the healthy ones. Nevertheless, the acceleration peaks of the synchronous average can be physically explained by inspecting the engine event diagram.

As shown by Fig. 3.20 (a) acceleration peaks are present on the pressurization of each cylinder. Moreover two acceleration peaks appear at 100 and 280 degrees respectively. Probably they could be due to the wide clearances between rod and crankshaft. These clearances are abruptly traversed whenever there is a change in the direction of the resultant force acting on the rod. As a matter of a fact, taking into account the analytical model developed in the Section 3.3 (see Fig. 3.7) it can be possible to observe that the resulting force acting on the rod changes its direction in two points (i.e. 1 and 2 in Fig. 3.7). They are located at 80 degrees before and after the TDC of the cylinder at the beginning of the intake stroke. This fact could be an indication that the two peaks in Fig. 3.20 (a) located about 100 degrees before and 80 degree after the TDC of the cylinder 3 at the beginning of the intake stroke (see ‘Comb 2’ in Fig. 3.20 (d)) could be due to the change in the direction of the resultant force acting on the rod.

However, it is evident that this type of analysis is inadequate to distinguish the presence and position of the fault from the events related to the pressurizations. For that reason, a second order analysis is performed.

Table 11 – RS3 engine: statistics extracted from TSA and MIP.

RS3 engine (Pre-loaded rod)				
	RMS		Peak	
	Normal	Faulty	Normal	Faulty
Vibration Time Synchronous Average [g]	0.17	0.14	1.20	0.71
Mean instantaneous power [g^2]	-	-	0.22	1.10

The mean instantaneous power (MIP) of the residual signal is evaluated and plotted in Fig. 3.20 (c), which also displays the faulty Peak value compared with the healthy one. As one can clearly see, the presence of the defect is confirmed by the differences in the MIP Peak values: the MIP Peak value is approximately five times the healthy one.

The residual signal depicted in Fig. 3.20 (b) shows the two events related to the faulty condition: the first one at 100 degrees is more clear than the second one at 280 degrees. The MIP (see Fig. 3.20 (c)) improves the localization of the two peaks.

At this stage, it can be concluded that the analysis of the mean instantaneous power makes know that the incorrectly tight rod is located in the cylinder 3.

In order to confirm these results, the WVD of the synchronous average and the residual signal are computed. Fig. 3.21 (a) and (b) plot the WVD's of the synchronous average and residual signal respectively.
The WVD of the synchronous average is of difficult interpretation. De facto vertical lines appear at the pressurization of each cylinder. Unfortunately, because of the acceleration amplitude associated to the engine events are about two times the back-ground noise (see Fig. 3.20 (a)), the vertical lines associated to the engine events are not clearly visible in the WVD, and in addition several cross-terms of relevant amplitude arise in the distribution. Therefore, the fault presence and its location cannot be established from Fig. 3.21 (a).

For that reason the WVD of the residual signal is computed (see Fig. 3.21 (b)). As previously said, the residual signal takes into account the 2nd order cyclostationary content of the signal, and so, by computing the WVD of this signal, one can obtain a distribution in which the energy content is mainly restricted at the fault location.

In fact, Fig. 3.21 (b) has only a vertical line in correspondence of the first change in direction of the resulting force acting on the piston rod of the cylinder 3.

The CWTs (Impulse mother wavelet is used) of both synchronous average and residual signal are also computed by using the traditional method (Fig. 3.22 (a) and (b)). It can be noted that the CWT of the time synchronous average is clearer than the WVD of the same signal. In particular the CWT map of the synchronous average (Fig. 3.22 (b)) detects the four cylinder pressurizations and the two events related to the fault condition. Even if a remarkable vertical line at 100 degree is present in the CWT map of the synchronous average (Fig. 3.20 (b)), it is not enough in order to assure the presence of a mechanical fault since its amplitude is comparable with the amplitudes of the pressurization peaks. Therefore, the CWT of the residual signal is an expected step for the mechanical fault localization. As depicted in Fig. 3.22 (b) the presence of the pre-loaded rod is highlighted by the marked vertical line at about 100°. Hence, as previously observed in WVD analysis, the fault location can be only achieved by the analysis of the residual signal. It is worth noting that the WVD of the residual signal, taking the advantages of the best time-frequency resolution everywhere, shows a better angular fault localization compared to the ones obtained by the CWT.

In order to improve the CWT of the TSA, the purification method is firstly carried out using the correlation weighted CWT coefficients, i.e. $C\hat{W}T$, as described in Chapter 2.

The correlation coefficient $\gamma(a,t)$ used in this method is able to select which coefficient gives the better matching between the frequency of the signal and the frequency corresponding to the Impulse wavelet scale. Fig. 3.23 shows that this method provides a clearer representation in terms of sensitivity to the background noise. However, the use of the coefficient correlation method does not improve the angular localization of the main engine events. This enhancement can be obtained using the Morlet mother wavelet that gives (see Fig. 3.24) a lower frequency resolution but a higher angular localization of the angle-frequency map. The Morlet mother wavelet has been used to compute the wavelet transform by means of both traditional and TDAS methods. The latter permits to obtain a better noise reduction and clearly reveals the event due to the faulty condition confirming what found for the tested signal model. Since the purpose of the proposed approach is to obtain a reliable faulty diagnostic through an accurate transient event localization, the Morlet wavelet can be considered as the most desirable if compared with the Impulse one. Fig. 3.25 and Fig. 3.26 illustrate the application of the TDAS method adopting linear and geometric averages respectively: no significant differences can be observed between the two time-frequency distributions.

Finally, the last proof of the mechanical fault presence can be obtained by the WVS of the residual signal. De facto, Fig. 3.27 shows only a vertical line at 100 degrees highlighting so the fault location. The WVS, joining the advantages of the best time-frequency resolution and the cyclic averaging power of the autocorrelation function is also able to point out other engine events happening within the entire engine cycle. This can be considered the best representation of the time-frequency response within an engine cycle.

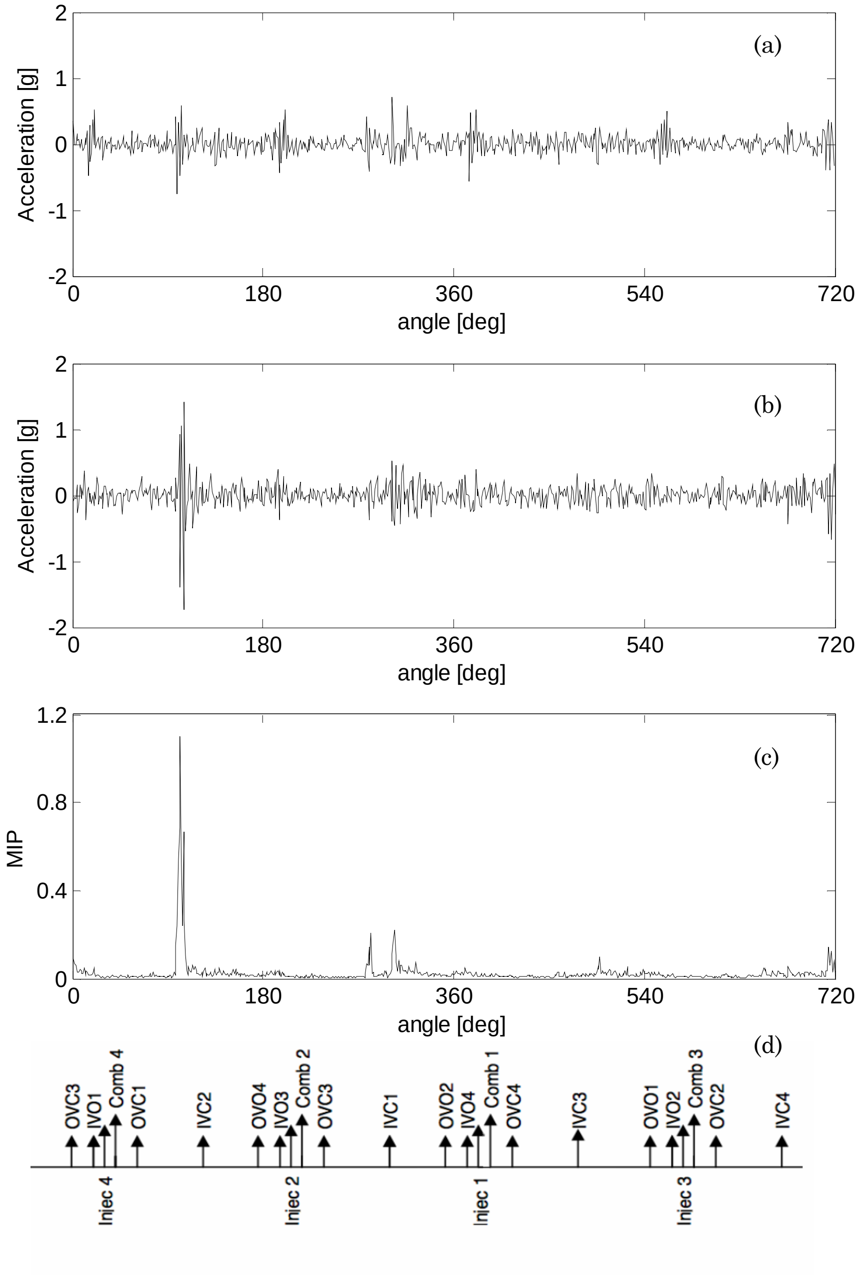

Fig. 3.20 – RS3 engine: (a) Time Synchronous Average, (b) residual signal, (c) Mean Instantaneous Power of the residual signal, (d) engine event diagram.

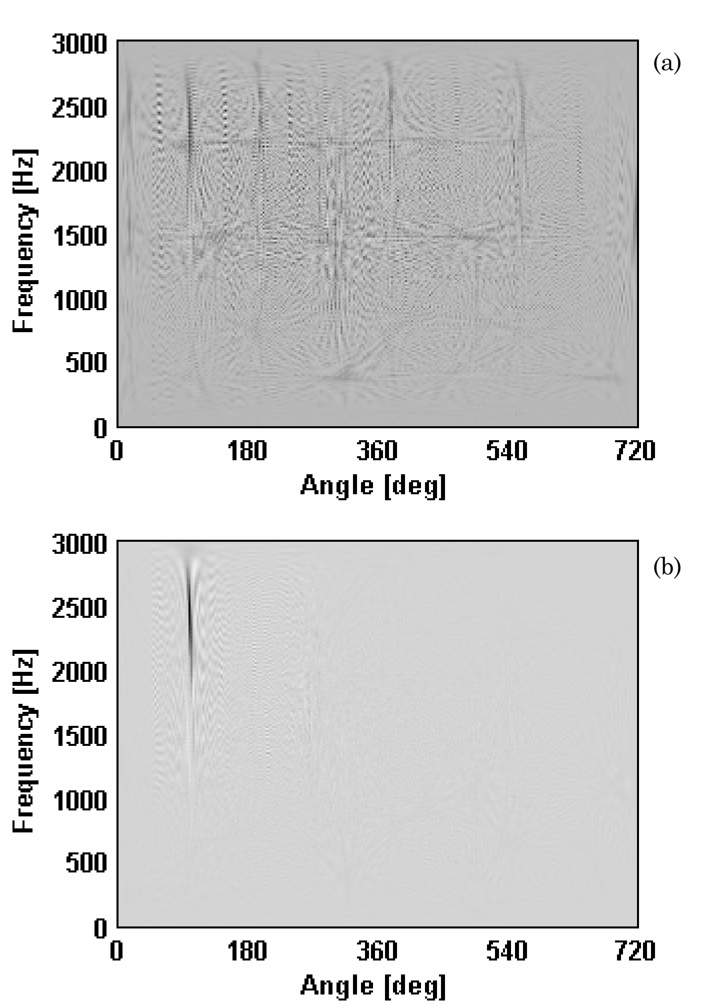

Fig. 3.21 – RS3 engine. WVD of the (a) TSA and (b) residual signal.

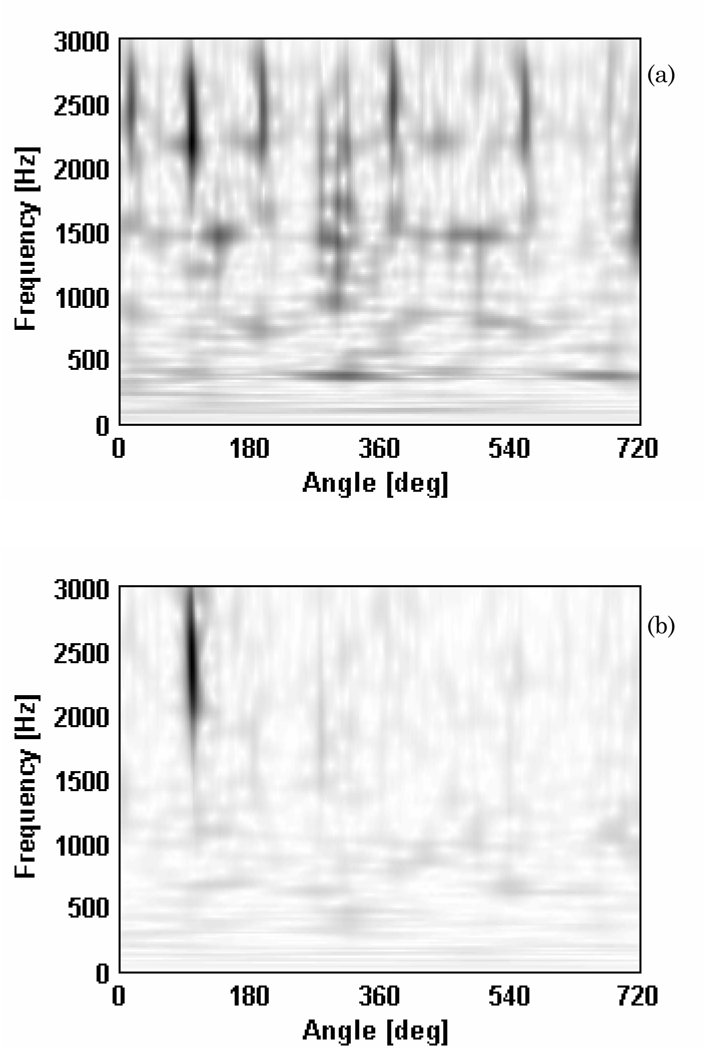

Fig. 3.22 – RS3 engine - CWT (traditional method - impulse mother wavelet) of the: (a) TSA and (b) residual signal.

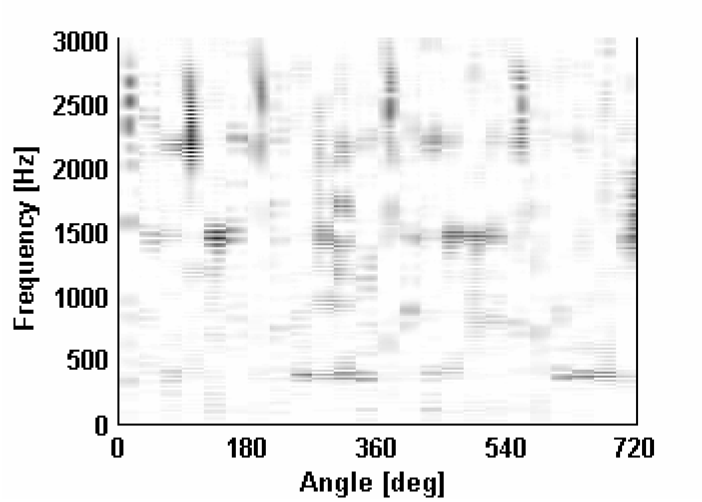

Fig. 3.23 – RS3 engine - CWT of the TSA: purification method (impulse mother wavelet).

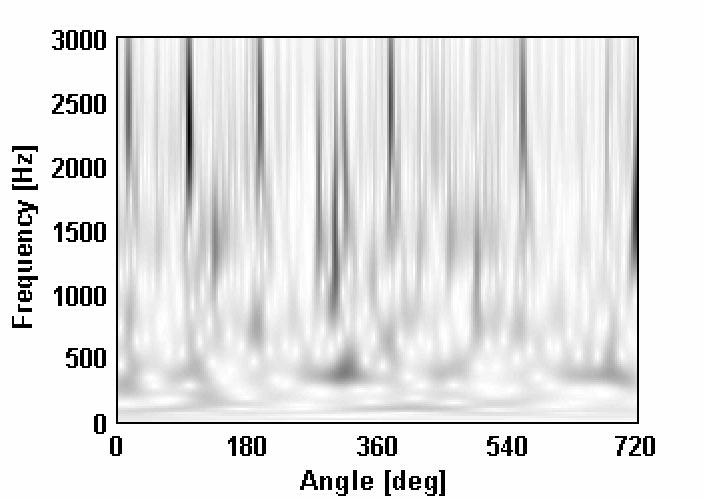

Fig. 3.24 – RS3 engine - CWT of the TSA: traditional method (morlet mother wavelet).

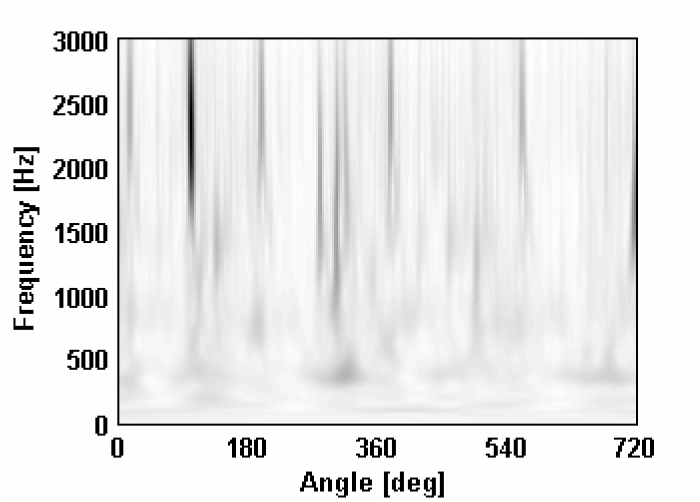

Fig. 3.25 – RS3 engine - TDAS using linear average (traditional method - morlet wavelet).

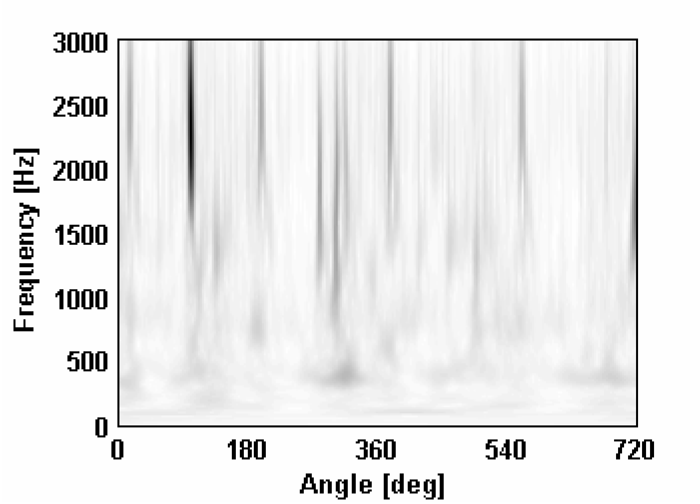

Fig. 3.26 – RS3 engine - TDAS using geometric average (traditional method - morlet wavelet).

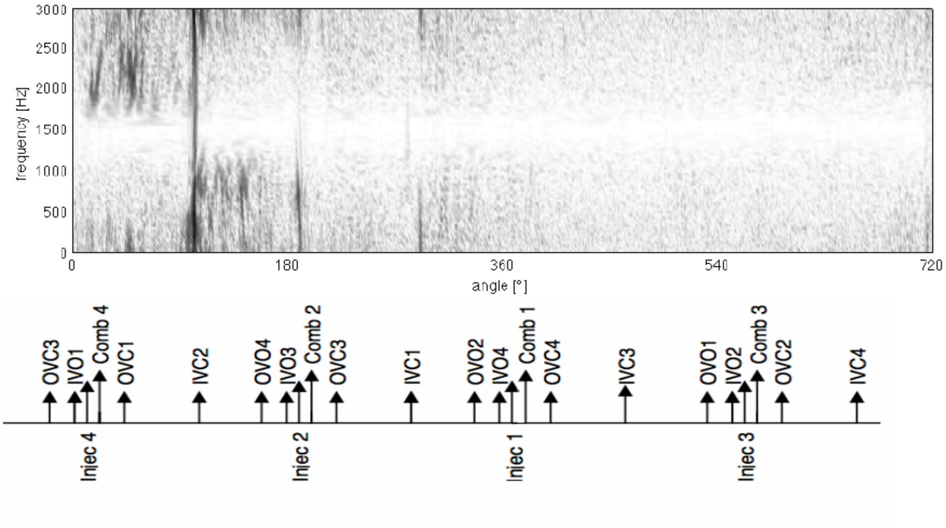

Fig. 3.27 – RS3 engine – WVS of the residual signal.

Rod without the bearing cap

Concerning the second fault condition, i.e. rod without bearing cap, all the same previous analyses are carried out: firstly the signal is synchronously resampled, secondly the residual signal and the mean instantaneous power have been calculated. The synchronous average is shown in Fig. 3.28 (a); Table 12 shows the comparison among RMS and Peak vibration values both in healthy and faulty conditions. This comparison highlights the presence of a defect: both RMS and Peak signal values are greater than in the healthy case.

In order to better understand this result, we associate the engine event diagram at the synchronous average depicted in Fig. 3.28 (a). By this comparison one can notice that four lower acceleration peaks are present on the pressurization of each cylinder.

In addition it can be noted a big variation in the synchronous average related to the hit of the piston rod of the cylinder 4 when the opening of the intake valves of the cylinder 4 happens at the beginning of the intake stroke.

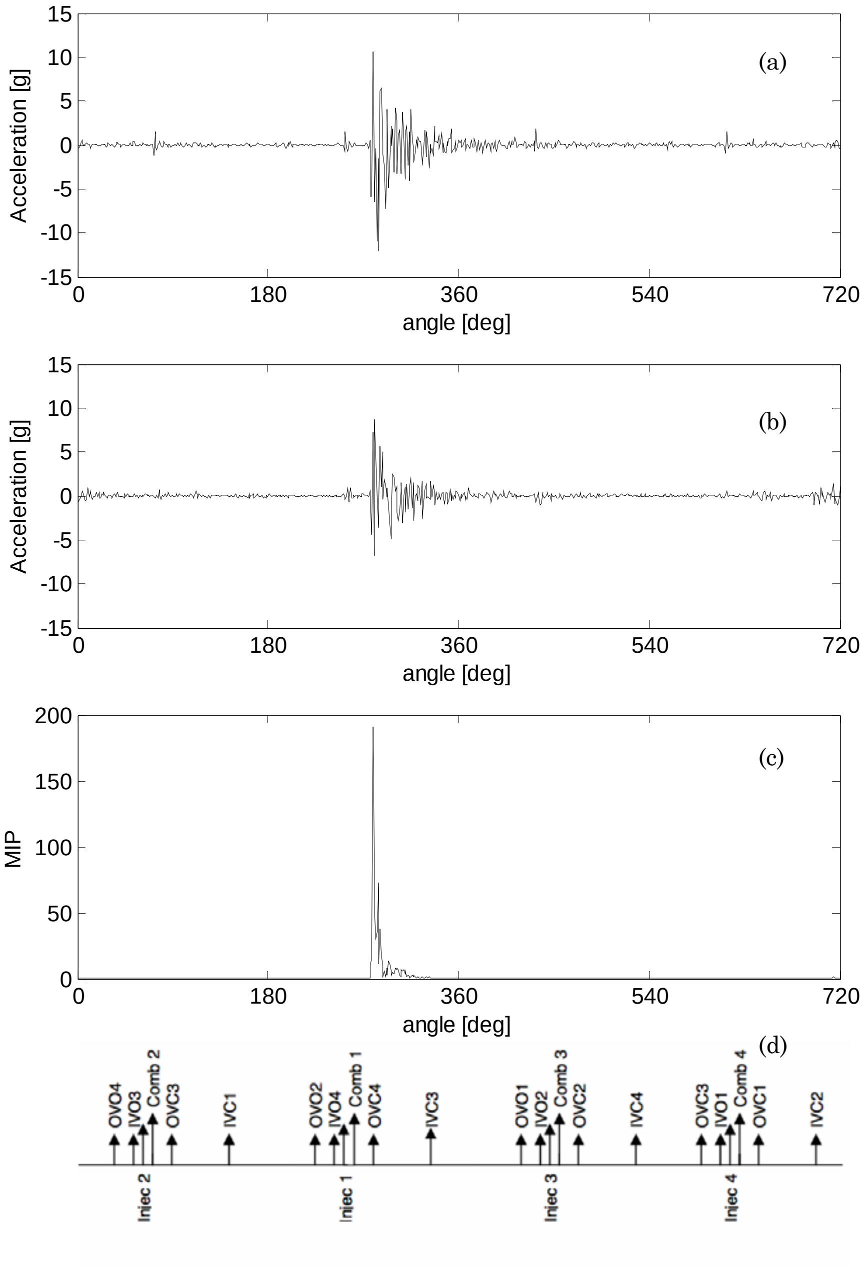

Fig. 3.28 – RC4 engine: (a) Time Synchronous Average, (b) residual signal, (c) Mean Instantaneous Power of the residual signal, (d) engine event diagram.

Table 12 – RC4 engine: statistics extracted from TSA and MIP

RC4 engine (Rod without bearing cap)				
	RMS		Peak	
	Normal	Faulty	Normal	Faulty
Vibration Time Synchronous Average [g]	0.17	1.13	1.20	10.61
Mean instantaneous power [g^2]	-	-	0.22	191.41

This fact, happening 26 degrees after the TDC of the cylinder 4, may be due to the impact of the piston against the intake valves that are being opened. This phenomenon, which is caused by the excessive backlash due to the absence of the bearing cap, occurs one time per engine cycle.

In order to get a better localization of the fault position, the mean instantaneous power of the residual signal has been computed. Fig. 3.28 (b) points out the presence of the fault at 26 degree after the TDC of the cylinder 4 at the beginning of the intake stroke confirming the results achieved by analyzing the time synchronous average.

Counter-rotating masses with a phase lag of 180 degrees

As previously mentioned this kind of fault concerns the incorrect mounting of the counterweight masses that permit the inertial force balance inside the engine block. In order to simulate this faulty condition two shafts running twice the crankshaft speed are mounted with two counter-rotating masses having a phase lag of 180 degrees. By means of such a wrong mounting the masses not only are unable to balance the inertia forces but they contribute to their increase.

Hence, the purpose here is not the localization of a single faulty event but the evaluation of how the faulty condition affects the engine block vibration response. The signals measured from the faulty engine are compared with the ones obtained from the unique healthy engine tested during the second investigation. From Fig. 3.29 (a) and Fig. 3.30 (a) it is clear that we are not able to understand some differences about the state of the engine only looking at the TSA of the signal. This clearly depicts the four peaks due to the pressurization of each cylinder for both healthy and faulty signals. What we may say is that the four pressurization peaks measured in faulty condition assume quite higher values than in the healthy one.

More significant information about the state of the engine can be revealed by the amplitude spectra of the TSA (Fig. 3.29 (b) and Fig. 3.30 (b)) that reveals that the faulty condition shows higher second order amplitudes. Also several harmonics still assume higher amplitudes.

This fact can be linked to the increase of the second order inertial force due to the incorrect mounting of the masses. As it is well known this force is not correctly balanced in a four-cylinder Diesel engine and the incorrect phase lag of the masses causes the increase of its amplitudes. It can be concluded that the TSA spectra can be taken into account in the analysis procedure in order to monitor the amplitude trend of the characteristic vibration frequencies in a four-cylinder engine (2 order = firing frequency, 1/2 order = engine cycle, 1 order = crankshaft speed).

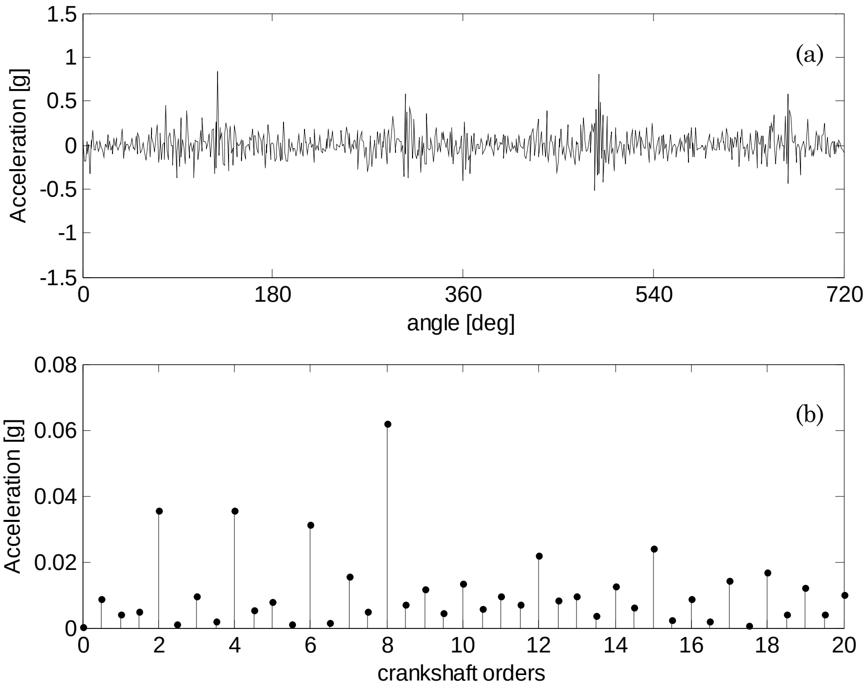

Fig. 3.29 – CRM engine: (a) Time Synchronous Average, (b) FFT of the TSA.

In this case the second order frequency component can be related with the periodicity of the second order inertial force term that is not balanced here.

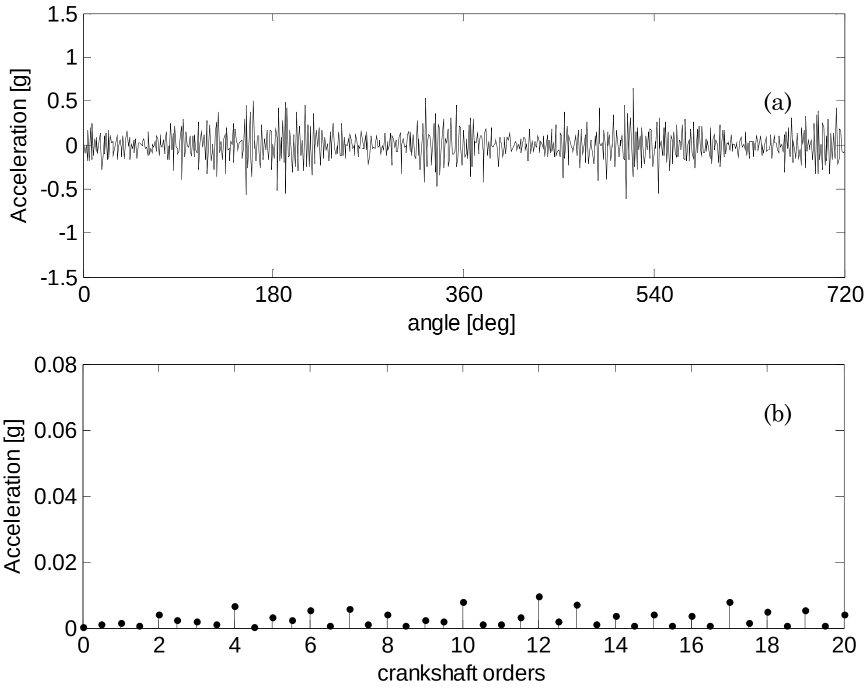

Fig. 3.30 – Healthy engine: (a) Time Synchronous Average, (b) FFT of the TSA.

3.6 Instantaneous Angular Speed (IAS) analysis

Instantaneous Angular Speed (IAS) of a diesel engine could supply useful information about faults affecting the gas pressure and the crankshaft motion. As a matter of a fact the IAS fluctuations of a diesel engine are closely related to the fluctuations of the total power acting on the crankshaft. As it is well known, the total power is then obviously affected by the gas pressure in the cylinder, inertial forces, friction forces and engine load. Since we are examining data measured from engines in non-combustion state, the goal is to use the IAS signal as an useful tool to detect faults related to the pressurization of the cylinders (i.e. when both exhaust and intake valves are closed) and hits affecting the crankshaft.

The two faults under study are the rod not correctly pre-loaded and the one without bearing cup. It is expected that they could affect the pressurization since the piston linked to the faulty rod gives a more longer stroke than in healthy condition. Moreover several hits of the faulty rod against the crankpin can affect the crankshaft motion and, therefore, the crankshaft angular speed.

3.6.1. Data pre-processing

The IAS signal has been obtained by means of the method outlined in Chapter 2 processing an encoder signal giving 1024 pulse/rev. The encoder is mounted between the coupling unit and the clasp connected to the flywheel. During the acquisitions the IAS signal is synchronised and resampled in the angular domain obtaining 1024 angular points each revolutions. This was done in order to compute the TSA of the IAS signal over 83 angular histories, each corresponding to two crankshaft rotations (720°), in order to respect the periodicity of the 4-stroke engine.

Fig. 3.31 depicts the 83 synchronised angular histories having the same starting phase. The average angular speed of the engine during the acquisitions was set at 1000 rpm.

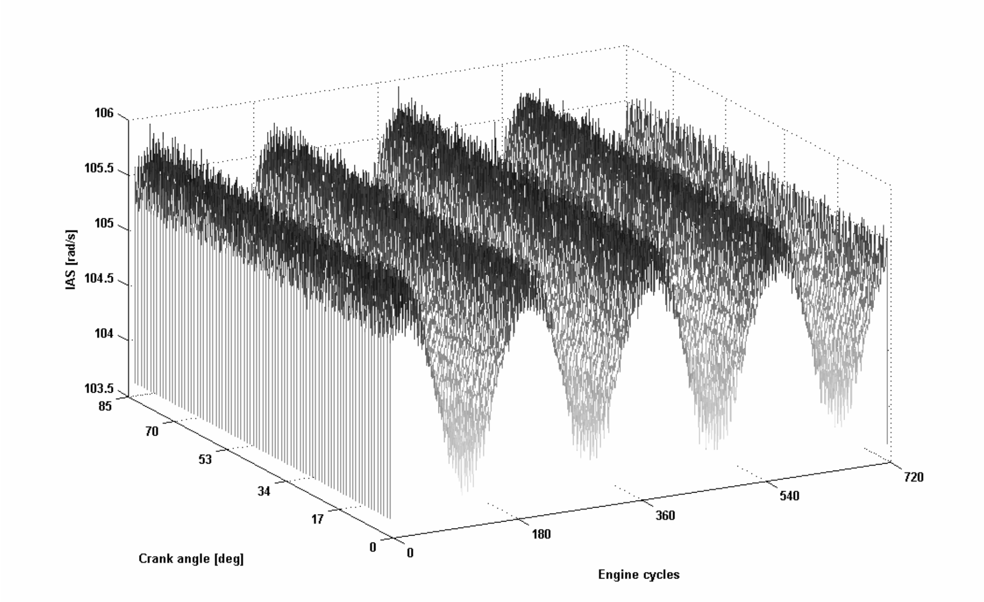

Fig. 3.31 – Waterfall of synchronous IAS acquisitions in two crankshaft revolutions.

Since the TDC reference is not available here the phase is different for all three engine tested (healthy, pre-loaded rod and rod without bearing cap). Therefore, we are only able to identify the presence of the fault and not to point out its angular localization inspecting the engine event diagram.

3.6.2. Experimental results

Fig. 3.32 depicts the TSA of IAS for all three engine analyzed. It can be noted that the IAS signal can be regarded as a first-cyclostationary process since the TSA clearly shows a strong periodic behaviour. In fact the TSA varies from a minimum at the beginning of the expansion stroke to a maximum near the middle of the same stroke confirming what found by Yang [33]. Since the engines are tested at lower speeds and the pressurization in each cylinder mainly contributes to the total power torque, only a peak value of IAS is present for each expansion stroke. In the faulty condition pressure variations affecting the combustion chamber of the one cylinder should mean a change in the pattern of IAS. Moreover if a pressure variation happens due to the fault in one cylinder, the other cylinders produce a greater power than in the normal condition in order to maintain the balance of engine power and the speed.

Nevertheless no important differences among the faulty and healthy condition tested can be shown by Fig. 3.32. Therefore it can be concluded that the IAS signal is not effective to point out hits or cylinder pressure variation caused by the two faulty analyzed.

For this reason the torsional vibration signal can be derived after differentiation of the IAS signal.

The TSA of the torsional vibration signal is obtained differentiating each phased angular history over two revolutions and then computing the average over 83 crankshaft revolutions as done for the IAS signal. In this case the periodic behavior of the vibration signal is less evident since it is buried in the noise (see Fig. 3.33 (a)). However, the residual signal (Fig. 3.33 (b)) is found predominant: this means that relevant random fluctuations of the torsional vibration exist from cycles to cycles.

By the analysis of the residual signal for all the three engines tested (Fig. 3.33, Fig. 3.34 and Fig. 3.35 (b)) no clear differences can be observed in order to detect the presence of the fault.

The next step is to calculate the (Mean Instantaneous Power) MIP of the residual signal squaring the signal itself. The MIP calculation put in evidence the periodicity of the residual signal making clear the second order cyclostationary nature of the torsional vibration signal.

Observing the MIP values for all three engines (Fig. 3.33, Fig. 3.34 and Fig. 3.35 (c)), it can be noted that the MIP obtained in the healthy condition (Fig. 3.33 (c)) shows a quite uniform trend within an engine cycle. On the other hand the MIP calculated in faulty conditions (Fig. Fig. 3.34 and Fig. 3.35 (c)) show a more irregular behavior that could mean higher fluctuations around the deterministic value due to the presence of the fault. Moreover higher MIP amplitudes can be obtained for both faulty conditions. At this stage it is only possible to assure that the MIP trend changes from the normal to the healthy condition and not to associate the origin of the irregularities to particular events due to the faulty condition.

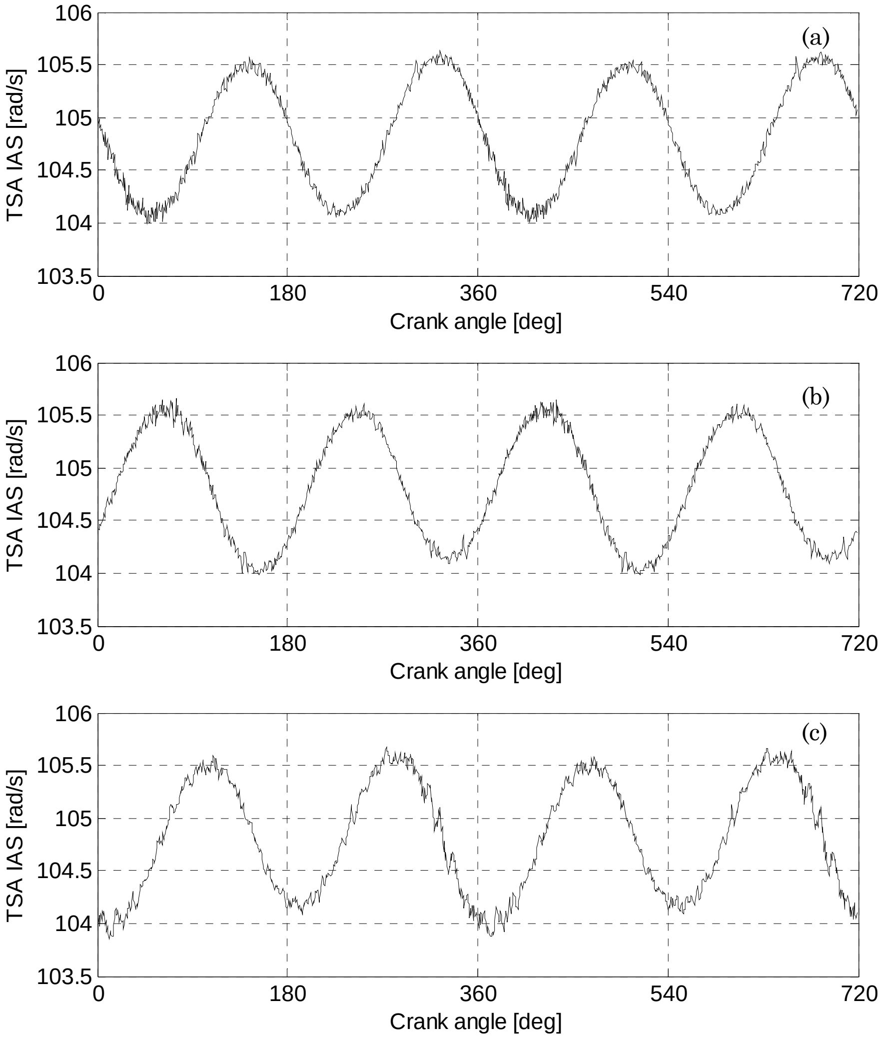

Fig. 3.32 – TSA of IAS: (a) Healthy engine; (b) RS3 engine; (c) RS4 engine.

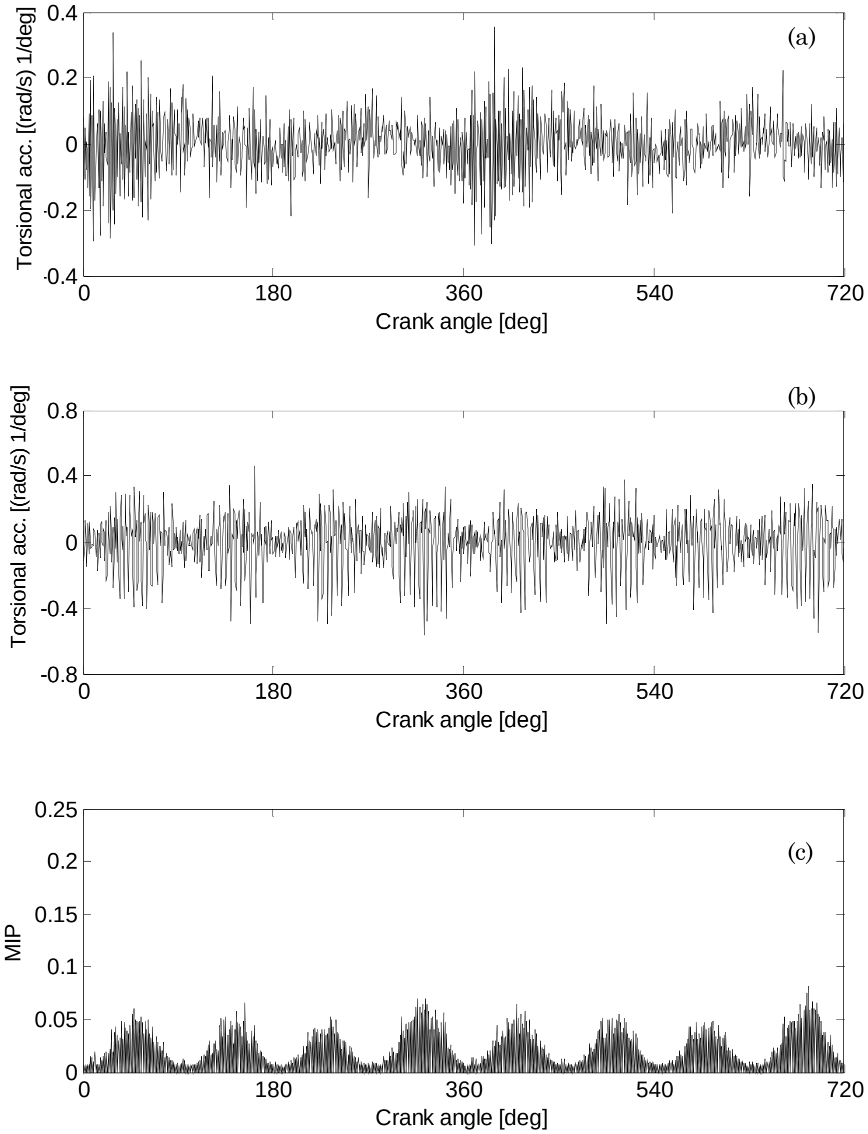

Fig. 3.33 – Healthy engine: (a) torsional TSA acceleration after differentiation of IAS trend depicted in Fig. 3.32 (a); (b) residual torsional acceleration; (c) MIP of the residual torsional acceleration.

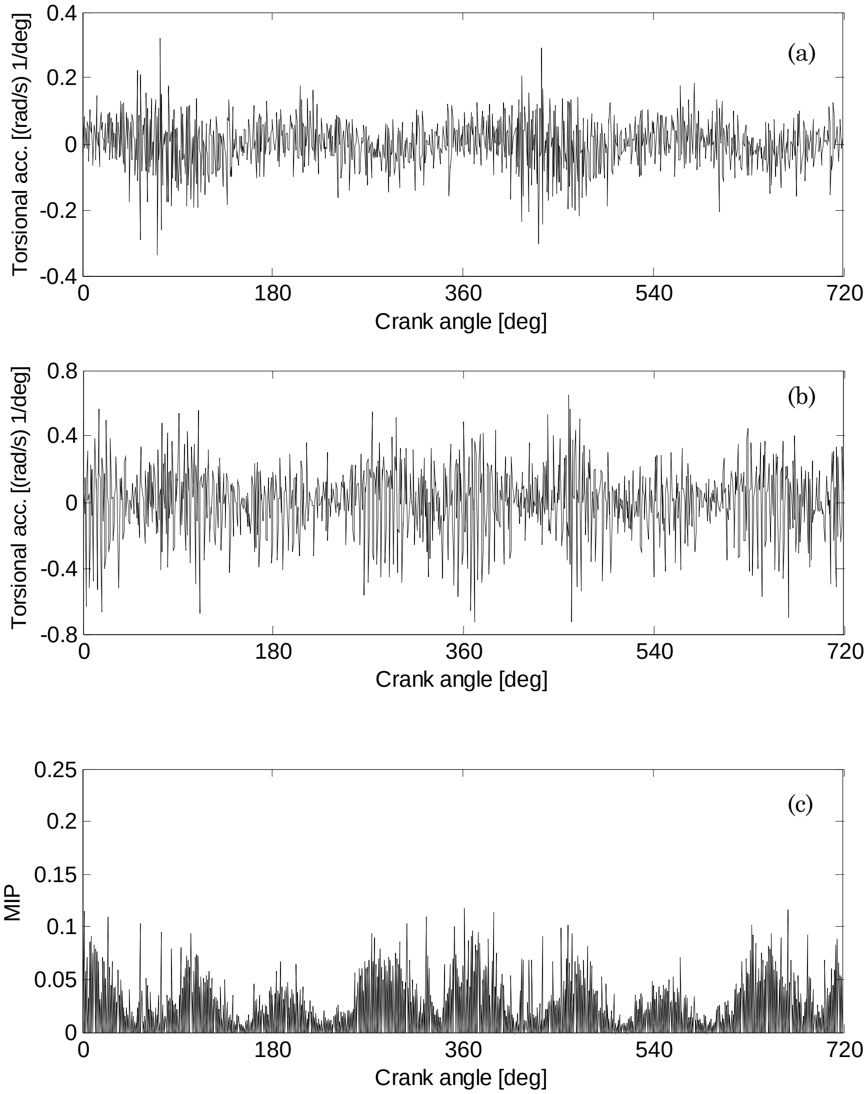

Fig. 3.34 – RS3 engine: (a) torsional TSA acceleration after differentiation of IAS trend depicted in Fig. 3.32 (b); (b) residual torsional acceleration; (c) MIP of the residual torsional acceleration.

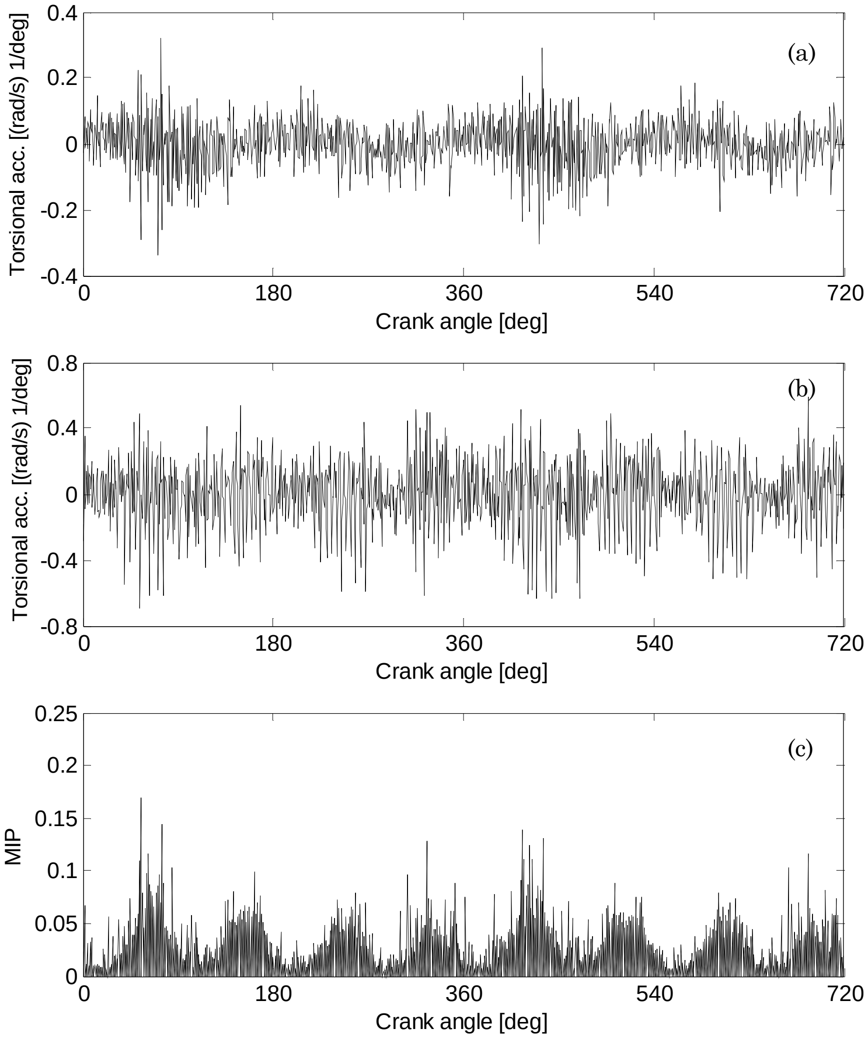

Fig. 3.35 – RC4 engine(a) torsional TSA acceleration after differentiation of IAS trend depicted in Fig. 3.32 (c); (b) residual torsional acceleration; (c) MIP of the residual torsional acceleration.

Interestly it can be concluded that the deterministic/random torsional vibration signal decomposition can be used to evaluate the presence of the tested faults. The torsional vibration obtained by means of the IAS signal differentiation has found to be more effective than the IAS signal itself in detecting irregularities due to the both faults tested.

Chapter 4

CONDITION MONITORING OF THE THRESHING PROCESS IN HARVESTING MACHINES

4.1 Introduction

The condition monitoring procedure adopted in the case of the threshing process condition monitoring can be divided into three steps: measurement of the physical quantity (acceleration and sound pressure), processing of the collected data in order to extract proper features and successive evaluation of the feature values calculated for different harvesting machine settings.

The description of the mechanical parts involved in the threshing process, which form the so-called threshing unit, is developed in Section 4.2. The experimental apparatus and some data pre-processing tools are described in Section 4.3 and 4.4 respectively.

A preliminary frequency analysis of the accelerometer signals measured on the threshing unit is needed to understand which point that shows the best vibration response in terms of acceleration amplitudes and which vibration response is better correlated with the different vibration sources due to the threshing process. The achievements obtained by means of the preliminary frequency analysis are shown in Section 4.5. The application of the time domain monitoring procedure by means of the feature extraction is outlined in Section 4.6.

Section 4.7 shows the use of the Discrete Wavelet Transform (DWT) to extract the frequency band mostly characterised by impulsive components. Finally, Section 4.8 describes some outlines obtained through the vibro-acoustic analysis performed in the angular domain.

4.2 The threshing process: description of the mechanical parts

The threshing unit of a non conventional harvesting machine performs the following operations:

- threshing and separation: the harvesting machine, after cutting the crop, makes the kernels free from chaff and straw;
- cleaning process of the crop in order to separate the kernels from other small particles like chaff and short straw.

The mechanical parts involved in the threshing process are illustrated in Fig. 4.1.

The first operations are performed by two counter-rotating rotors that allow an helicoidally flux of the crop. Spirally rasp bars and friction elements mounted on the rotors favour the friction of the crop against the concaves.

There are four concaves, two for each rotor, two mounted close to the threshing zone and two close to the separation zone.

It is easy to distinguish two different zones (see Fig. 4.2) along the whole rotor path:

- the threshing zone;
- the separation zone.

The size of the concaves, the number as well as the size of the rasp bars change as they go from the threshing zone to the separation zone.

Most of the crop that leaves the straw is obtained in the threshing zone in which the concave shows the highest vibration. During the separation process the rotor tries to thresh the crop kernels that are still attached to the straw.

When the crop has already been threshed, it is cleaned under the rotors.

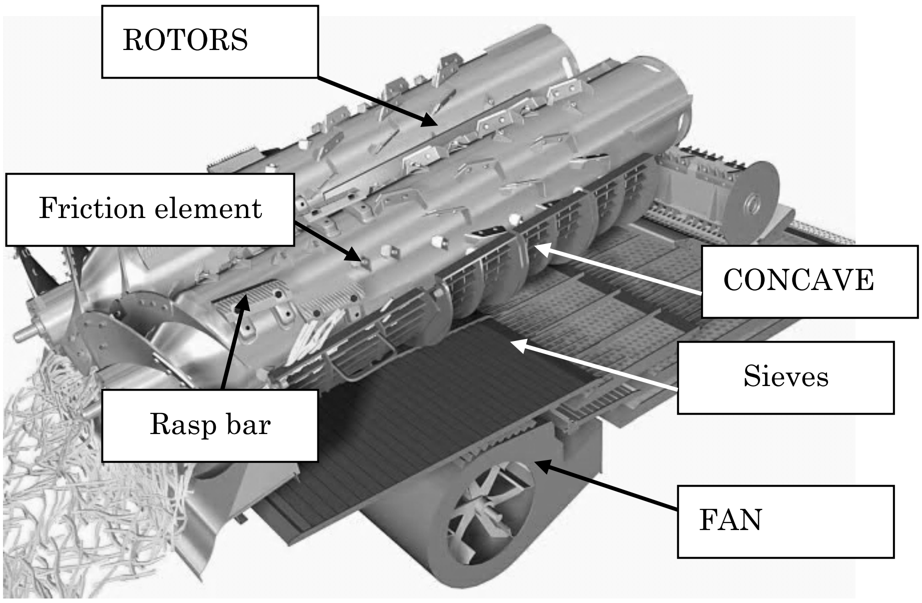

Fig. 4.1 – Threshing unit: mechanical parts involved in the threshing process.

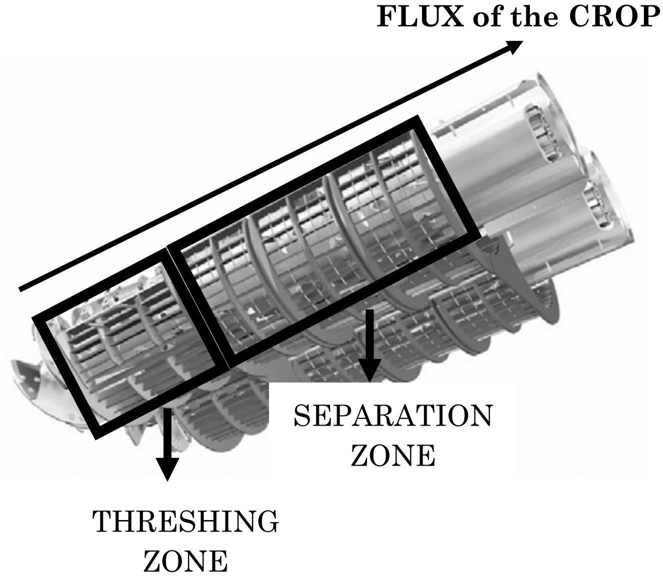

Fig. 4.2 – Harvesting unit: threshing and separation zones.

As shown in Fig. 4.1, the cleaning operations are carried out by means of 3 different sieves, upper, middle and lower, that, running alternatively, keep the material out from the crop (chaff and short straw). The air produced by the fan blows away this material.

4.3 Experimental apparatus and tests conditions

As mentioned above, the first step in the condition monitoring process is to measure the physical quantity of interest.

Piezoelectric accelerometers and condenser microphones have been used for all the tests in **stationary** (i.e. indoor laboratory test rig) and **field** conditions (i.e. outdoor during field operations).

The main part of the results shown in the next Sections have been achieved by means of **stationary** tests. These tests have been carried out using a conveyor belt that brings the crop towards the feeder. The feeder helps the crop enter in the threshing unit.

Both indoor and outdoor setup have been built in order to test the machine under different setting conditions by varying capacity (i.e. total crop entering the machine), concave distance (i.e. radial distance between the concave and the rotor), rotor speed, grain to straw ratio (i.e. length of the plant) and degree of moisture. A higher variety of machine settings can be tested in stationary conditions.

Both test rigs are designed taking some important constraints into account:

- measure signals from points located in both threshing and separation zones in order to understand if differences in excitation occur between these two zones;
- measure the vibration signal from the machine frame in order to understand which is the contribution of the machine vibration to the total vibration measured on the concaves;
- measure the vibration of the concave in order to understand how the crop distribution affects the concave vibration;
- mounting transducers in points where the transmission path is less intricate;

- verify the effectiveness of the microphone signals acquired from both threshing and separation zones in explaining the crop distribution between the rotor and the concave; verify if the microphone mounted outside the cabin can simulate the user ear in linking the threshing performances with the sound perceived.

In the **stationary and field tests** the vibration signals have been measured in 6 positions (see Fig. 4.4) by means of piezoelectric accelerometers (frequency range: 1-10000 Hz):

- Threshing zone: concave front, middle, rear positions (triaxial accelerometers; see Fig. 4.7);
- Frame supporting the concave (triaxial accelerometer);
- Rotorplate front (monoaxial accelerometer); Rotorplate rear (monoaxial accelerometer).

The sound pressure signals have been acquired by means of 3 condenser microphones mounted in the following positions:

- Threshing zone (see Fig. 4.4);
- Separation zone (see Fig. 4.4);
- Outside the cabin (see Fig. 4.5).

In the **stationary tests** the National Instrument PXI has been used for acquiring both accelerometers and microphone signals at sampling frequency of 6 kHz. In the same tests, the microphone signals have been also acquired with the LMS Pimento system at higher sampling frequency of 20 kHz.

In the **field tests** the microphone signals have been acquired with a sampling frequency of 8 kHz.

Two experimental investigations in **stationary conditions** have been carried out: a tachometer signal has only been measured in the 2nd investigation. This signal generates 1 pulse for each revolution of the rotor, acquired at sampling frequency of 6kHz.

NI Lab-view software has been used to visualise the data during the tests. The output data have been processed by means of Matlab software.

As shown in Fig. 4.3, a run of the stationary tests is typically made up of various parts. A first part where the machine runs empty (1), a second part where the amount of crop in process increases (2), a third

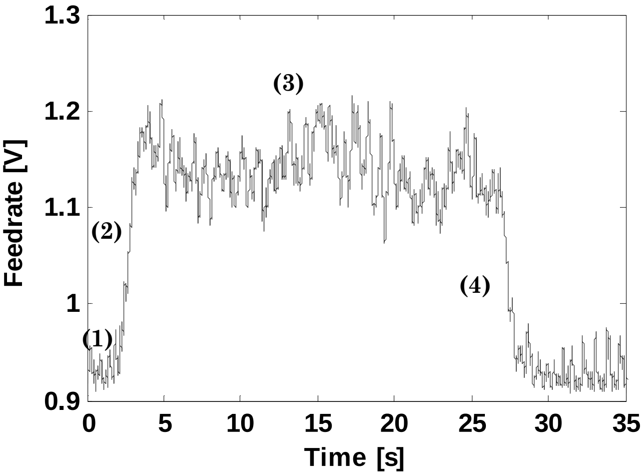

Fig. 4.3 – Feedrate signal measuring the amount of crop processed: processing phases.

part where the crop is processed (3) and a final part where the amount of crop decreases (4).

The third part is obviously the main subject of investigation. In order to extract the time histories related to this part, the feedrate signal is taken as a measurement of the amount of crop processed. The feedrate signal (see Fig. 4.3) measures the feeder belt tension during the loading operations.

4.4 Data pre-processing

Some pre-processing operations were needed in order to treat the signals in time and frequency domain before the analysis.

4.4.1. Fixed and adaptive multiband digital filtering

Digital filtering has been used to focus the analyses in zoomed frequency bands. This has been made using IIR filters like band pass and high/low pass digital filers.

In order to filter the signal in characteristic frequency bands an adaptive multiband filter has been designed tracking the rotor speed.

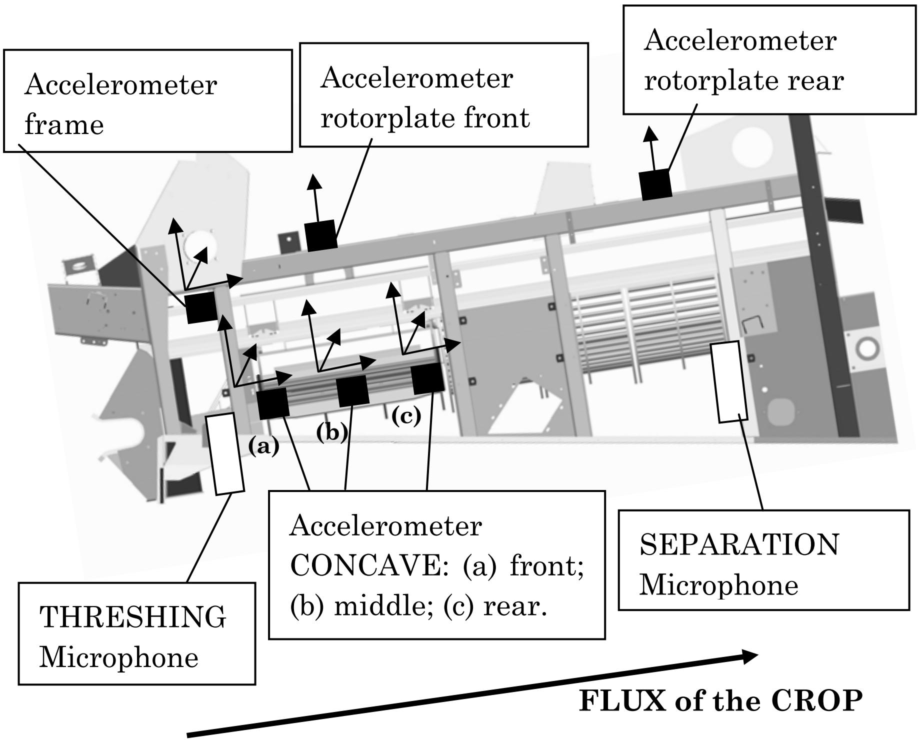

Fig. 4.4 – Test setup: accelerometers and microphones mounted INSIDE the machine.

During the first investigation, the speed information has been extracted through the "Rpm extraction" workbench available in LMS Test.Lab tracking the ninth order of the rotor speed extracted from the vibration signal. It will be proved that this frequency component is resulted the most relevant for all the runs. It is worth noting that the application of a multiband filter is equivalent to calculate the Time Synchronous Average (TSA) of the vibration signal. More details concerning the implementation of this method are reassumed in [101].

Fig. 4.5 – Test setup: microphone mounted OUTSIDE the machine, over the cabin.

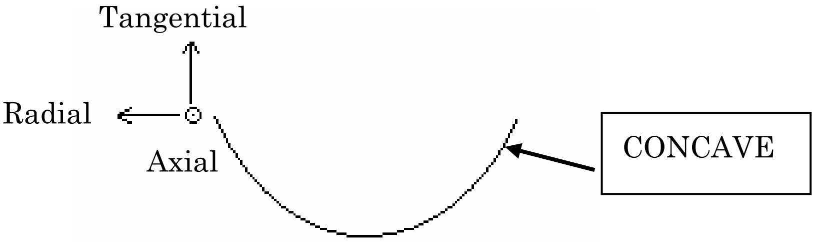

Fig. 4.6 – Test setup: triaxial concave accelerometers directions.

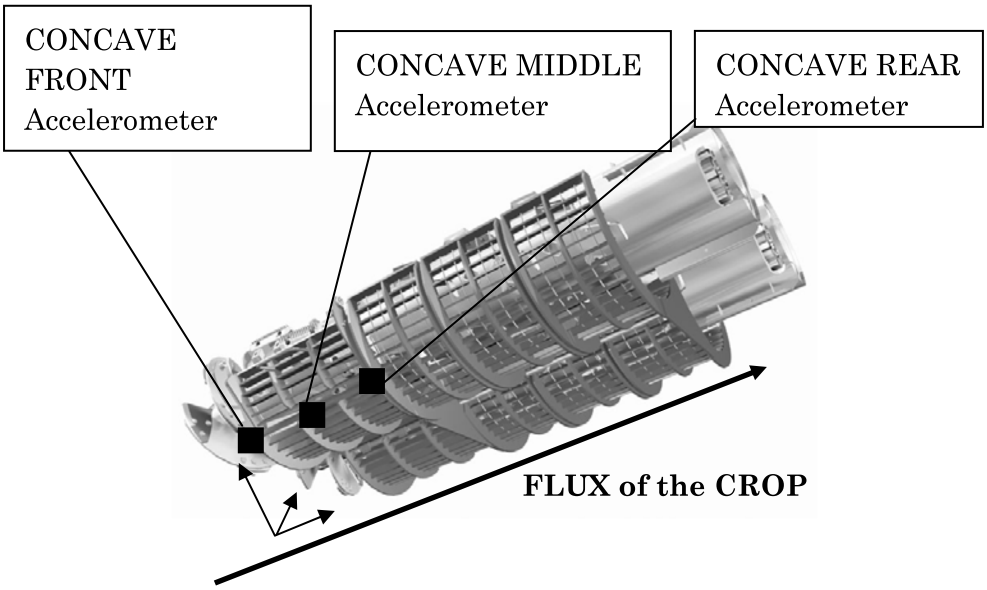

Fig. 4.7 – Threshing zone -Test setup: focus on the CONCAVE accelerometers: front, middle and rear positions.

Fig. 4.9 compares the PSD of the raw and adaptive multiband filtered signals in five different bands showing the 3X characteristic frequency and its four harmonics. It can be noted that the peaks of the frequencies of the filtered signal match exactly the ones obtained from the raw signal. This means that the tracking of the speed is correctly performed. The differences in amplitudes are given by the high gain used for the filter application in order to highlight the characteristic frequency and its four harmonics. In the next Sections it will be verified that the 3X characteristic frequency is due to the interactions among the rasp bars (mounted on the rotor) and the concave.

4.4.2. Weighting

The A-weighting has been applied to the raw sound pressure signals in order to reproduce the ear sensitivity to different frequencies.

As it is known the human ear is more sensitive to high frequencies than lower frequencies. The weight A filter considers this fact

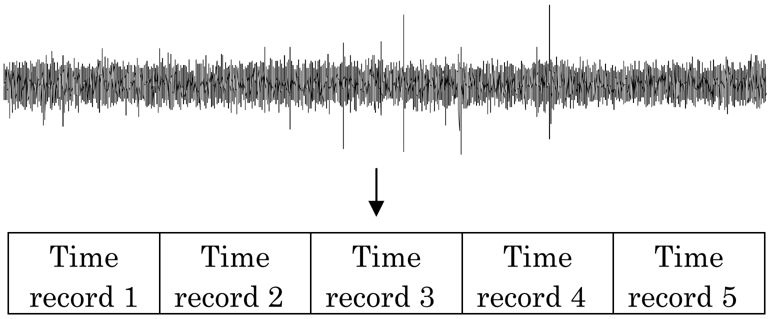

Fig. 4.8 – Segmentation analysis.

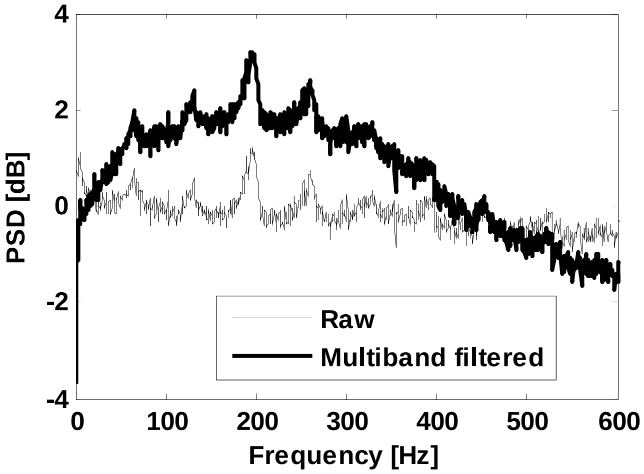

Fig. 4.9 – PSD of the raw and multiband filtered concave middle radial vibration signal.

emphasizing the frequency amplitudes between 1 kHz and 5 kHz and doing a reduction in the range lower than 1 kHz.

4.4.3. Fixed and adaptive segmentation

Segmentation of a time domain signal (see Fig. 4.8) can be performed in two ways: fixed segmentation and adaptive segmentation.

A fixed segmentation scheme divides the signals in time record having the same duration.

An important consideration in the fixed segmentation process is the selection of the segment length which should have to reflect the statistical properties of the entire signal.

In adaptive segmentation, the time record length can be decided in order to have the same number of segments for signals of different durations. Only the first approach has been used in this work.

4.5 Characteristics of the vibration signature: frequency analysis

This Section shows the results of the preliminary frequency analysis carried out for vibro-acoustic signals in load conditions. The frequency analysis has been performed by calculating the PSD in peak format [g^2/Hz] without overlap and with Hanning window.

The sampling frequency is 6 kHz for both accelerometer and microphone signals so the analysis bandwidth is 3 kHz. The frequency resolution is set 0.5 Hz for all PSD's calculations.

The goals of this preliminary analysis are the following:

- Understanding which is the concave accelerometer direction that shows the best response in terms of amplitudes in the frequency domain;
- Understanding which is the transducer that measures the signal most correlated with the vibration sources due to the threshing operations;
- Understanding if the signals are sensitive to the changes in amount of crop processed between the threshing zone and the separation zone;
- Identifying characteristic frequencies in the spectra and the causes of their presence;
- Understanding which part of the raw vibration measured on the concave is due to the crop excitations and which is due to the supporting frame vibration;

- Correlating the frequency signatures with the operational parameters: capacity, concave distance, rotor speed, degree of moisture and grain to straw ratio.

4.5.1. Concave and frame accelerometer signals

The frequency analysis was firstly carried out for signals measured by the three concave middle accelerometers in the radial direction. This direction was expected to be the most excited by the threshing flow. In principle a comparison among three radial signals measured with the maximum excitation condition was performed. This condition was expected to be obtained by the following machine settings:

- high capacity;
- low concave distance;
- high rotor speed.

The run that satisfies this kind of setting is the Run 27 presenting the setting parameters listed in Table 13.

By the PSD's depicted in Fig. 4.10, it can be seen that the radial signal measured in the concave middle position shows in the first 600 Hz a characteristic relevant frequency content in the first 600 Hz where it is possible to observe equispaced frequencies.

Concerning the amplitudes, the middle signal presents higher values than the other signals coming from the front and rear concave accelerometers due to the fact that they are mounted close to the bolt joints that connect the concave to the frame.

In order to verify the repeatability of this frequency behaviour, further comparisons among runs with different setting parameters have been evaluated.

The Runs 54, 36 and 12, presenting the setting parameters listed in Table 13 have been considered.

Observing the PSD trends shown by the Run 54, 36 and 12 for the radial direction in all three positions (see Fig. 4.11, Fig. 4.11 and Fig. 4.12) it can be noted that the concave middle radial direction is the most excited. As a matter of a fact all the positions show equispaced frequencies in the first 600 Hz. However the middle position still continue to show the highest amplitudes for all three directions. The change in quantity of the crop between the front concave position (start of the threshing zone) and the rear one (end of the threshing zone and start of the separation one) does not affect the frequency behaviour that seems to be the same in the first 600 Hz for all positions. In particular the amplitudes are strongly dependent by the transducer location.

As a second step we want investigate how the different setting parameters influence the vibration amplitudes. Concerning the frequency amplitudes, it is already possible to recognize some differences due to the different setting parameters. As an example, since it presents high concave distance, Run 36 shows lower PSD amplitudes than the Runs 27 and 54. Moreover the resonance zone highlighted by the rear signals at Runs 54 and 12 is not excited at Run 36.

In order to evaluate the presence of relevant characteristic frequencies components only the Run 27 has been taken into account considering the accelerometer mounted on the middle concave position. As the first analyses have highlighted, the concave middle radial signal shows the best response in terms of frequency amplitude values.

Moreover, the Run 27, presenting the highest excitation due to its setting parameters, is well suited to evaluate the presence of characteristic frequencies.

Table 13 – Stationary tests: setting parameters of four runs.

Operational parameters		Run			
		27	**54**	**36**	**12**
Concave distance	[mm]	5	13	35	13
Rotor speed	[rpm]	1350	1350	1350	945
Capacity	[ton/h]	91.1	110	102	82

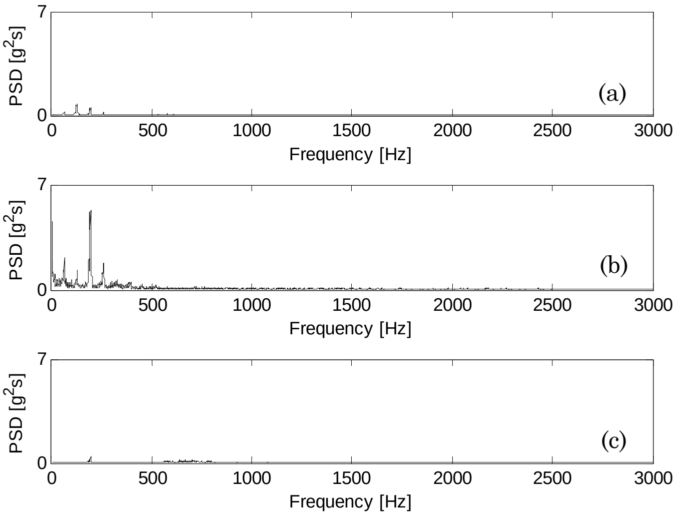

Fig. 4.10 – Run 27 - PSD of the vibration signal - Radial direction - Positions: (a) concave front, (b) concave middle, (c) concave rear.

Fig. 4.14, plotting the PSD (ref. 1 g^2/Hz) of the concave middle radial signal, clearly shows the existence of one characteristic frequency and its several harmonics. It is proved that this relevant characteristic frequency is due to the periodical rasp bar interactions with the concave.

Since their helicoidally placement along the rotor, one rasp bars interact with the concave three times for each rotor revolution. Due to this fact let's call the characteristic frequency as F_{bar} that can be expressed as follows:

$$F_{bar} = \frac{3 \cdot n_{rotor}}{60} \tag{4.1}$$

where n_{rotor} is the nominal rotor speed in rpm. Concerning the Run 27, it presents $n_{rotor} = 1350$ rpm and, consequently, $F_{bar} = 67.5$ Hz.

The cursor in Fig. 4.14 indicates a smaller value of 64.5 Hz, due to the intrinsic speed rotor irregularities. Hence, the F_{bar} and its 7 harmonics are clearly visible in Fig. 4.14. The peak closest to the zero frequency is verified to be not influenced by the setting parameters, so it has not considered relevant for the analysis.

Fig. 4.15 depicting the PSD of the front, middle and rear concave accelerometer signals in the radial direction show the same frequency behaviour in the first 600 Hz for all three positions. Moreover it can be noted that the front direction shows several damped resonances in the bands 600-3000 Hz. Focusing on the range 0-600 Hz (see Fig. 4.16) the front and rear accelerometer show lower amplitudes than the middle one in the radial direction. Moreover, the PSD of the axial, tangential and radial concave middle signals (see Fig. 4.17) show that the radial direction is the most excited in the range 0-600 Hz. On the contrary, the axial direction seems to be the less excited as expected. All three signals show the presence of F_{bar} and its seven harmonics.

From Fig. 4.18 and Fig. 4.19, it is observed that the tangential direction shows the same frequency behavior of the radial signal for each concave position: F_{bar} and its harmonics can be recognized in the first 600 Hz and a flat spectrum elsewhere. However, it can be noted that the F_{bar} harmonics are less pronounced in the PSD of the tangential signal compared to the radial one.

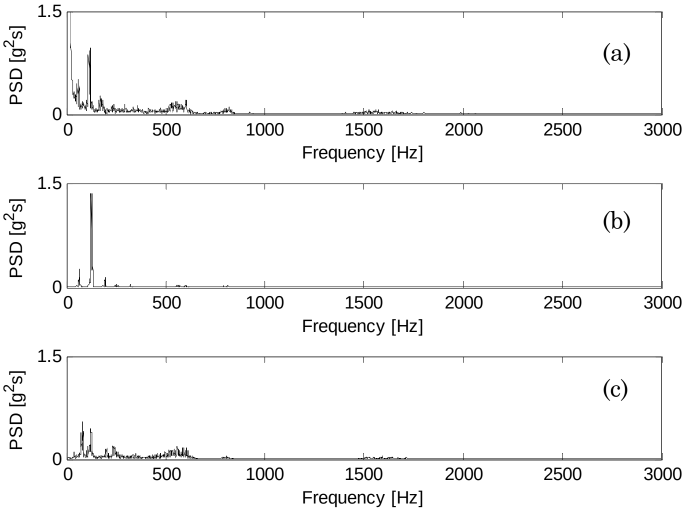

Fig. 4.11 – Position: concave front - PSD of the vibration signal - Radial direction - Runs: (a) 54, (b) 36, (c) 12.

Finally, Fig. 4.20, depicting the PSD of the frame accelerometer radial signal, shows that it is not possible to recognize the characteristic frequency and harmonics in the range 0-600Hz. The frame signal presents an irrelevant frequency content if compared with the concave middle one. Hence, the middle concave vibration is mainly caused by the vibration due to the crops.

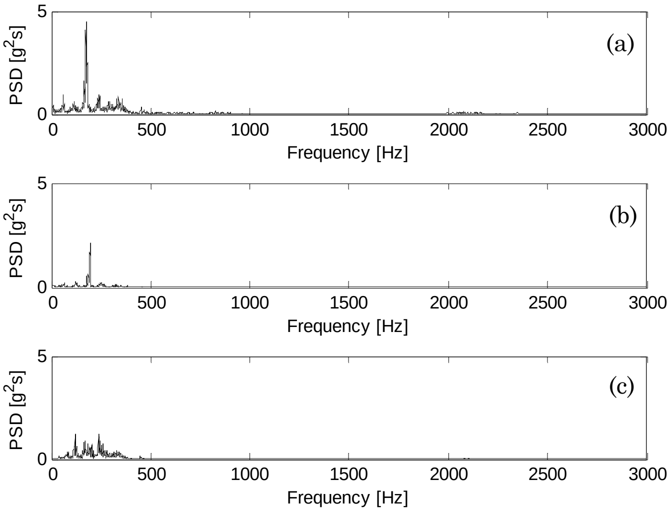

Fig. 4.12 – Position: concave middle - PSD of the vibration signal - Radial direction - Runs: (a) 54, (b) 36, (c) 12.

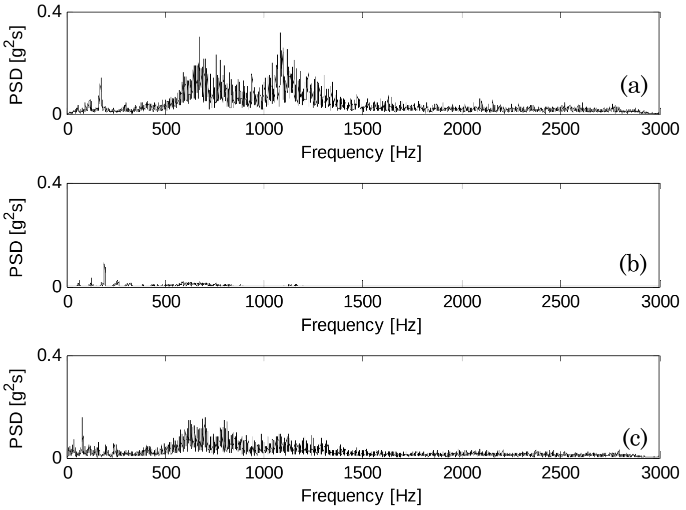

Fig. 4.13 – Position: concave rear - PSD of the vibration signal - Radial direction - Runs: (a) 54, (b) 36, (c) 12.

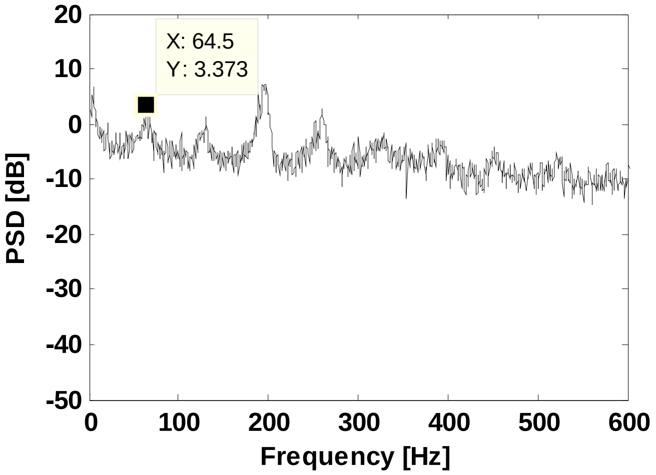

Fig. 4.14 – Run 27 - Position: concave middle; Radial direction. PSD of the vibration signal: focus on the 0-600 Hz frequency range.

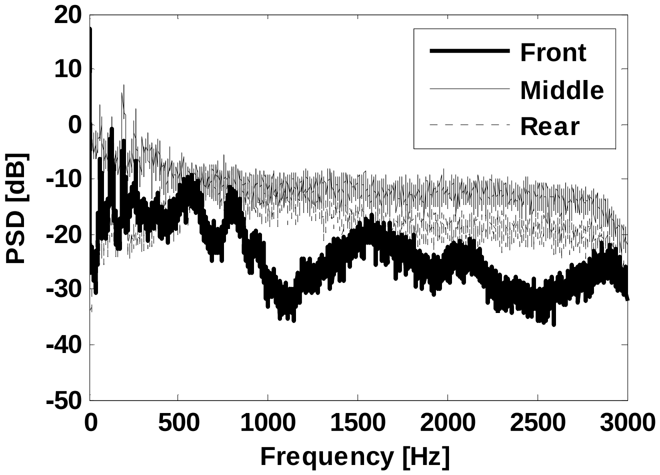

Fig. 4.15 – Run 27 - Different concave positions - Radial direction: PSD in the entire bandwidth

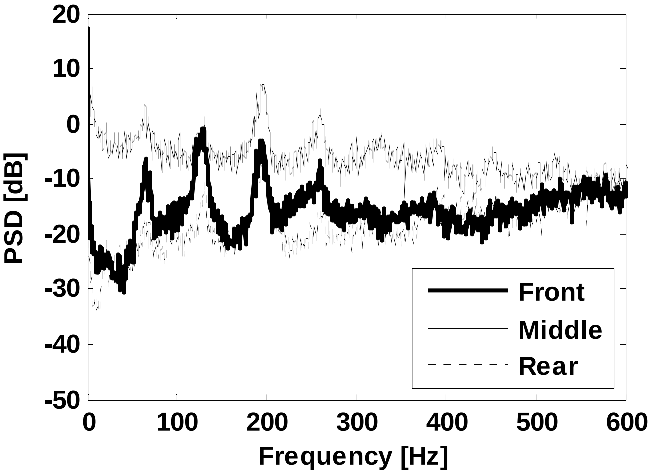

Fig. 4.16 – Run 27 - Different concave positions - Radial direction: PSD in the range 0-600 Hz.

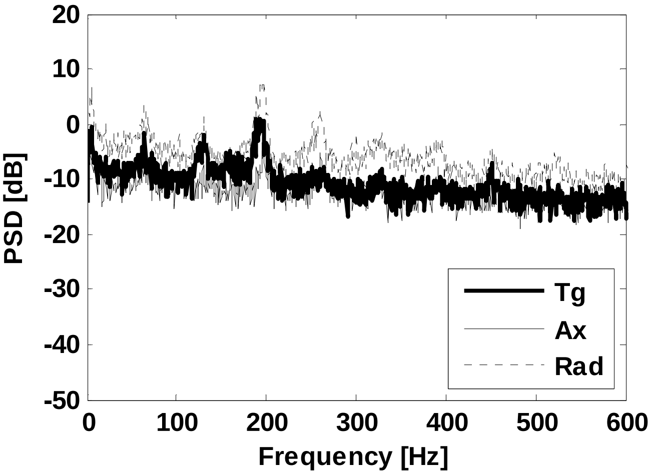

Fig. 4.17 – Run 27 - Concave middle position - 3 directions: PSD in the range 0-600 Hz.

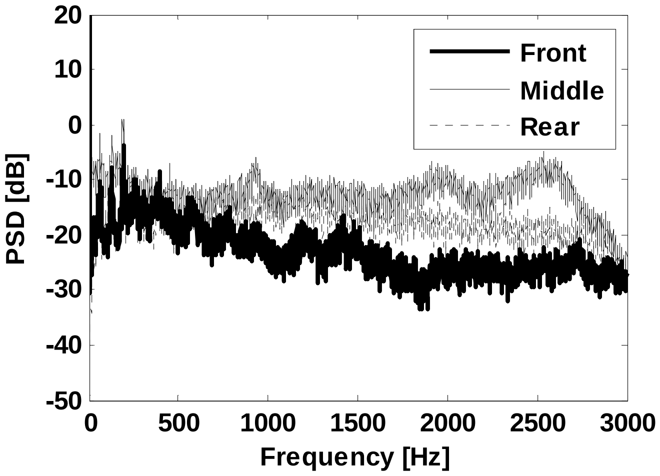

Fig. 4.18 – Run 27 - Different concave positions - Tangential direction: PSD in the entire bandwidth.

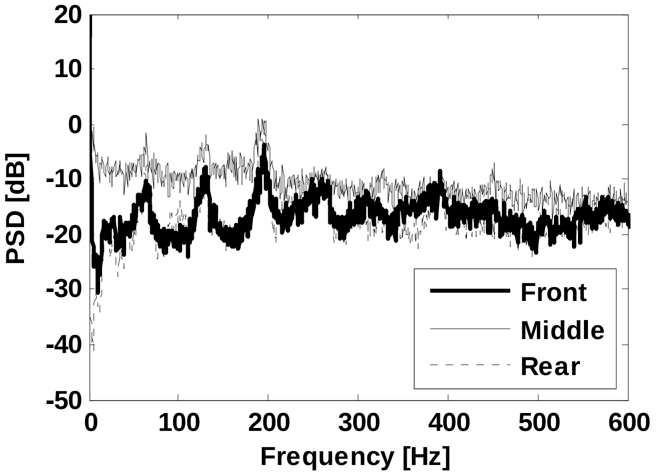

Fig. 4.19 – Run 27 - Different concave positions - Tangential direction: PSD in the range 0-600 Hz.

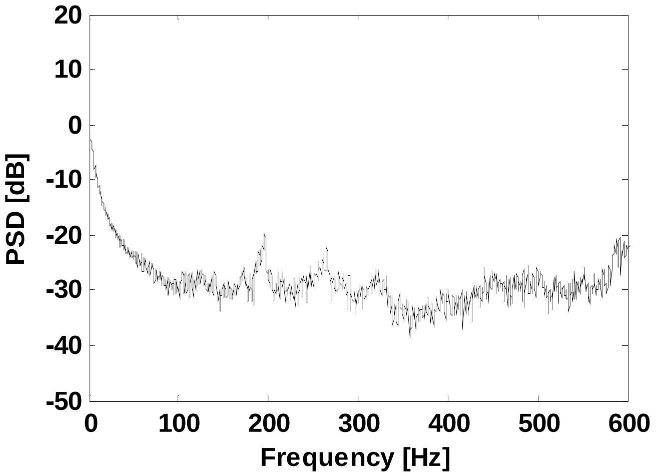

Fig. 4.20 – Run 27 -Position: frame; Radial direction. PSD of the vibration signal: focus on the 0-600 Hz frequency range.

On the basis of these first outlines the concave middle radial accelerometer signal could be considered as the most linked to the threshing process and it can be taken as the reference for the condition monitoring procedure. Based on the frequency behaviour described above, this signal can be decomposed in 3 different components:

- a component measured in idle condition due to the vibration of the mechanical parts in operation;
- a sinusoidal component given by the superposition of the F_{bar} and its harmonics;
- a broadband component.

In order to illustrate these components (see Fig. 4.21) the sinusoidal part and the broadband noise are synthesized.

It is worth noting that the broadband spectrum component keeps the response of the concave to two vibration sources:

- turbulence due to the threshing flow;
- hits of the kernels that impact the concave.

For this reason the noise has not to be neglected during the analysis but has to be considered as “operational” noise given by the process itself.

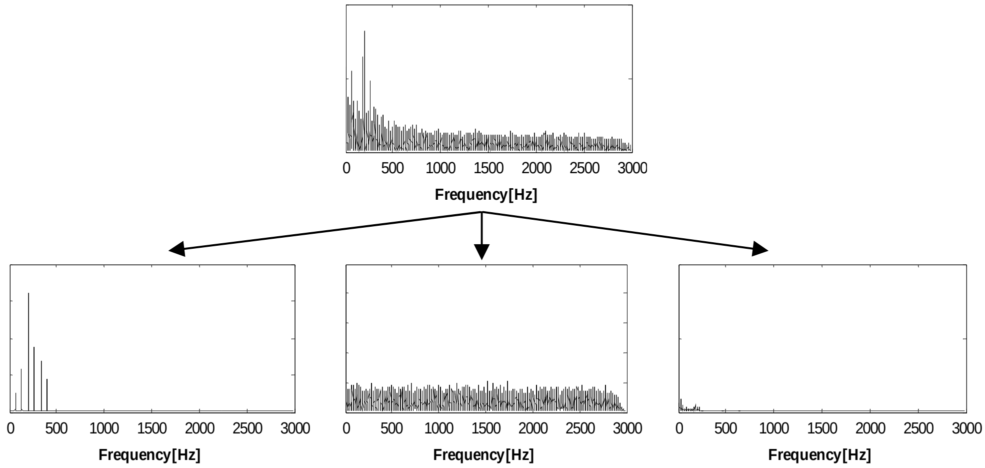

(a) (b) (c)

Fig. 4.21 – Real concave middle vibration signal decomposition: (a) Synthesized sinusoidal component in load condition; (b) Synthesized noise component in load condition; (c) Measured raw signal in idle conditions.

4.5.2. Rotorplate accelerometer signals

Considering the front and rear rotorplate accelerometer signals, both show the well known frequency behaviour in the first 600 Hz (see Fig. 4.22 and Fig. 4.23): here it is possible to distinguish the F_{bar} and its 7 harmonics.

These facts confirm the results achieved through the frequency analysis of the vibration measured on the concave.

Concerning the rear signal, a big amount of energy in this range is localized in the 1650-1950 Hz band indicating a resonance.

Although the front and rear rotorplate accelerometer signals are mounted at the beginning of the threshing zone and at the end of the separation zone respectively, they show the same amount of energy in the first 600 Hz. Differences in energy level can be observed in the 600-3000 Hz frequency range with the exception of the resonance band as a consequence of the different amount of crop processed in the separation zone.

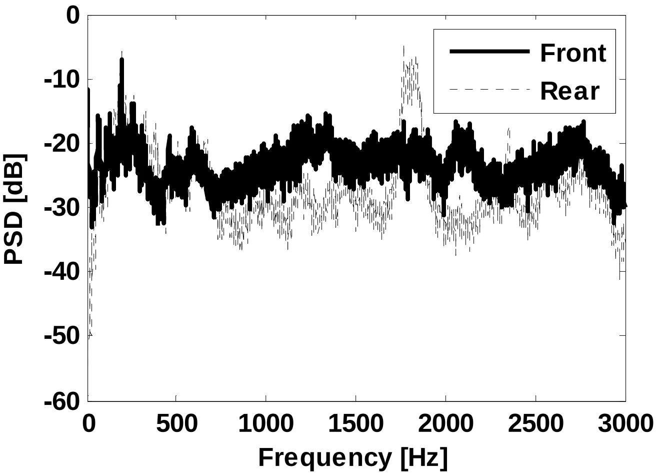

Fig. 4.22 – Run 27: PSD of the front and rear rotorplate vibration signals in the entire bandwidth.

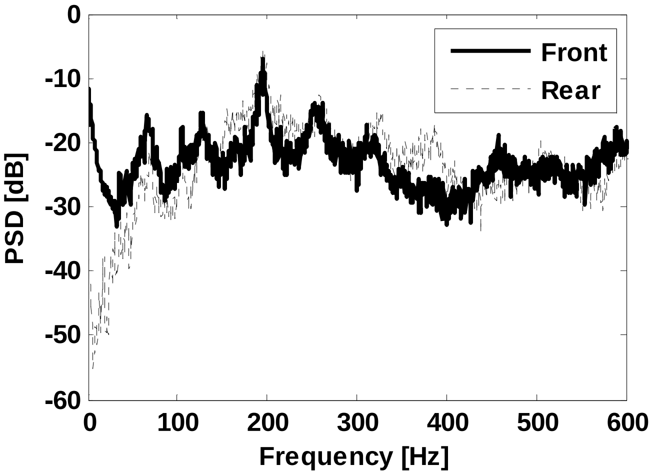

Fig. 4.23 – Run 27: PSD of the front and rear rotorplate vibration signals in the 0-600 Hz frequency range.

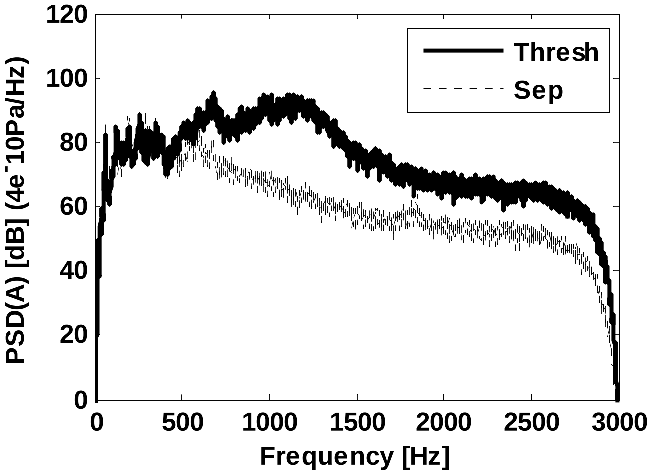

Fig. 4.24 – PSD of the sound pressure measured by threshing and separation microphones.

4.5.3. Threshing and separation microphone signals

The PSD's of the threshing and separation microphone signals depicted in Fig. 4.24 and Fig. 4.25 confirm the results achieved for the accelerometer signals. Both microphone signals show the characteristic frequency F_{bar} and harmonics in the first 600 Hz. The Overall Level of the sound pressure calculated (but not reported here) of the threshing microphone is proved to be higher than the one calculated for the separation one for all runs carried out. This fact is due to the changes in amount of crop processed between the two zones. However, the differences in spectral energy are more relevant in the range 600-3000 Hz where the spectrum is dominated by the response to the threshing turbulence and the threshing of the crop against the concave.

It can be noted that the interactions between the rasp bars and the concave are still evident in the separation zone as confirmed by the rotor plate rear accelerometer that is placed in correspondence of the separation zone. The interactions are still evident in the separation zone because of the presence of the straw even if the amount of crop processed is decreasing.

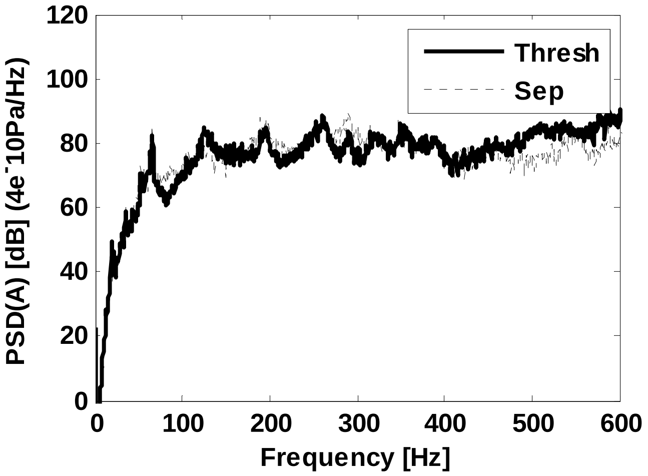

Fig. 4.25 – PSD of the sound pressure measured by threshing and separation microphones: focus on the 0-600 Hz frequency range.

It is worth noting that the PSD's are calculated after applying the A-weight in order to reproduce the human ear sensitivity to different frequencies. On the basis of the PSD analysis it can be noted that we can found the F_{bar} and its first harmonics within the range of the maximum amplification of the A-weight. Therefore the sound due to the rasp bar interactions can be easily listened by the human ear.

4.6 Condition monitoring procedure

As previously said, the threshing process is due to two principal mechanisms: the "grain over grain" threshing and the friction of the crop over the concave. Moreover it is worth noting that the rotor crop distribution and, consequently, the efficiency of the process is strongly influenced by a series of operational parameters. For instance, due to the "grain over grain" threshing, an increase of capacity (quantity of the crop processed) should mean an increase of the threshing efficiency in terms of lower losses. Moreover, a faster rotor speed and a lower concave distance should assure a better crop separation but making the threshing more aggressive causing an inferior crop quality.

This Section treats the processing of the accelerometer and microphone signals measured in both stationary (i.e. indoor) and field (i.e. outdoor) testing conditions.

This kind of analysis has been done in order to evaluate the effects of some operational parameters over the vibro-acoustic response of the threshing unit.

The following operational parameters have been taken into account during the analysis:

- capacity (i.e. amount of the processed crop);
- concave distance (i.e. radial distance between the rotor and the concave);
- rotor speed;
- degree of moisture;
- grain to straw ratio.

The selection and extraction of proper features from the time domain signals has been carried out in order to search good correlations between the features and some efficiency parameters that can describe the efficiency of the threshing process. The features extracted are the following:

- RMS which reflects the energy of a signal;
- Crest Factor (CF), Temporal Kurtosis (TK) and Impulse Factor (IF) which reflect the level of peakness of a signal;
- Approximate Entropy (AppEn) which reflects the regularity of a signal;
- Sound quality metrics, such as Loudness and Sharpness, which extract information from the sound pressure signals measured outside the cabin. These metrics take into account the non linearity of the human ear and can be used to validate the results obtained from the accelerometer signals.

The efficiency parameters that have been considered are:

- losses;
- distribution of the crop over the sieve;
- amount of broken kernels (in this work grain kernels have been considered).

Although one of the purposes of the feature extraction is to visually check the correlations with the efficiency parameters, the vibro-acoustic features can be also easily used as input parameters of a genetic algorithm in order to find more rigorously which is the feature best correlated with the efficiency parameters to search the best regression model that can be used to predict the efficiency parameters.

4.6.1. Influence of the operational parameters

4.6.1.1 Influence of the capacity

The influence of the capacity over the vibro-acoustic response has been evaluated comparing different runs carried out in stationary conditions at two different rpm rotors set at 1350 and 945 rpm. The influence of the capacity is analyzed for different machine settings having different concave distance values. For the sake of brevity it will be shown hereafter the graphs related to the runs carried out at 1350 rpm with 5, 13 and 25 mm concave distances. The setting parameters of the runs processed are collected in the Table 14, Table 15, and Table 16. First of all, the analysis of the PSD's in the range 150-250 Hz was needed to understand how the characteristic frequency F_{bar} and its harmonics are influenced by the changes in amount of crop processed by the threshing unit. As made before, the PDS spectra have been plotted with the y-axis scaled in dB values taking 1 g^2/Hz as a reference.

The cursor discussion concerning the variations of the second harmonic of the F_{bar} (that shows the highest amplitude) is added to the RMS calculation carried out in the 150-250 Hz frequency band. Observing the Fig. 4.26 and Fig. 4.27, that depict the PSD of the concave middle radial signal, it can be noted that the second harmonic of F_{bar} (2X F_{bar}) shifts towards higher frequencies as the capacity decreases. This behaviour, that can be due to the increase of the rotor speed due to the decrease of the load, has been verified for all the rpm and concave distance settings. Concerning the amplitudes assumed by the 2X F_{bar} at different capacity settings, it is not easy to detect relevant differences. What we can observe is that the peaks become sharper going towards lower capacities because of less speed irregularities.

Table 14 – Influence of capacity (1350 rpm and 5 mm).

Operational parameters		Run			
		27	**26**	**28**	**31**
Concave distance	[mm]	5	5	5	5
Rotor speed	[rpm]	1350	1350	1350	1350
Capacity	[ton/h]	91.1	72	50	10
RMS 150-250 Hz	[dB]	18.35	17.75	16.21	16.52

Table 15 - Influence of capacity (1350 rpm and 13 mm).

Operational parameters		Run					
		54	**02**	**55**	**03**	**07**	**08**
Concave distance	[mm]	13	13	13	13	13	13
Rotor speed	[rpm]	1350	1350	1350	1350	1350	1350
Capacity	[ton/h]	110	102	90	72	30	10
RMS 150-250 Hz	[dB]	18.73	18.19	15.56	14.18	14.45	15.09

Table 16 - Influence of capacity (1350 rpm and 25 mm).

Operational parameters		Run			
		19	**17**	**18**	**23**
Concave distance	[mm]	25	25	25	25
Rotor speed	[rpm]	1350	1350	1350	1350
Capacity	[ton/h]	102	72	50	10
RMS 150-250 Hz	[dB]	13.15	12.20	11.16	11.17

However, as indicated by the Table 14, Table 15 and Table 16, the RMS values assumes higher values at lower capacities.

As a matter of a fact Fig. 4.26, and Fig. 4.27 show that the peak of the 2XF_{bar} becomes the sharpest at 10 ton/h capacity. So, it is evident that regular interactions between the concave and the rotors can achieved decreasing the amount of crop processed. Concerning the rotorplate front vibration signal (see Fig. 4.28) measured in correspondence of the threshing zone, it still shows the capacity-

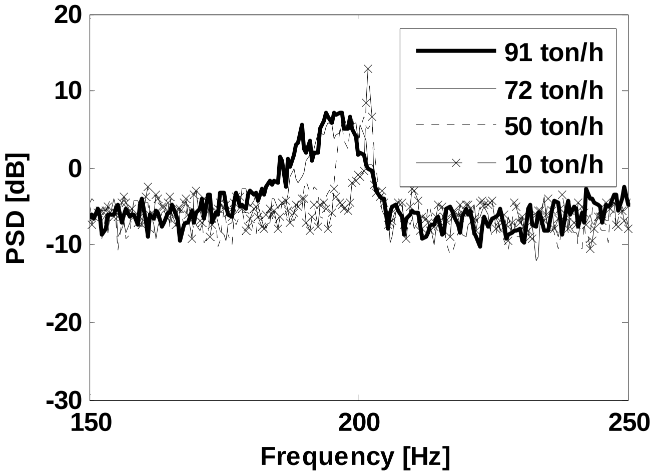

Fig. 4.26 – Concave middle radial vibration signal: influence of capacity at 1350 rpm and 5 mm concave distance (see Table 14).

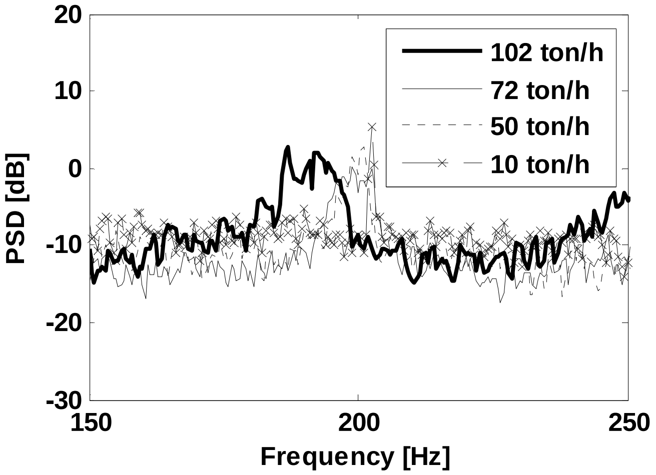

Fig. 4.27 – Concave middle radial vibration signal: influence of capacity at 1350 rpm and 13 mm concave distance (see Table 15).

dependent shifts in frequency confirming what found through the concave middle accelerometer analyses.

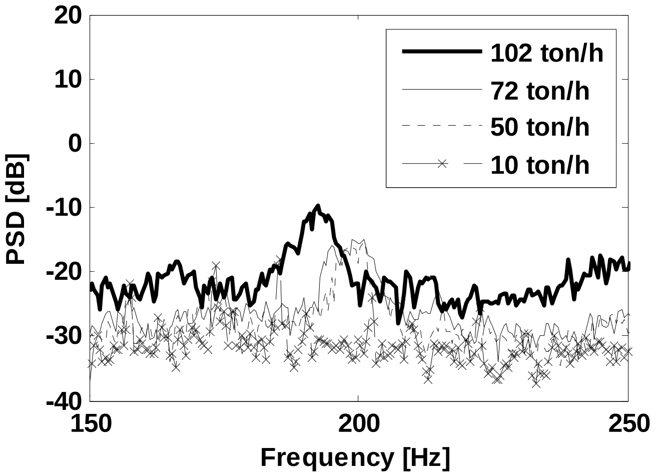

Fig. 4.28 – Rotorplate front vibration signal: influence of capacity at 1350 rpm and 25 mm concave distance (see Table 16).

Furthermore the amplitude of the peak is clearly influenced by the variations in capacity whilst its sharpness is not affected by such variations. Therefore, we can suppose that the speed irregularities do not affect the rotorplate vibration response. Actually, based on the experiments described above, we may obtain an accurate description of the effects of the capacity in the frequency domain.

However, in order to understand more accurately the capacity-dependent energy variation of the vibration signal, a time domain feature extraction is needed. For each signal, several features (mentioned above) are extracted for different time records by means of a fixed time segmentation of each run (see Section 4.4.3).

After that, all the feature values are averaged obtaining one value for each signal. Quadratic spline lines were needed to fit the feature trends calculated with respect of the setting parameters.

RMS

An Averaged RMS value (Av. RMS) has been calculated averaging the RMS values obtained for time records of 2 s. This has been done for runs carried out at different capacity settings.

Fig. 4.29 (a) and (b) concern the front and rear concave radial vibration signals depicting the correlations obtained fitting the Av. RMS values vs. capacity for each concave distance. It is clearly evident that for both signals their energy increases as the capacity increases. This behaviour is verified to be the same for each concave distance setting. It has to be noted that the influence of the concave distance is more evident at high capacities. Fig. 4.29 (c) illustrates the correlation obtained for the concave middle radial signal showing quite constant trends. Observing the trends obtained at 13 mm it is confirmed what previously found by means of the frequency analysis: the RMS is high at low capacities.

Temporal Kurtosis (TK)

The Av. Temporal Kurtosis (TK) was calculated averaging the Temporal Kurtosis values obtained for time records of 2 s. Fig. 4.30 shows that the Av. TK extracted from front and rear accelerometer concave signals is not correlated with capacity. Concerning the middle concave radial signal, the 35 mm concave setting presents a decrease of the Av. TK when the capacity increases. This behaviour can be caused by the fact that at that concave distance at higher capacities the kernels have less space to impact the concave, so that the peakness of the signal decreases. Concerning the other trends obtained at lower concave distances they seems to be not influenced by capacity variations. Moreover, it is evident that as the concave distance increases, the Av. TK increases: in the following Section the correlations Av. TK vs. concave distance will explain better this phenomenon.

Crest (CF) and Impulse (IF) Factors

The Crest Factor (CF) and Impulse Factor (IF) were calculated in order to search better correlations between the degree of peakedness of the filtered concave middle radial signal at high capacities (600-3000 Hz) and the capacity. The Av. CF, that is less sensitive to the presence of high peaks compared to the TK, shows a constant trend at 5 mm concave distance. Apart this fact, no further improvements were obtained.

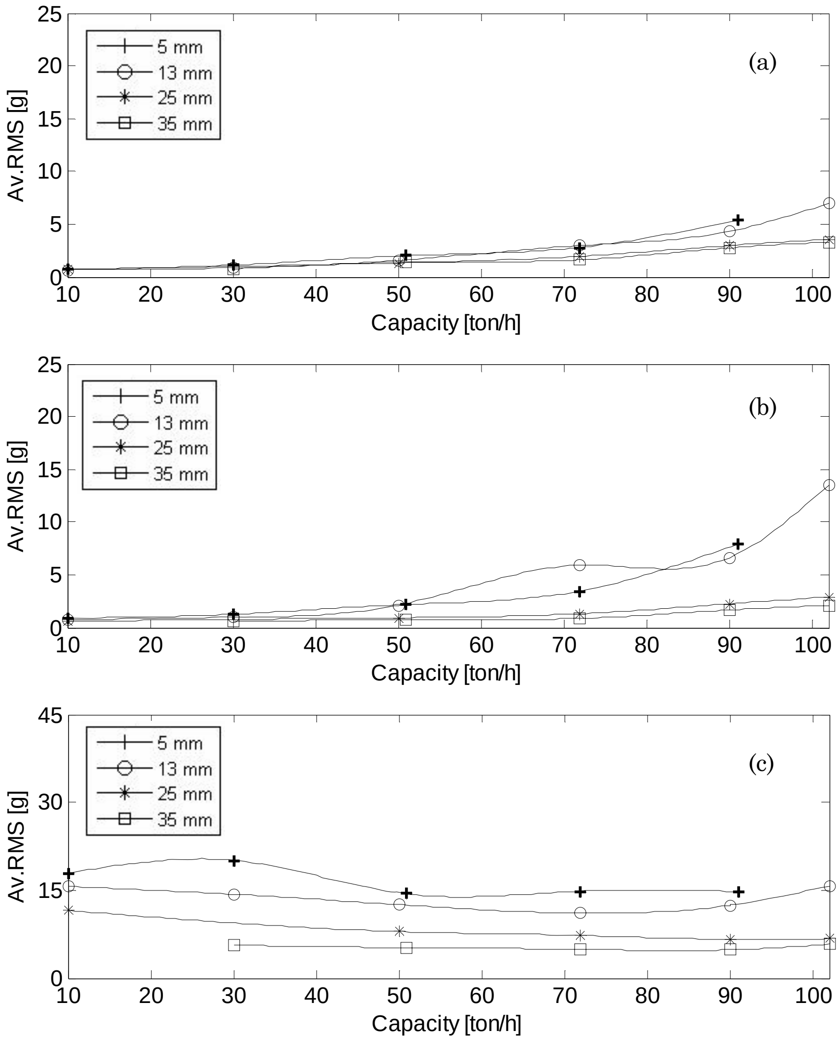

Fig. 4.29 – Av. RMS vs. capacity - Concave radial vibration signal: (a) front, (b) rear, (c) middle positions.

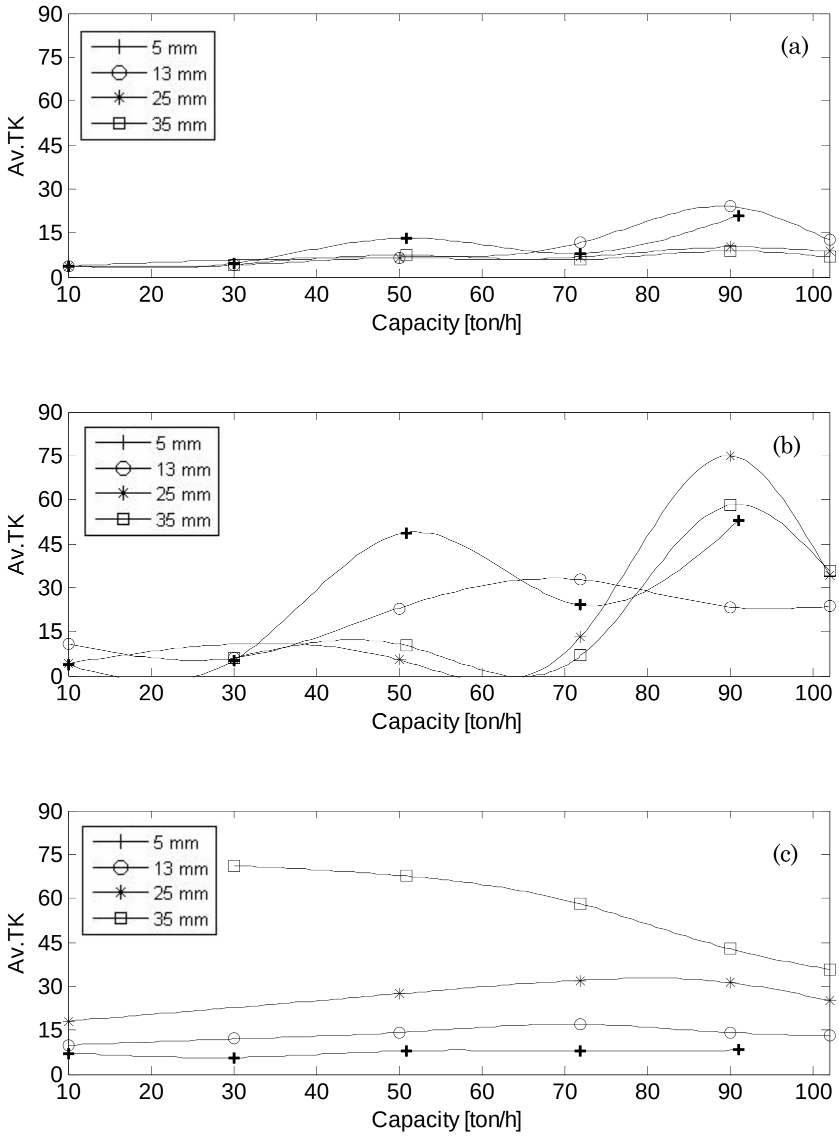

Fig. 4.30 – Av. TK vs. capacity - Concave radial vibration signal: (a) front, (b) rear, (c) middle positions.

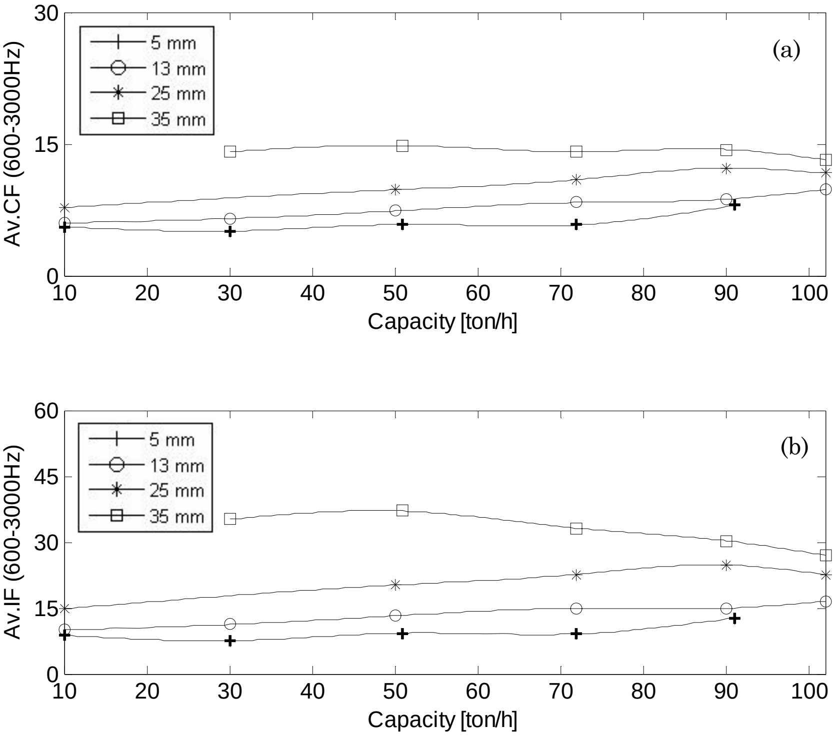

Fig. 4.31 – Av. (a) CF and (b) IF vs. capacity - Filtered middle concave radial signal (600-3000 Hz).

Approximate Entropy (AppEn)

As said in Chapter 2, the AppEn was calculated for 0.5 s time records for computational reasons. Its averaged value, the so-called Av. AppEn, extracted from the concave middle radial signal shows a slight increase as the capacity increases. Therefore, it seems that the irregularity of the signal increases as a consequences of the higher threshing turbulence at high capacity.

Hence, it the AppEn can be considered a useful indicator to explain the concave vibration due to the so-called “grain to grain effect” that causes the threshing turbulence.

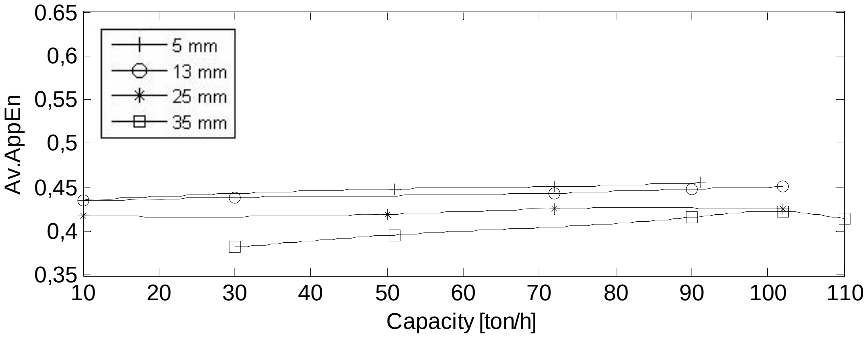

Fig. 4.32 – Av. AppEn vs. capacity – Raw concave middle radial signal.

Loudness and Sharpness

The common sound quality metrics are extracted from the sound pressure signal measured by the microphone placed outside the cabin.
It is well known that the Loudness is a perceptual measure of the effect of the energy content of a sound on human's ear and the Sharpness is a measure of the high frequency content of a sound. These metrics seem to be well suited to describe the threshing sound that can be heard by an external receiver. Moreover they can extract information that can be compared with the ones obtained from the transducers mounted inside the threshing units (concave and frame accelerometers, threshing and separation microphones).

The averaged values of these two metrics have been correlated with the capacity as done for the previous features. In this Section and in the rest of the chapter the values of the sound quality metrics are neglected for confidential reasons. From Fig. 4.33 it can be observed that both metrics assume higher values for higher capacities showing a quadratic trend for all concave distance settings with the exception of 25 mm that presents a point of instability at 10 ton/h capacity. This fact means that the outside microphone signal is sensitive to the increase of capacity. Moreover although the sound measured from the external microphone is produced by all mechanical parts in operation (i.e. engine, rotor, transmissions, etc..) the noise due to the threshing mechanisms seems to be still relevant.

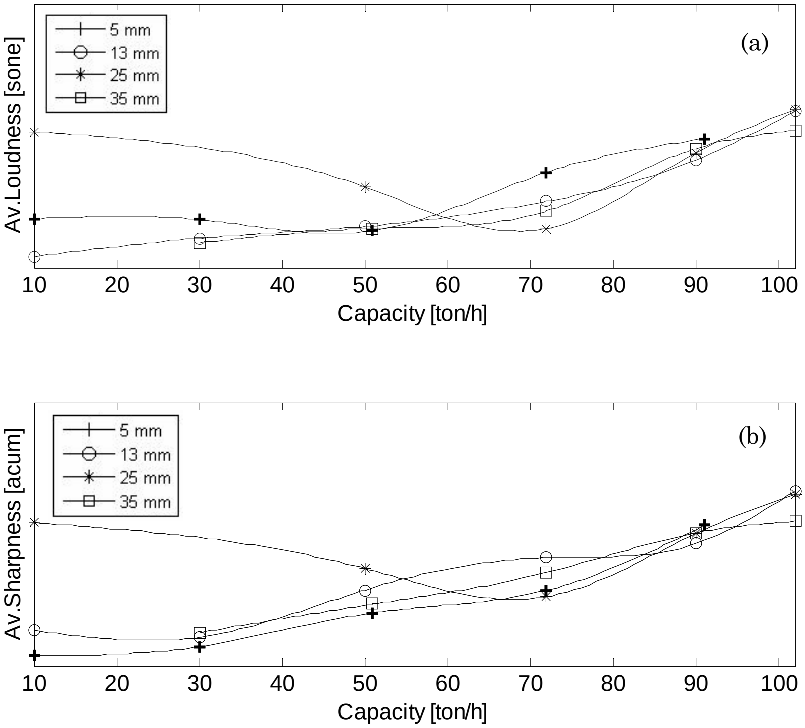

Fig. 4.33 – (a) Loudness and (b) Sharpness of the sound pressure signal measured by the microphone outside the cabin.

4.6.1.2 Influence of the concave distance

The concave distance setting parameter is probably the most critical: a good crop distribution and, consequently, the quality of the crop threshed are strongly dependent on this parameter that can be tuned by the user during the on-the-go field operations.

The preliminary analysis of the PSD spectra (still plotted with the y-axis scaled in dB values taking 1 g^2/Hz as a reference) zoomed in the range 150-250 Hz, clearly shows the influence of the concave distance over the frequency behaviour of the concave middle radial signal for Runs listed in Table 17. As confirmed by the plot depicted in Fig. 4.34, the amplitude of the 2X F_{bar} increases as the concave distance decreases. This fact is confirmed by the signal measured by the front rotorplate accelerometer mounted in correspondence of the threshing zone (see Fig. 4.35) and it is valid also for low capacity settings (Fig. 4.36). Observing the plots it seems that the changes in concave distances do not cause any rotor speed variations and, consequently, shifts in frequency of the F_{bar} and harmonics.

Based on the frequency analysis achievements let’s quantify the signal energy increasing calculating the time domain Av. RMS. Moreover the TK is also calculated in order to investigate the degree of peakedness of the signal. Fig. 4.37 depicts the trends related to the evolution of these two features for different time segments can be taken as an on-line monitoring tool by the user to evaluate the vibration of the concave at different concave distance configurations during the field operations.

From the plot depicted in Fig. 4.37 it can be observed that the RMS obtained for segmented time histories at different concave distances are clearly separated from each other showing higher values at higher concave distances. On the other hand, the TK trends remain mostly overlapped. However from Fig. 4.37 (b) it can be observed that an increase of the concave distance causes an increase of the peakness of the signal. In order to quantify the effects of the concave distance over the time signal features, the same analysis procedure adopted in the previous Section has been carried out.

Table 17 – Influence of concave distance (1350 rpm and 90 ton/h capacity)

Operational parameters		Run			
		34	**16**	**55**	**27**
Concave distance	[mm]	35	25	13	5
Rotor speed	[rpm]	1350	1350	1350	1350
Capacity	[ton/h]	90	90	90	90

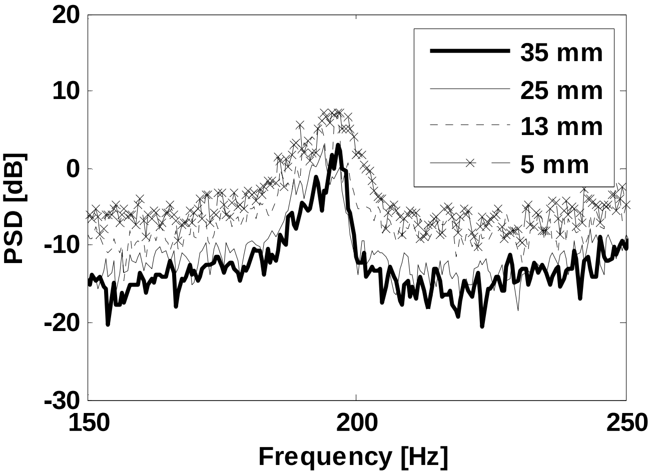

Fig. 4.34 – Concave middle radial vibration signal: influence of concave distance at 1350 rpm and 90 ton/h capacity (see Table 17).

Table 18 - Influence of concave distance (1350 rpm and 90 ton/h capacity)

Operational parameters		Run			
		40	**23**	**08**	**31**
Concave distance	[mm]	35	25	13	5
Rotor speed	[rpm]	1350	1350	1350	1350
Capacity	[ton/h]	10	10	10	10

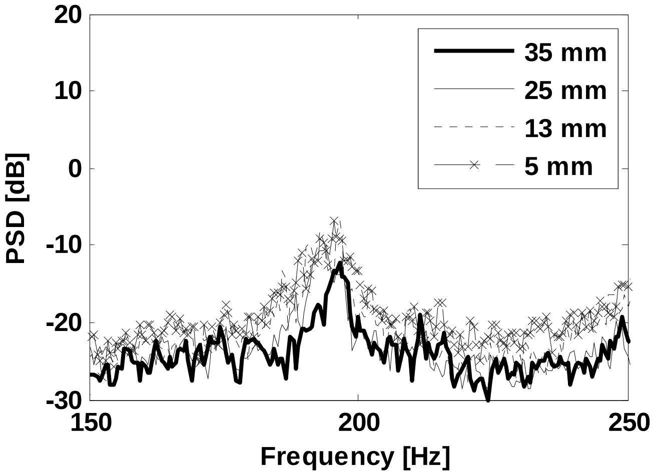

Fig. 4.35 – Rotorplate front vibration signal: influence of concave distance at 1350 rpm and 90 ton/h capacity (see Table 17).

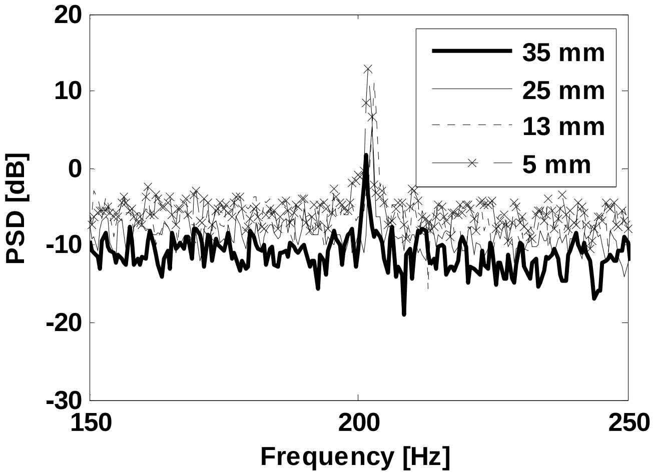

Fig. 4.36 – Concave middle radial vibration signal: influence of the concave distance at 1350 rpm and 10 ton/h capacity (see Table 18).

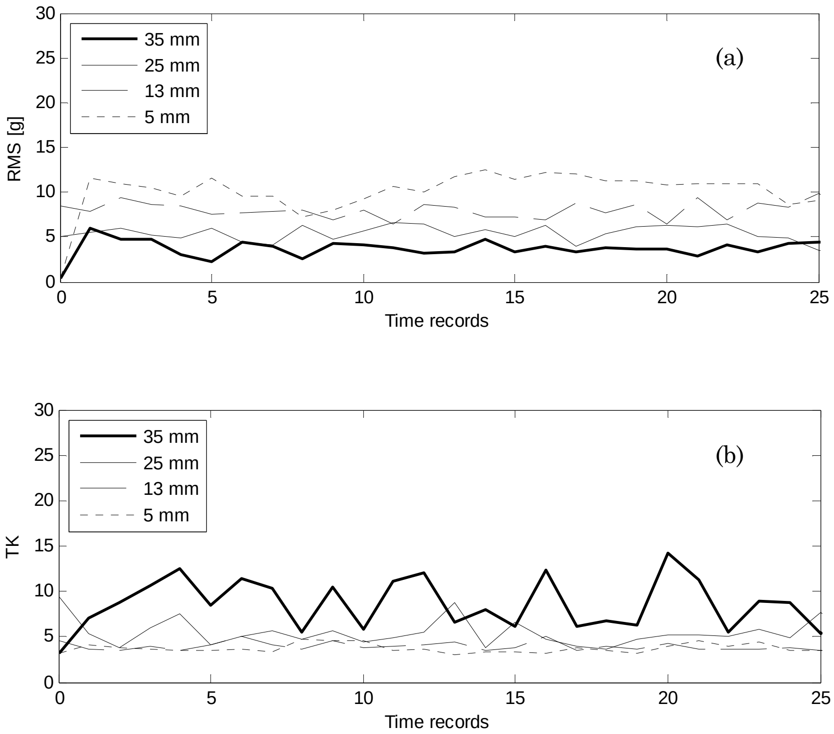

Fig. 4.37 – Concave middle radial vibration signal: evolution of (a) RMS and (b) TK at 50 ton/h capacities for different concave distances.

RMS

Looking at Fig. 4.38 it can be observed a very good correlation existing between the energy of all concave accelerometer signals and concave distance: as the concave distance increases the Av. RMS decreases in a less than linear way. This is true for all the capacity settings tested. As seen before, when capacity is set at 10 ton/h higher values are obtained.

Concerning the middle concave accelerometer signal the application of the adaptive multiband filter (see Fig. 4.38 (e)) does not bring further improvements to the correlation. Based on these achievements we are able to link the concave vibration with the concave distance.

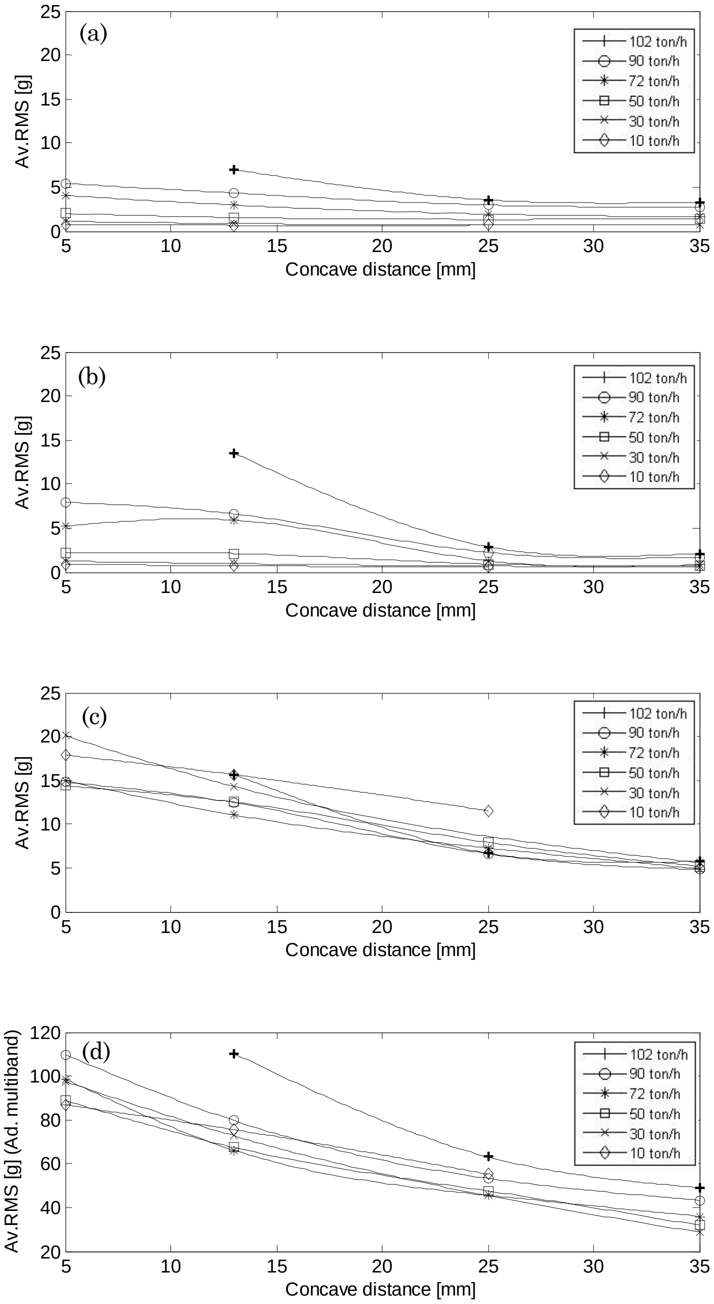

Fig. 4.38 – Av. RMS vs. concave distance - Concave rad. vibration signal - positions: (a) front, (b) rear, (c) raw middle, (d) filtered middle.

Temporal Kurtosis (TK)

Through the evaluation of the Av. RMS trends we get an idea of the global vibration of the concave. Analysing the Av. TK we can related to that part of vibration due to impulsive components. From Fig. 4.39 (a) and (b) it is found that bad correlations could be found extracting the Av. TK from front and rear concave signals: the peakness of these signals seems to be insensitive to concave distance variations probably because of the transducers are mounted close to bearing supports. On the other hand the TK of the concave middle radial signal (see Fig. 4.39 (c)) presents good correlations with the concave distance variations. An increase of the concave distance causes an increase of the TK. This behaviour is probably due to the changes in crop distribution: at higher concave distances the crop is more spread between the concave and the rotor. Because of this fact more space is available for the kernels that can impact more easily the concave. Hence we can refer to a sort of saturation effect happening at low concave distances. It is worth noting that the TK increases for certain capacities (30, 50, 72 ton/h) than others. The 10 ton/h is too lower to give relevant TK values.

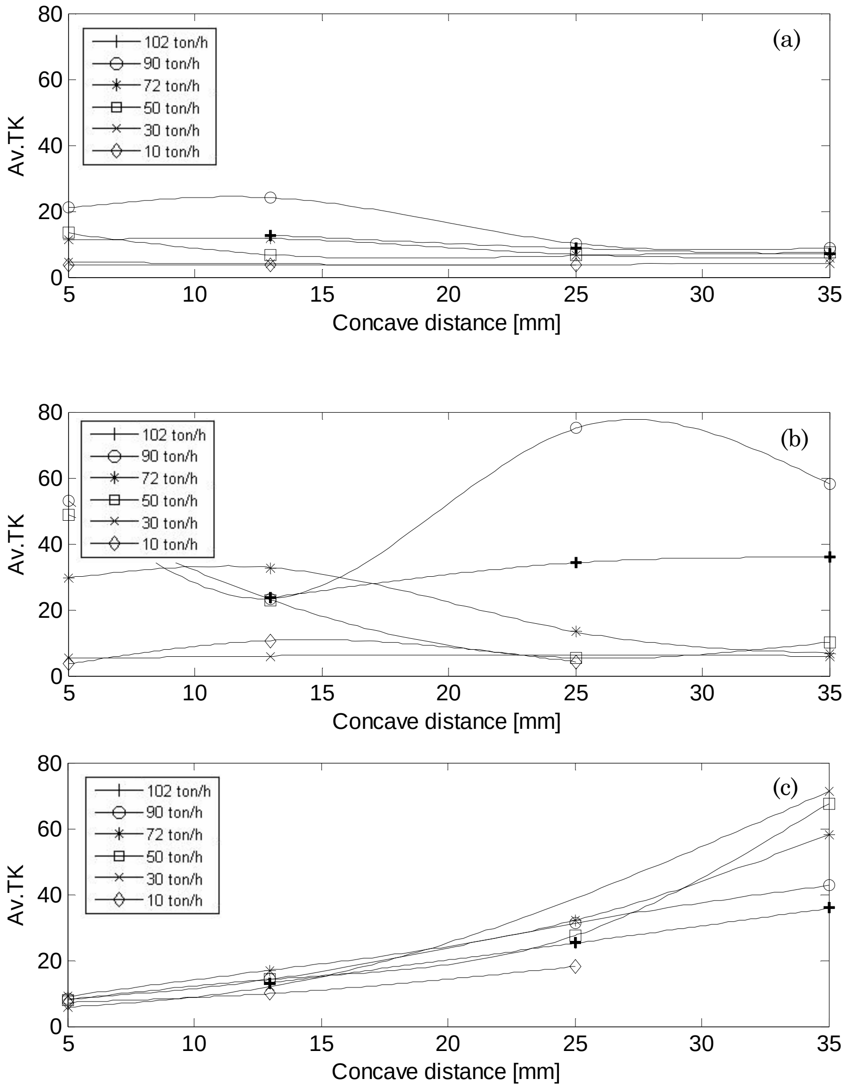

Fig. 4.39 – Av. TK vs. concave distance - Concave radial vibration signal: (a) front, (b) rear, (c) middle positions.

Crest (CF) and Impulse (IF) Factors

Fig. 4.40 depicts the correlations obtained for CF and IF with respect of the concave distance. It can be noted that they confirm the results obtained for the TK. Hence, these features do not bring significant improvements to the TK correlations.

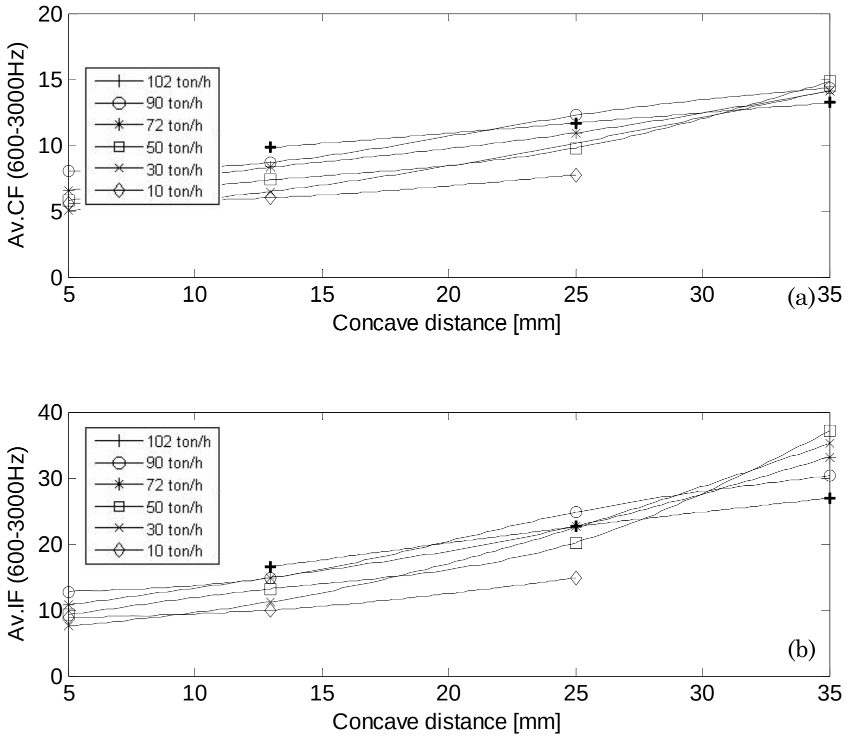

Fig. 4.40 – Av. (a) CF and (b) IF vs. concave distance - Filtered middle concave radial signal (600-3000 Hz).

Approximate Entropy (AppEn)

The effect of the concave distance over the regularity of the concave middle radial signal can be evaluated through the analysis of the AppEn. The Fig. 4.41 illustrates the trends obtained: plotting the Av.AppEn vs. concave distance it is clear that the regularity of the time signal decreases going towards higher concave distances. It is worth noting that the trends assume linear behaviour in the range 13-25 mm concave distances for all capacities. It can be concluded that the threshing noise is more relevant at low capacities as expected.

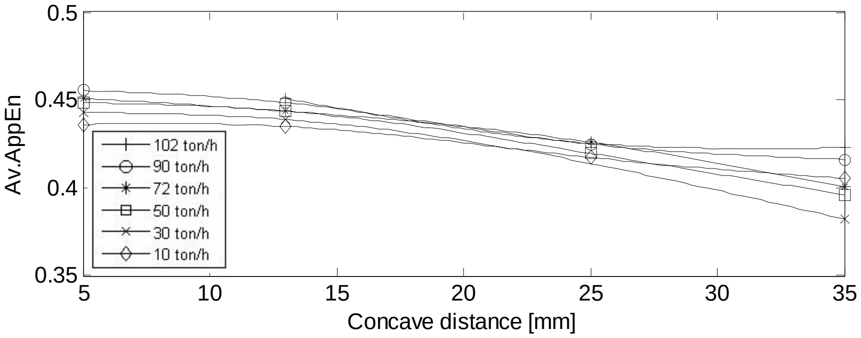

Fig. 4.41 – Av. AppEn vs. concave distance – Raw concave middle radial signal.

Loudness and Sharpness

The Loudness and Sharpness metrics evaluated on the sound pressure signal measured by the microphone placed outside the cabin (see Fig. 4.42) seem to be insensitive to the concave distance variations. Both metrics present constant trends for each capacity with the exception of 10 ton/h that gives some instabilities at higher concave distance. As a matter of a fact the excitation is too low and it is reasonable that the microphone outside cannot be sensitive giving a bad correlation.

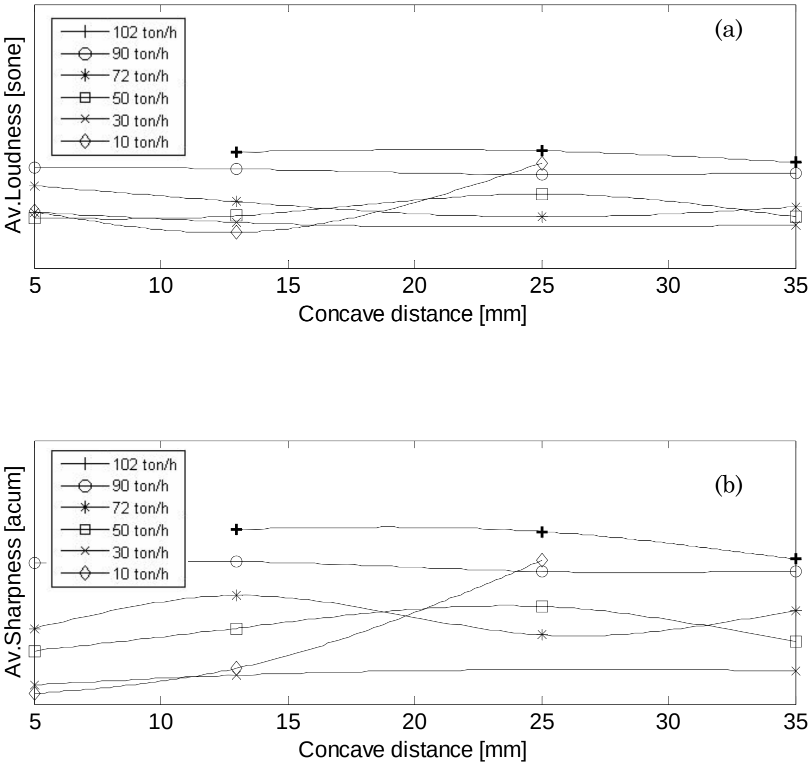

Fig. 4.42 – (a) Loudness and (b) Sharpness of the sound pressure signal measured by the microphone outside the cabin.

4.6.1.3 Influence of the rotor speed

The effect of the rotor speed over the frequency behaviour of the vibration signal is quite straightforward. The increase of the rotor speed obviously causes a shift of the 2XF_{bar} towards higher frequencies as can be noted observing Fig. 4.43 and Fig. 4.44.

Analysing the PSD of the concave middle signal in Fig. 4.43 it seems that the amplitude of the characteristic frequency increases as the rotor speed increases. On the other hand the amplitude of the 2XF_{bar} of the rotorplate signal (see Fig. 4.22) seems to be insensitive to the rotor speed variation.

The time domain analysis will help to understand how the signal energy varies as a consequence of changes in rotor speed.

RMS

Fig. 4.45 (a) and (b) show the correlations obtained calculating the Av. RMS for concave front and rear radial signals: the trends are not so straightforward showing a concavity point around 1150 rpm for both signals. This effect is more evident at high capacities. At higher rotor speeds the increase of the centrifugal force permits higher concave excitation. On the other hand at low rotor speed the axial velocity of the crop is lower and the interactions between the crop and the concave become more relevant causing higher concave vibration. This behaviour is confirmed by the middle concave signal at 102 and 72 ton/h. Concerning the other capacities they don’t follow the same trends obtained for rear and front concave positions showing an increase of the RMS as the rotor speed increases.

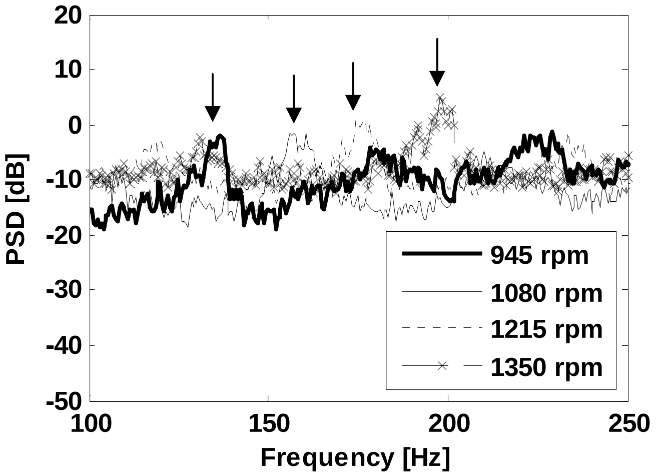

Fig. 4.43 – Concave middle radial vibration signal: influence of the rotor speed at 72 ton/h capacity and 13 mm concave distance.

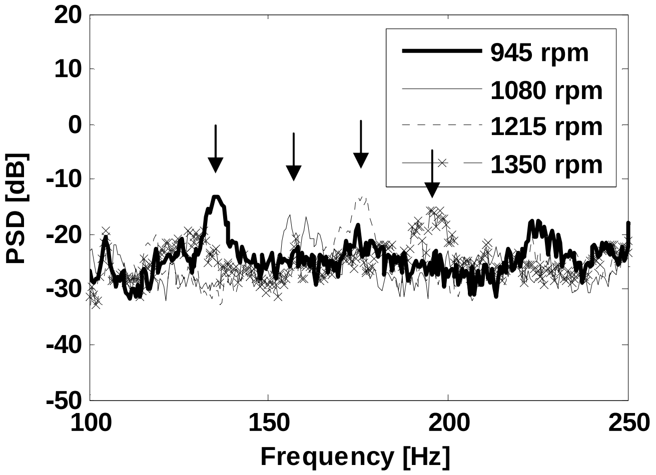

Fig. 4.44 – Rotorplate vibration signal: influence of the rotor speed at 72 ton/h capacity and 13 mm concave distance.

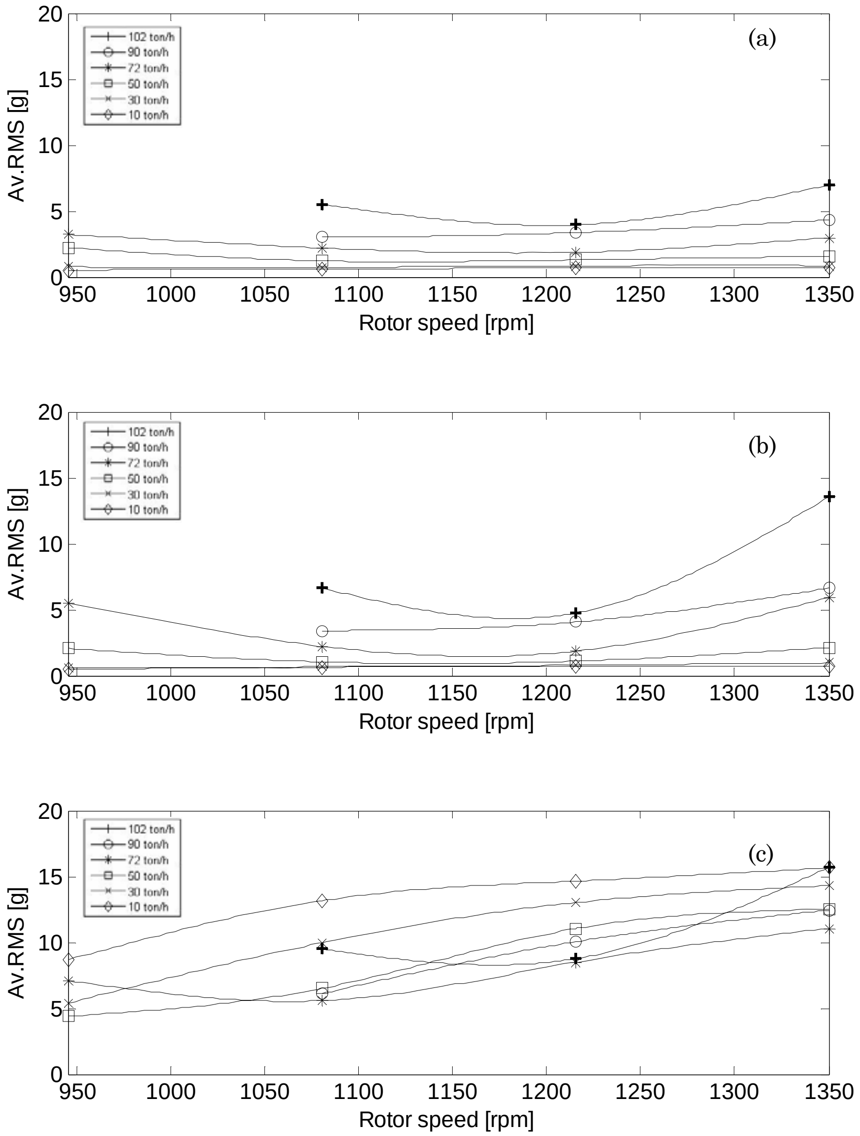

Fig. 4.45 – Av. RMS vs. rotor speed - Concave radial vibration signal: (a) front, (b) rear, (c) middle positions.

Temporal Kurtosis (TK)

Observing Fig. 4.46 it is found that it is not possible to find a clear link between TK and rotor speed for concave front and rear signals.

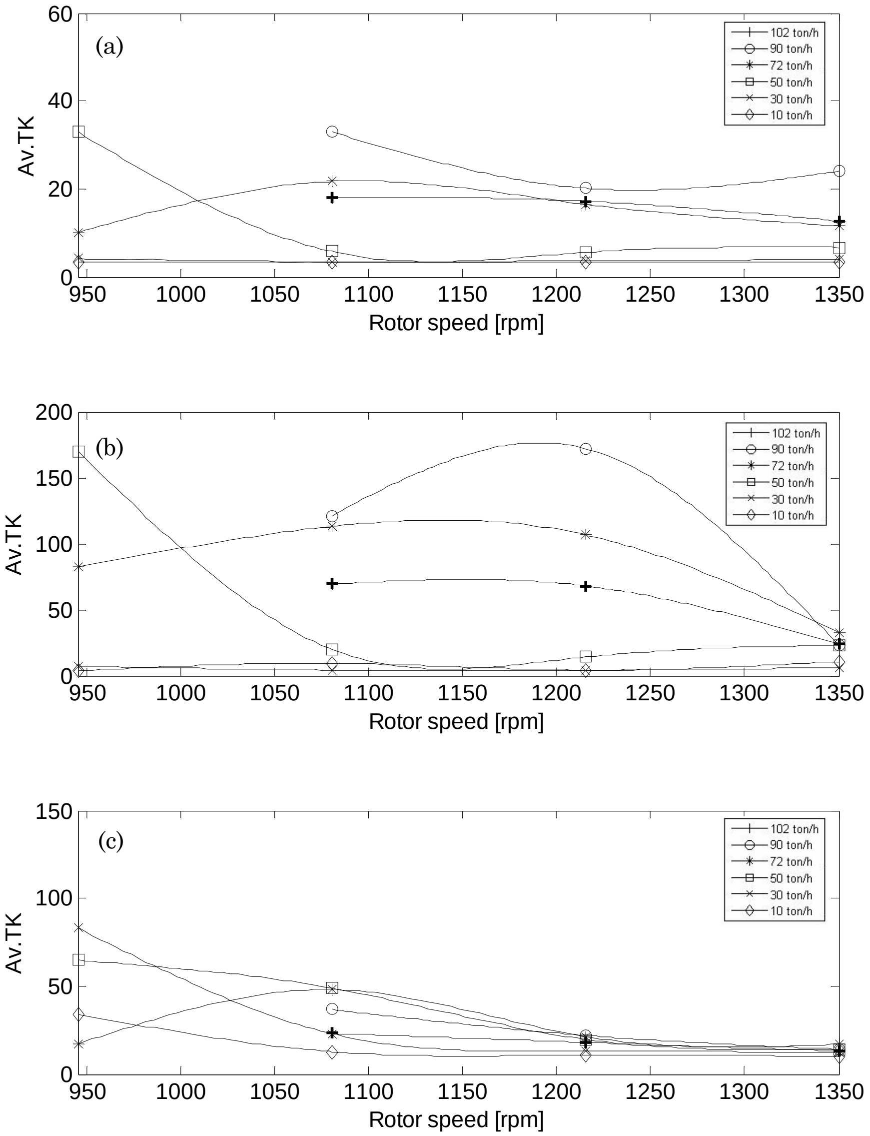

Fig. 4.46 – Av. TK vs. rotor speed - Concave radial vibration signal:(a) front, (b) rear, (c) middle positions.

Moreover high TK values can be obtained at low rotor speeds. As said before when the rotor is running slower the “grain over grain threshing” and consequently the threshing turbulence is less relevant than the threshing of the kernels against the concave. Hence the peakedness of the signal can result higher at low rotor speed. This phenomenon is more evident in the range 950-1150 rpm where the slope of the trend is higher.

Crest (CF) and Impulse (IF) Factors

The CF and IF do not bring further improvements to the correlations obtained through the TK, even if observing the trends depicted in Fig. 4.47 it can be noted that these two features appear more sensitive to the capacity variations.

Approximate Entropy (AppEn)

The AppEn linked to the rotor speed (see Fig. 4.48) show that the regularity of the signal decreases at higher rotor speeds where the threshing noise becomes more relevant.

Loudness and Sharpness

The Loudness and Sharpness metrics are not very sensitive to the changes in rotor speed. It is worth noting that the Sharpness shows a concavity point around 1150 rpm as done by the RMS calculated for front and rear concave signals. It can be noted that front and rear concave accelerometer signals and the outside microphone one are affected by the global vibration of the entire threshing unit whilst the concave middle radial one is more sensitive to local phenomena happening between the concave and the rotor.

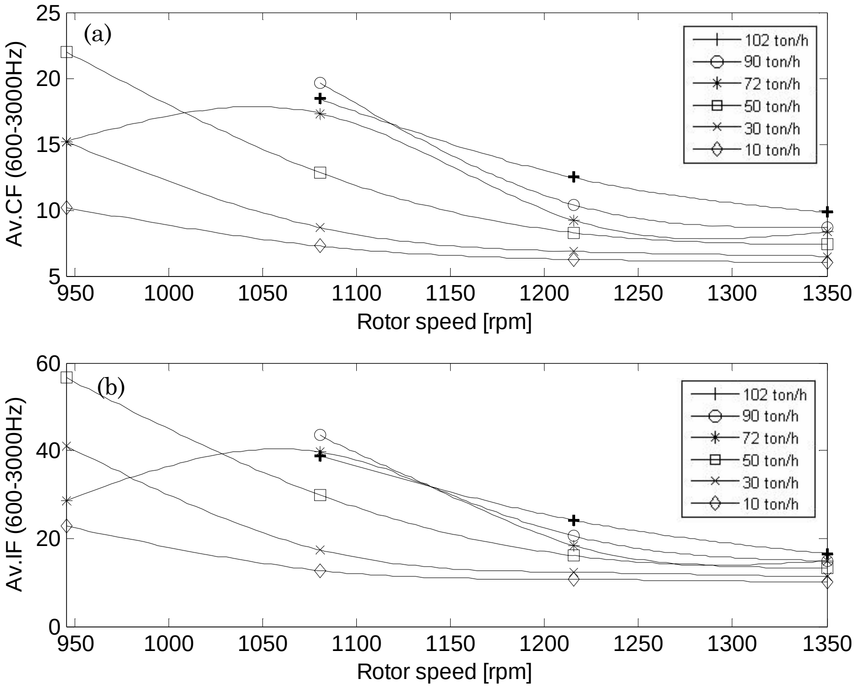

Fig. 4.47 – Av. (a) CF and (b) IF vs. rotor speed - Filtered middle concave radial signal (600-3000 Hz).

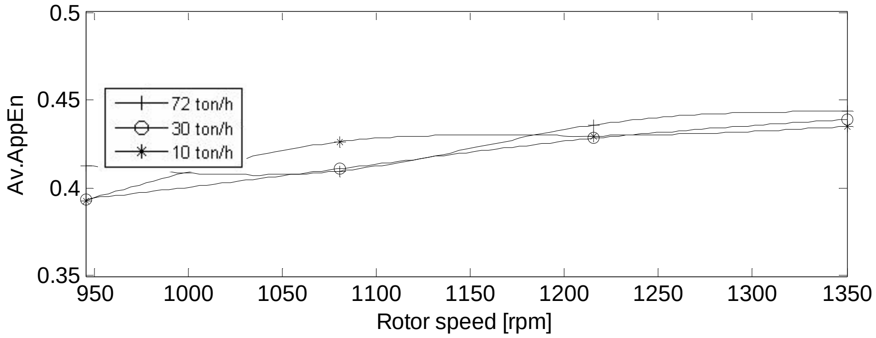

Fig. 4.48 – Av. AppEn vs. rotor speed – Raw concave middle radial signal.

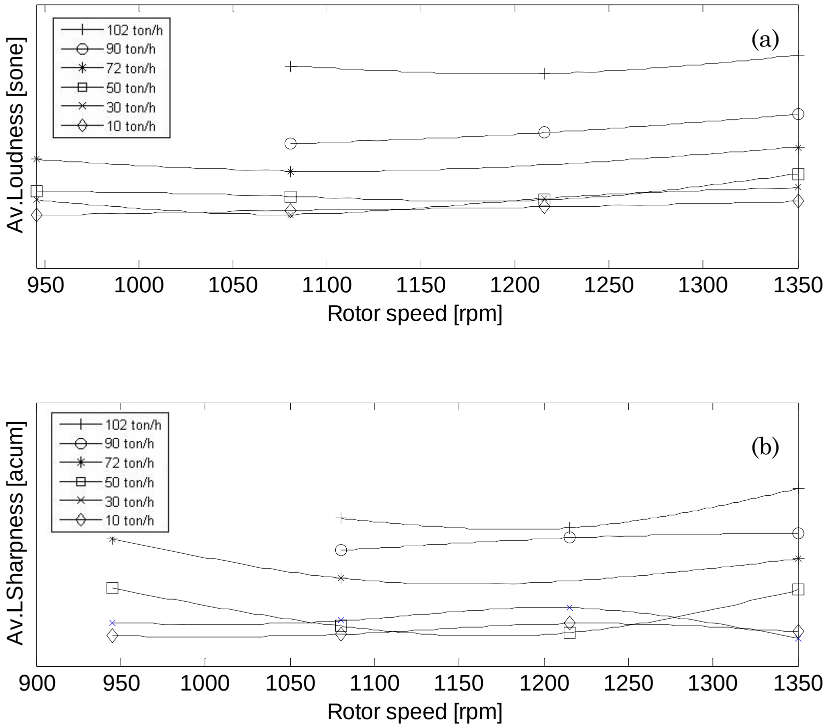

Fig. 4.49 – (a) Loudness and (b) Sharpness of the sound pressure signal measured by the microphone outside the cabin.

4.6.1.4 Influence of the moisture

One of the goals of the field tests is to evaluate if the crop processed is affected by moisture. This can be achieved through the vibro-acoustic analysis. As it is well known the moisture does not permit a good separation of the kernels from the straw causing lower efficiency performance of the threshing process. In order to evaluate the influence of the moisture several runs were performed before the sunset (LM: Low Moisture) and others after the sunset (HM: High Moisture) when the degree of moisture is much higher. Table 19 reports the range of variation of the Overall (OA) Levels (A) for all the microphone signals. It indicates that:

- the threshing microphone signal presents the highest amplitude: it is the most sensitive to the presence of the moisture with an OA increase of 5-10 Pa for the test carried out after the sunset;
- the separation microphone is still sensitive to the presence of moisture but less strongly than the threshing microphone signals;
- the outside microphone is insensitive to the changes in crop conditions.

Based on the experiments we may say that the kernels in HM conditions generate more noise when impact the other kernels and the concave.

Fig. 4.50 depicts the OA (A) values for two fixed segmented signals obtained in LM and HM conditions. The high differences in OA(A) between the two conditions are very clear for both threshing and separation microphones. This kind of plot can be taken as a reference by the user for the on-line evaluation of the degree of moisture affecting the crop during the field operations.

In this sense, the microphones mounted inside the threshing unit can be considered useful transducers for this purpose. It is also can be noted that the outside microphone still remains insensitive to such a local problem confirming what previously found.

Table 19 – Microphone signals: influence of misture.

RMS OA(A) ranges [Pa]	LM	HM
Threshing microphone	12-17	17-27
Separation microphone	6-10	8-13
Outside microphone	2-3	2-3

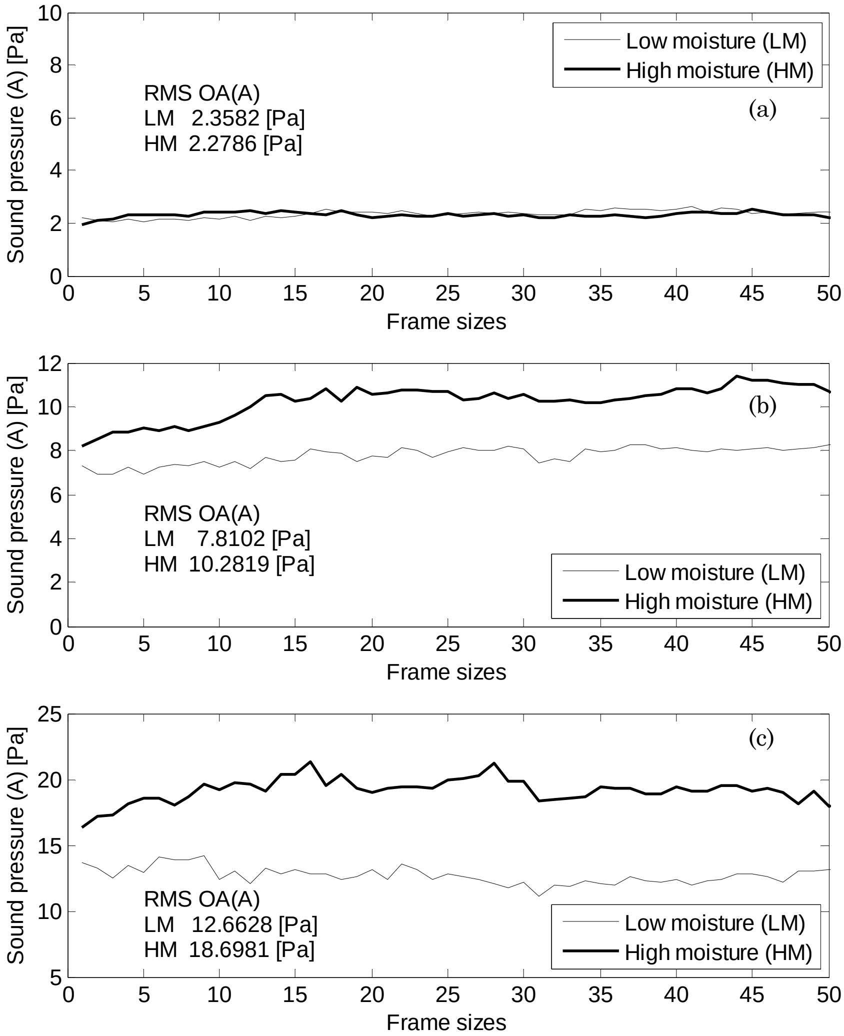

Fig. 4.50 – Sound pressure signals weighted A in LM and HM conditions: (a) outside, (b) separation, (c) threshing microphone.

4.6.1.5 Influence of the grain to straw ratio

The grain to straw ratio is a way to indicate the total length of the plant cut by the machine during the threshing operations. Each plant is composed by straw and the ear of the crop (in this case the crop processed is grain).

If the length of the plant is higher than the normal the grain to straw ratio is lower because the amount of grain is lower in proportion to the length of the straw. On the other hand, if the length becomes lower the grain to straw ratio increases.

Fig. 4.51 – Plant: ear of the crop and straw.

The effect of the grain to straw ratio over the threshing performance could be evaluated analyzing the concave middle radial vibration signals. In particular the RMS values have been extracted and compared for two kinds of crop with normal and short grain to straw ratio.

From Fig. 4.52 it can be observed that all the signals registered with normal grain to straw ratio show higher RMS values than the ones measured with shorter ratio. It is worth noting that the increase of the grain to straw ratio means that the amount of kernels that excite the concave becomes higher in proportion to the amount of straw processed. As a consequence higher excitation of the concave can be obtained processing plants with higher grain to straw ratios.

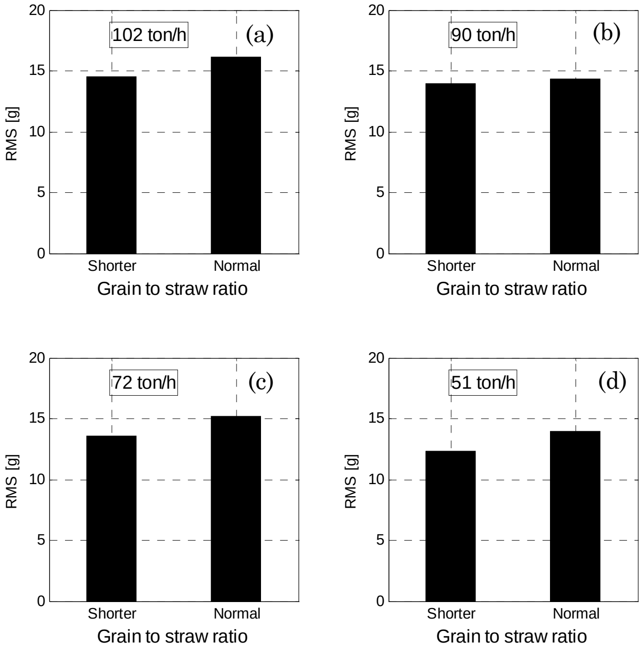

Fig. 4.52 – RMS value of the concave middle radial vibration signal: influence of the grain to straw ratio at (a) 102 ton/h, (b) 90 ton/h, (c) 72 ton/h, (d) 51 ton/h.

4.6.2. Feature extraction for efficiency parameters prevision

This Section is devoted to the research of some good correlations between the features previously calculated and some efficiency parameters. The aim is to investigate the possibility to predict the process efficiency by means of on-line sound and vibration measurements. The exact regression model calculation for each correlation is not the aim of this research.

The efficiency parameters try to numerically describe the efficiency of the threshing process. Some of the threshing efficiency parameters have been obtained directly from measurements (i.e. losses), others from probability function calculations (i.e. distribution of the crop over the threshing zone).

As previously mentioned the total threshing process is given by two sub-processes: threshing and separation. During the first part of the process in correspondence of the threshing zone, the kernels are separated by the straw ear. However some other kernels remain attached to the straw: this amount of kernels is threshed within the separation zone.

The performance of threshing mechanism is expressed by the **threshing efficiency** and the **separation efficiency**.

The threshing efficiency is the percentage of the threshed kernels calculated on the basis of the total kernels entering the threshing mechanism. The kernels that are not threshed give the so-called **threshing loss**. The **separation efficiency** of the rotors is defined as the percentage of the kernels separated in the threshing zone of the rotor, to the total kernels in the crop entering the threshing mechanism. So, the kernels that are not threshed in the threshing zone give the so-called **separation loss**. It is worth noting that in this case the terms "threshing losses" and "separation losses" are not directly linked with both threshing and separation zones of the rotor. The total amount of threshing and separation losses give the so-called **total loss**.

All these kinds of loss are measured as the ratio of their weight over the weight of the crop threshed and collected in the bins under the threshing unit: the loss is therefore measured in percentage.

After the threshing and separation processes, the kernels and MOG fall over the cleaning section formed by three sieves: upper, medium and lower sieve. During the cleaning process the crop is moving from the upper sieve, close to the front of the machine, towards the medium and lower sieves, close to the rear. More to the front they fall on the upper sieve, more time spend there, improving the cleaning. Hence, the distribution of the crop over the total length of the cleaning zone (formed by the upper, medium and lower sieves) is thus an important parameter to understand if the crop is more distributed towards the front having more time to be cleaned. In order to quantify this effect the crop is collected in containers under the machine and the relative amount of the mass in each row of containers can be considered a good indicator for the distribution.

For each of these containers there are 2 values: the gross value (the grain and the MOG) and the net value (only grain).

To extract more information a statistical distribution is fitted on the mass distribution. The beta distribution seems to be suited for this goal. It can be expected that the local deposit of material to be zero at the front, to increase fast to a maximum and to have a slow decline towards the end. All of this can be modelled with a Beta distribution.
The Probability Density Function (PDF) of the Beta distribution is:

$$f(x;\alpha,\beta)=\frac{x^{\alpha-1}(1-x)^{\beta-1}}{\int_0^1 u^{\alpha-1}(1-u)^{\beta-1}du}=\frac{\Gamma(\alpha+\beta)}{\Gamma(\alpha)\Gamma(\beta)}x^{\alpha-1}(1-x)^{\beta-1}= \tag{4.2}$$
$$=\frac{1}{B(\alpha,\beta)}x^{\alpha-1}(1-x)^{\beta-1}$$

Parameter estimation uses the following formulas. Let $\overline{x}=\frac{1}{N}\sum_{i-1}^{N}x_i$ be the sample mean and $\upsilon=\frac{1}{N}\sum_{1}^{N}(x_i-\overline{x})^2$ be the sample variance.

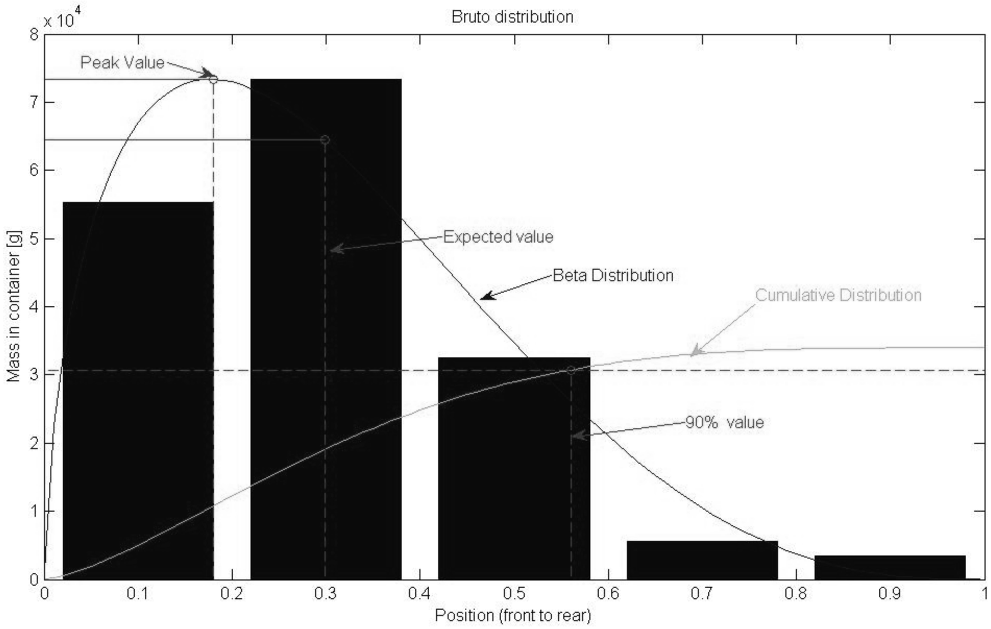

Fig. 4.53 – Distribution of the gross content of the containers at the cleaning position. A beta function has been fit on this data.

By means of this expressions it is possible to estimate the PDF parameters:

$$\alpha = \bar{x}\left(\frac{\bar{x}(1-\bar{x})}{\upsilon}-1\right) \tag{4.3}$$

$$\beta = (1-\bar{x})\left(\frac{\bar{x}(1-\bar{x})}{\upsilon}-1\right) \tag{4.4}$$

Using the previous formulas, a beta distribution has been fit on the mass distribution for the different containers. Several parameters can be extracted from this Beta distribution.

Fig. 4.53 shows the gross mass distribution of a typical run depicting the Beta distribution and the cumulative distribution. The peak value of the distribution, the expected value (i.e. the centre of gravity of the distribution) and the 90% position before which 90% of the material has been deposited can give a qualitative assessment for the mass distribution. The higher the value, the more to the rear the material gets deposited giving the cleaning less time to perform its function.

The same distribution can be obtained from the net mass distribution but it has been verified that there is a linear relation between the parameters extracted from the net and the brute mass distribution.

Threshing losses

Hereafter the scatter plots obtained to point out the correlations between time vibration features and threshing losses will be reported. From Fig. 4.54 and Fig. 4.55 it can be observed that good correlations exist using RMS and TK values as correlation features. The RMS and TK have been calculated for the signals of all runs carried out independently of the different setting parameters. It can be noted that the increase of the threshing losses can be predicted quite well by a decrease of the RMS and an increase of the TK.

In order to improve the correlations, these two features have been obtained after filtering the concave middle vibration signal in the range 600-3000 Hz. On the basis of the correlations obtained it can be supposed that an increase of concave distance, causing a RMS decrease and a TK increase, could give a bigger amount of threshing losses. After adopting these features as monitoring tools it will be also possible to predict an increase or decrease of the threshing losses.

Total losses

Good correlations with the total losses (i.e. overall amount considering both threshing and separation losses) could be obtained using the AppEn extracted from the concave middle radial vibration signal and the sound quality metrics, Loudness and Sharpness (see Fig. 4.57 and Fig. 4.59), extracted from the sound pressure signals measured by the microphone placed outside the cabin.

It can be noted that all feature values increase when the total loss increases in a logarithmic way. In particular, analyzing the Runs carried out at 1350 rpm with 13 mm concave distance as setting

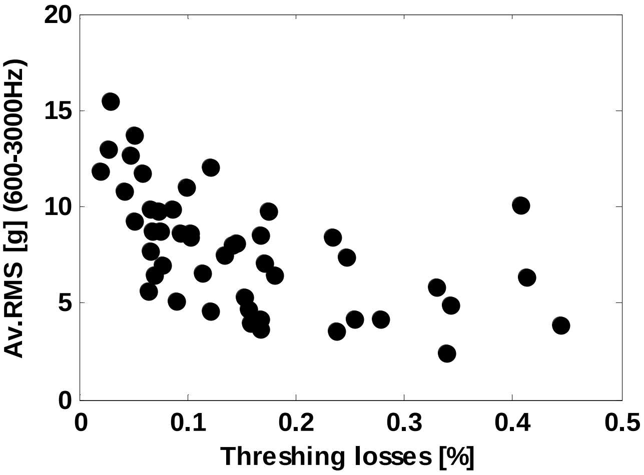

Fig. 4.54 – Concave middle vibration radial signal: Av. RMS values (600-3000 Hz) vs. Threshing Losses.

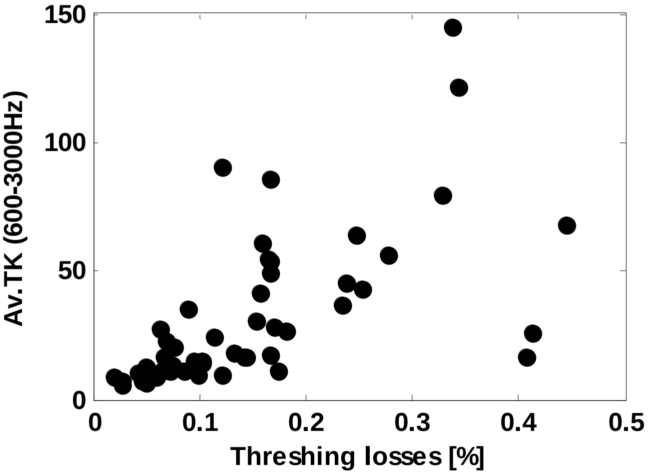

Fig. 4.55 – Concave middle vibration radial signal: Av. TK values (600-3000 Hz) vs. Threshing Losses.

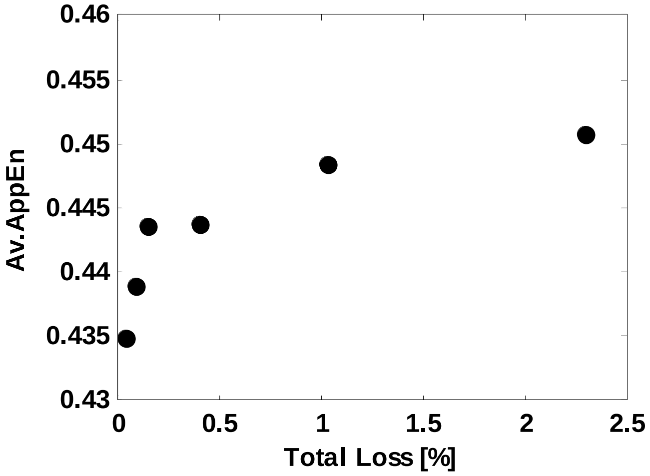

Fig. 4.56 – Concave middle vibration radial signal: Av. AppEn values vs. Total Loss: Runs carried out at 1350 rpm and 13 mm concave distance.

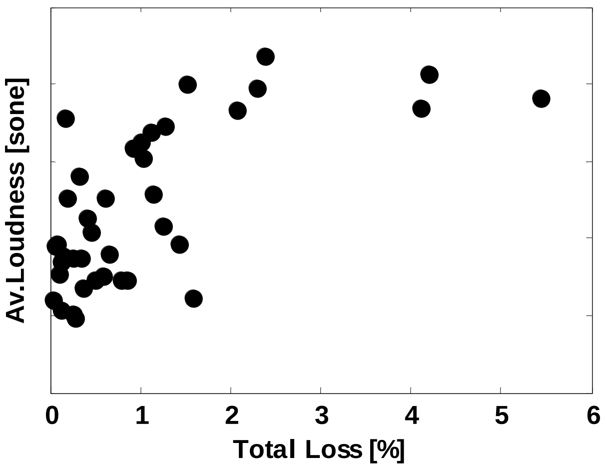

Fig. 4.57 – Sound pressure signal from microphone outside: Av. Loudness vs. Total Loss.

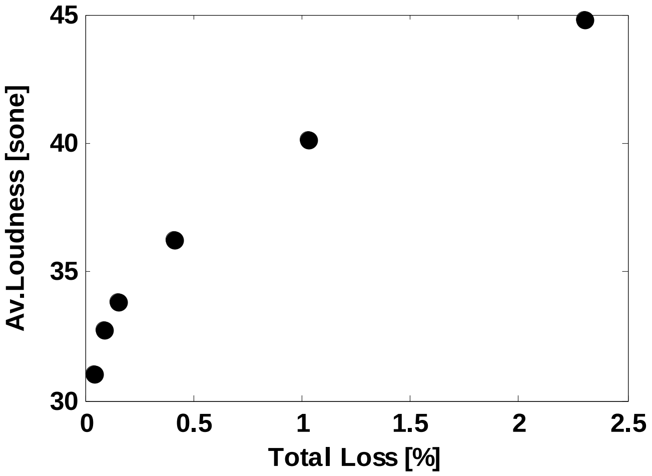

Fig. 4.58 – Sound pressure signal from microphone outside: Av. Loudness vs. Total Loss: Runs carried out at 1350 rpm and 13 mm concave distance.

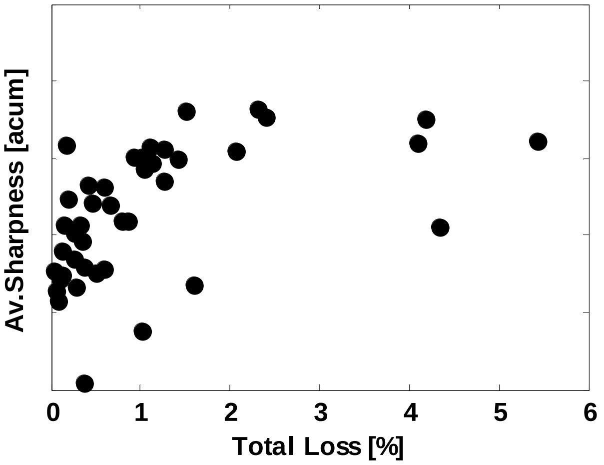

Fig. 4.59 – Sound pressure signal from microphone outside: Av. Sharpness vs. Total Loss.

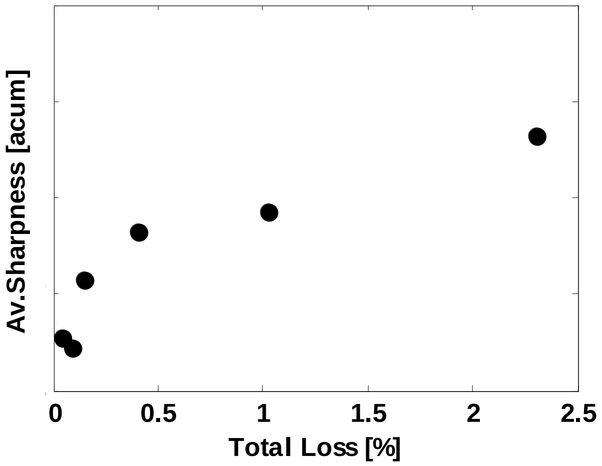

Fig. 4.60 – Sound pressure signal from microphone outside: Av. Sharpness vs. Total Loss: Runs carried out at 1350 rpm and 13 mm concave distance.

parameters, it is possible to obtain clearer correlations. It is found that the AppEn(see Fig. 4.56) and both metrics (see Fig. 4.58 and Fig. 4.60) show a quite linear trend. As a consequence, also these correlations could help the user to get and index of the total losses at the end of the threshing process.

Broken grains (kernels)

The percentage of broken grains (i.e. fractured grain kernels) with have been calculated during tests carried out in field conditions. This quality indicator is calculated through a vision-based sensor that collects images from the crop tank

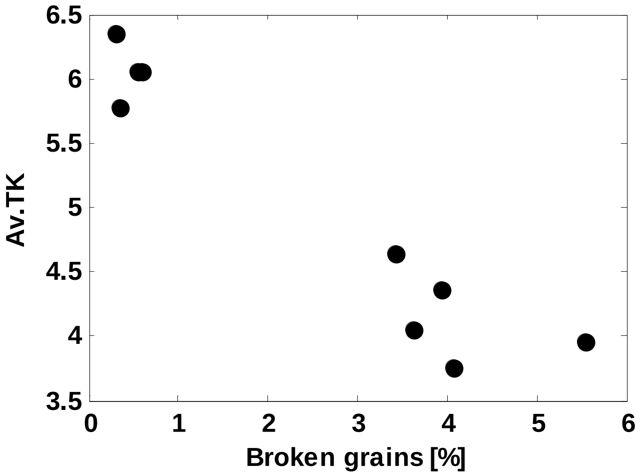

Fig. 4.61 – Field tests: Av. TK vs. Broken Grains.

putting in evidence the kernels cracked by using an image processing algorithm. Fig. 4.61 shows that as the Av. TK increases the amount of broken grain increases.

This behaviour can be interpreted assuming that an increase of the concave distance, indicated by higher TK values, may cause a decrease in the impact force existing between the kernels and the concave giving a low percentage of broken grains.

Distribution of the crop over the cleaning zone

As found for the total losses, the AppEn and sound quality metrics give quite good correlations with the Net 90% position (see from Fig. 4.62 to Fig. 4.66). Here the correlations follows a quite linear trend. This fact means that when the cleaning position before which the 90% of the material has been deposited goes towards the separation zone, the feature values increase. Therefore higher feature values may say a lower cleaning process efficiency.

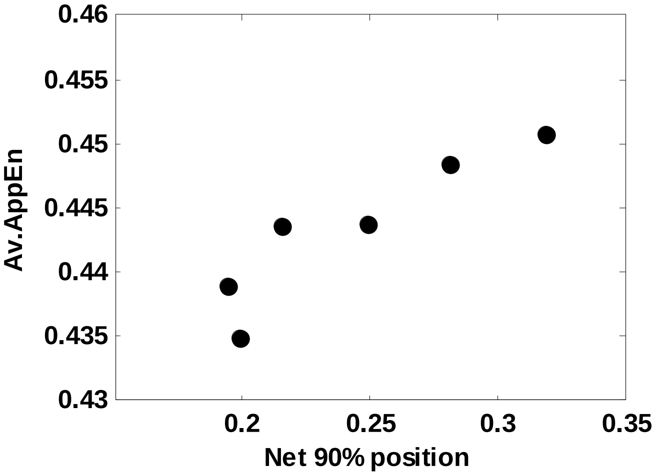

Fig. 4.62 – Concave middle vibration radial signal: Av. AppEn values vs. Gross 90% position: Runs carried out at 1350 rpm and 13 mm concave distance.

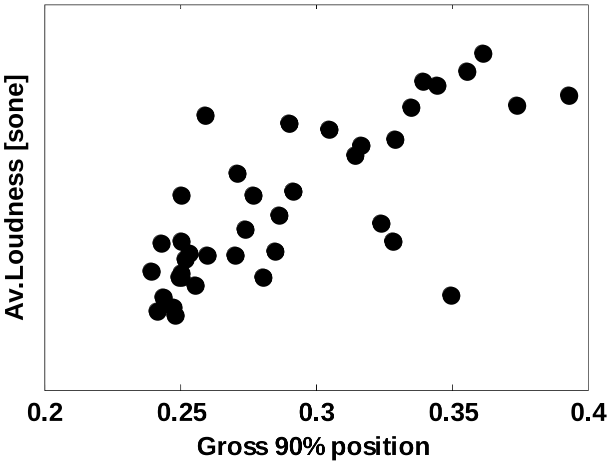

Fig. 4.63 – Sound pressure signal from microphone outside: Av. Loudness vs. Gross 90% position.

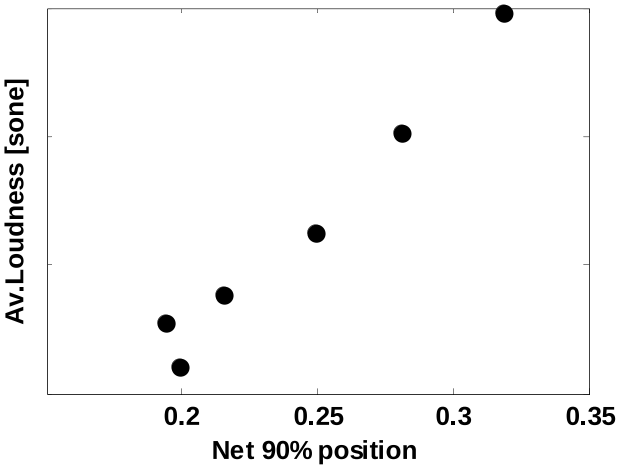

Fig. 4.64 – Sound pressure signal from microphone outside: Av. Loudness vs. Net 90% position: Runs carried out at 1350 rpm and 13 mm concave distance

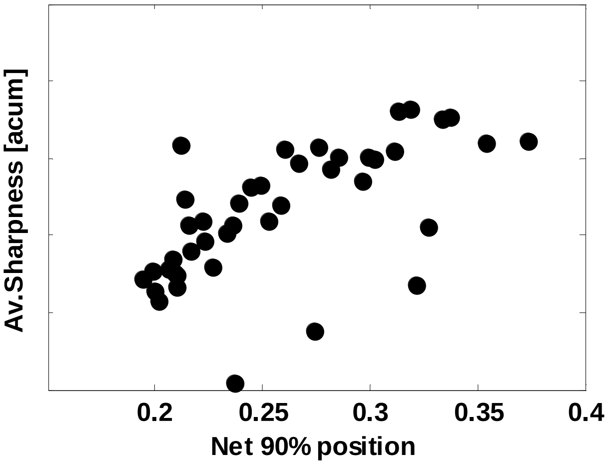

Fig. 4.65 – Sound pressure signal from microphone outside: Av. Sharpness vs. Net 90% position.

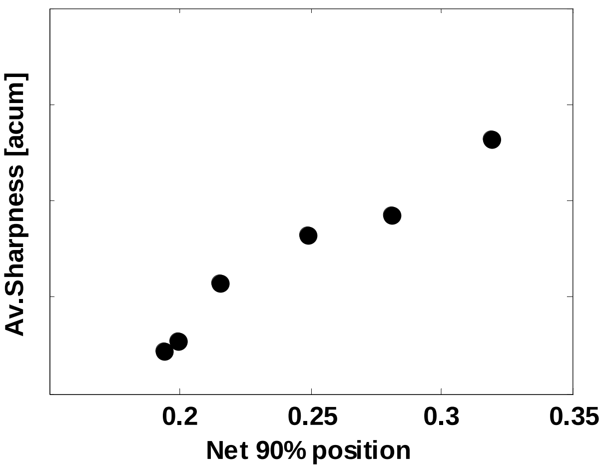

Fig. 4.66 – Sound pressure signal from microphone outside: Av. Sharpness vs. Net 90% position: Runs carried out at 1350 rpm and 13 mm concave distance.

4.7 Extraction of non stationary components: use of Discrete Wavelet Transform (DWT) for filtering purposes

This part deals with the decomposition of the concave middle radial signal in different frequency levels by means of the DWT technique in order to extract the frequency band with the maximum time domain kurtosis value (TK). The purpose is to find an optimal frequency band where we are able to better analyze the peakedness of the concave signal and evaluate how it changes varying the concave distance. This could be assumed as a practical way to understand how the concave distance affects the threshing of the kernels over the concave that is one of the principal threshing mechanisms.

As mentioned in Chapter 2, the DWT technique provides a multi-resolution representation of signals with different time-frequency scales. The calculation is based on the Mallat's algorithm (or pyramid algorithm) and it is implemented in Matlab. This is a very practical filtering algorithm that enables the wavelet transform to be computed in the form of a discrete wavelet transform. As previously said one can look at Mallat's algorithm either as a way of calculating wavelet coefficients at various scales or as a filter bank for processing discrete-time signals. The pyramid algorithm operates on a finite set of input data whose length is an integer power of two. These data are passed through two convolution functions that essentially act as filters.

In the present study, the vibration signal will be decomposed into 9 levels that contain 8 detail coefficients and 1 approximated coefficient. The frequency band of each wavelet level is given by

$$f = 2^j \left(\frac{F_s}{N} \right) \tag{4.5}$$

and the maximum frequency is:

$$f_{\max} = \frac{F_s}{2} \tag{4.6}$$

where f is the higher frequency limit of the frequency band represented by the level j; F_s is the sampling frequency and N is the

Table 20 – Different levels of wavelet analysis

Wavelet Level	Frequency band [Hz]	Center Freq. [Hz]
0 (A9)	0-5,86	2.93
1 (D9)	5,86-11,72	8.79
2 (D8)	11,72-23,44	17.58
3 (D7)	23,44-46,87	35.15
4 (D6)	46,87-93,75	70.31
5 (D5)	93,75-187,5	140.62
6 (D4)	187,5-375	281.25
7 (D3)	375-750	562.5
8 (D2)	750-1500	1075
9 (D1)	1500-3000	2250

number of data points in the input signal (here set as $N = 2048$ and $F_s = 6000$ Hz).

Table 20 summarized the nine frequency bands and the centre frequency of each level in which the signal has been decomposed. The original signal is given by the summation of the approximation at level 9 and all the first nine levels.

The Symlet mother wavelet has been chosen because of its high degree of symmetry can be used to extract the impulsive components of the signal. In order to verify the reliability of the decomposition one detail has been compared with the bandpass filtered signal in the same detail: it can be noted that a low loss of information can be achieved (see Fig. 4.67).

The decomposition algorithm was applied at each concave radial signal for all the runs independently by the machine settings. Then, the Temporal Kurtosis (TK) is calculated for each wavelet decomposition level. As shown by Fig. 4.68 it is found that level 8 (containing frequencies within the range 750-1500 Hz) show the highest TK for all the runs tested. The Spectral Kurtosis (SK) approach was not considered useful since it is affected by the problem related to the choice of the analyzing window. Moreover the implementation of the kurtogram is not so straightforward in processing a big number of runs.

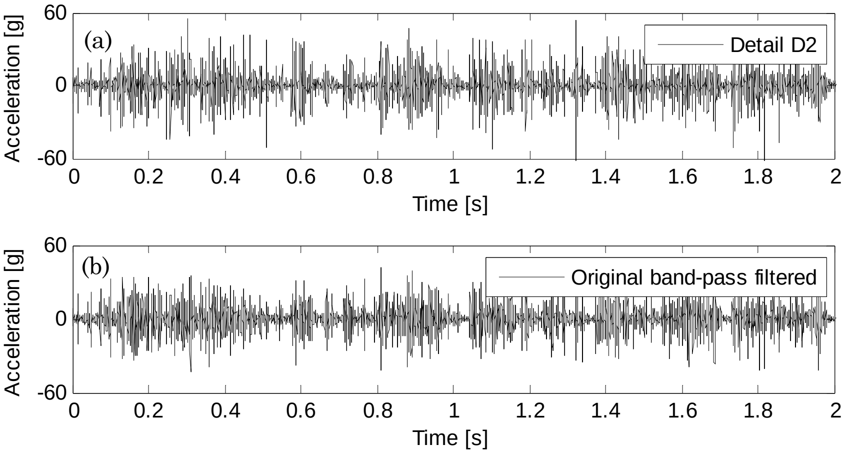

Fig. 4.67 – Concave middle radial signal: comparison between (a) detail D2 obtained after DWT multiresolution analysis and (b) filtered signal in the range 750-1500 Hz

The application of the STFT-based SK to a concave middle radial signal is illustrated in Fig. 4.69 showing the biasing of the SK estimation using different window lengths. It has to be remarked that the DWT technique is not applied to localize singular frequency components with high precision but to determine a frequency range of interest for a big number of runs with a low computational burder.

Once the DWT has revealed the detail level with the highest TK value, the goal is to filter all the signals in this frequency range, calculate the TK and evaluate the effect of the concave distance over the TK of the filtered signal: an improvement of the correlation can be expected.

Hence, assuming the result obtained from DWT as reliable, we can filter all the signals in the 750-1500 Hz frequency range and calculate the Av. TK.

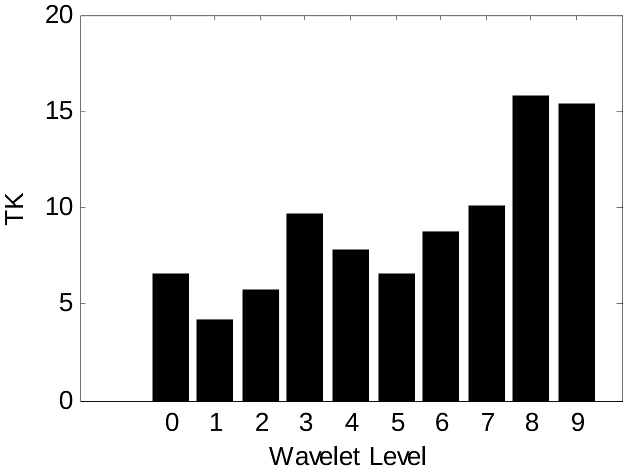

Fig. 4.68 – Typical TK for different wavelet levels.

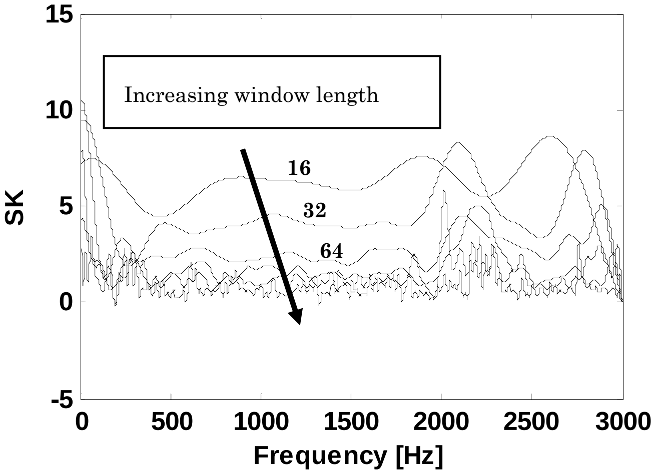

Fig. 4.69 – SK: effect of the window length.

Comparing the correlations obtained with respect of concave distance for both raw and filtered signals it is observed that all the trends show a minor dispersion still presenting the same good correlations (see Fig. 4.70 (b)).

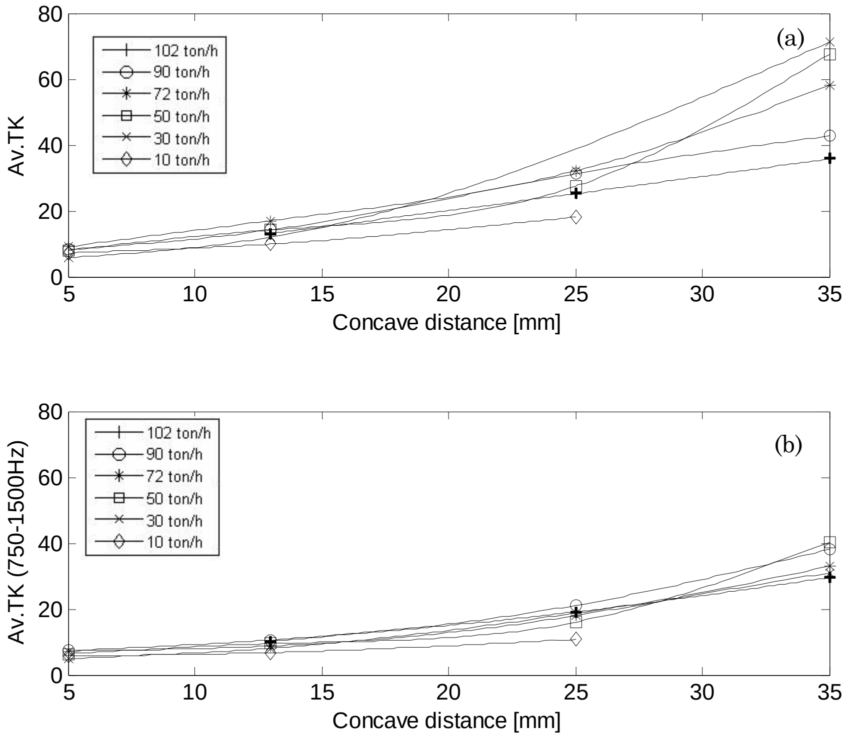

Fig. 4.70 – Influence of the concave distance: Av. TK calculated for (a) raw signal, (b) signal filtered in the range 750-1250 Hz.

In other words we may say that the correlations obtained after filtering the signal are not dependent on the capacity settings. Hence, it is possible evaluate the effect of the concave over the peakness of the signals for all capacity settings.

Therefore, filtering the signal in a proper band before the feature extraction could be considered a good approach to improve the correlations between the features and the operational parameters.

4.8 Evaluation of the rasp bar actions using the TSA of the vibration and sound pressure signals

As mentioned in the previous Chapter 2 time synchronous averaging is a common method adopted in rotating machinery analysis. By synchronising the sampling of the vibration signal with the rotation of a particular shaft and evaluating the ensemble average over many revolutions with the start of each frame at the same angular position, a signal - called Time Synchronous Average (TSA) – is obtained. This signal contains only the components which are synchronous with the revolution of a selected rotating shaft. As a matter of a fact this method strongly reduces the effects of all other sources the noise taking the advantages of the averaging power.

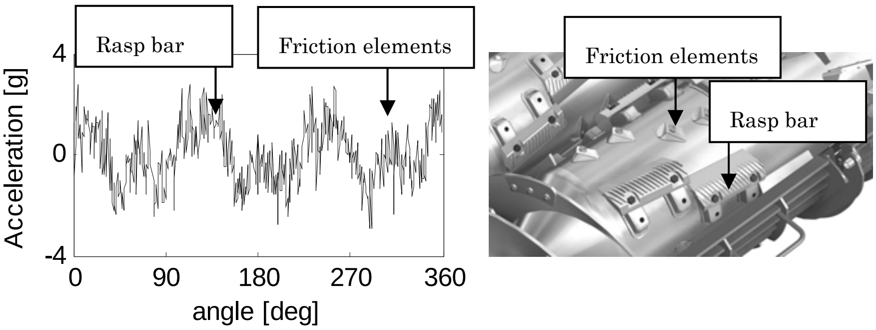

Fig. 4.71 – TSA of the concave middle tangential vibration signal: effects of the rasp bars and friction elements.

It will be show hereafter the analysis of the TSA carried out averaging 100 angular records extracted from the concave middle tangential vibration signal and the threshing microphone signal, taking 512 points for each revolution. In order to compute the TSA a second test investigation was needed in which a tachometer signal was used to get the rotor revolution reference in order to synchronise the records. It is worth noting that the reference phase is not the same for different runs and that only the concave middle tangential signal was available during the second investigation.

The TSA analysis is carried out for the following purposes:

- validate the achievements obtained through the time and frequency analyses;
- evaluate the effects of the capacity and concave distance over the TSA signal properties;

- evaluate how the rotor speed irregularities are influenced by changes in concave distance.

It is worth noting that the TSA vibration signal does not consider the contribution of the “operational” noise due to the threshing turbulence.

Fig. 4.71 shows that the TSA of the concave middle tangential signals is able to visualize the interactions not only among the rasp bars and the concave but also among the friction elements and the concave itself. As a matter of a fact, the TSA depicts three higher peaks due to the rasp bar actions and three lower peaks due to the friction elements actions. As it is illustrated in Fig. 4.71 two friction elements are placed in the vane between to adjacent rasp bars. This is the reason of the behaviour shown by the TSA that depicts six peaks for each rotor revolution.

The FFT of the TSA presented in Fig. 4.72 (b) put in evidence these characteristic periodicities: the third order and the first two harmonics assume higher amplitudes. This behaviour confirm what found by means of the previous frequency analysis. Fig. 4.72 (c), illustrates the Phase Modulation (PM) of the TSA. This quantity can be considered as an useful tool to visualize the speed rotor irregularities. Moreover it will be possible to understand which is the effect of the concave distance over the speed irregularities that can be influence the crop distribution and, consequently, the quality of the threshing process.

It has to be mentioned that normally the frequency demodulation technique is effective for mono-component signal. This approach can be used here since the third order component of the TSA seems to be the most relevant.

Observing Fig. 4.72 (c) it can be noted that the unwrapped PM clearly indicates when the instantaneous rotor speed is increasing or decreasing: when the slope of the PM trend is negative the rotor speed is decreasing. By this fact, it is clearly evident that the rotor speed decreases when the friction elements interact with the concave.

Subsequently, we can obtain the Instantaneous Frequency information by means of the PM differentiation. The Instantaneous Frequency (Inst. Freq.) is able to point out the instantaneous rotor speed fluctuations. From Fig. 4.72 (d) it can be observed that high fluctuation peaks can be observed during the transitions between the increasing and decreasing of the instantaneous rotor speed.

Concerning the TSA of the threshing microphone signal (see Fig. 4.73) it can be noted that it is not able to points out the friction element interactions with the concave but only the rasp bar effects. Because of this phenomenon, the FFT shows only a high peak corresponding to the third order component.

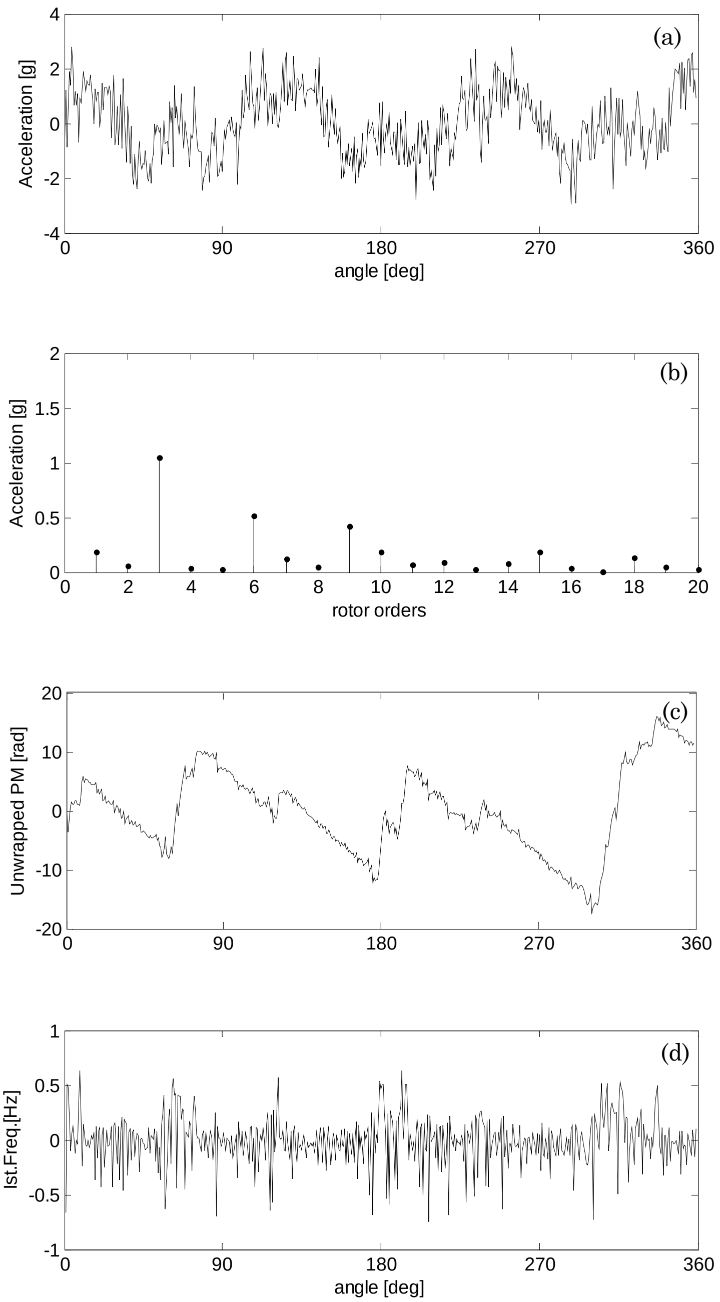

Fig. 4.72 – Concave middle tangential vibration signal: (a) TSA, (b) FFT of TSA, (c) Unwrapped Phase Modulation (PM) of TSA, (d) Instantaneous Frequency of TSA.

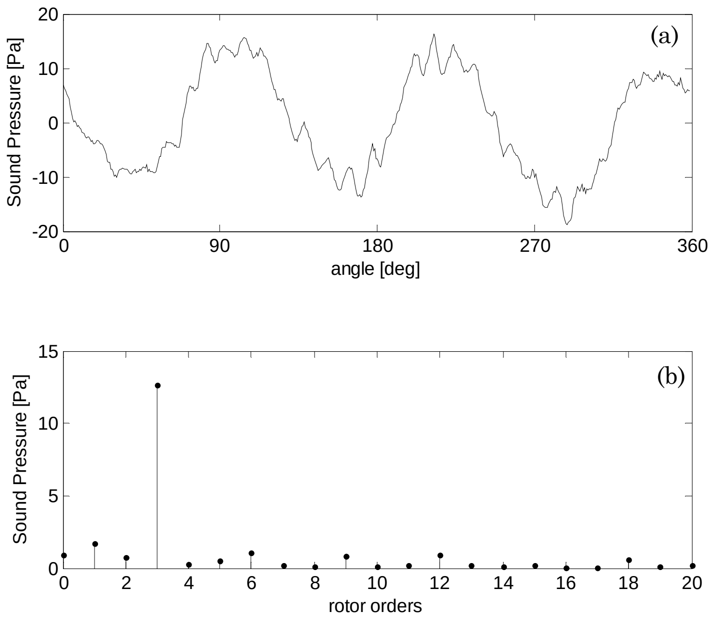

Fig. 4.73 – Threshing microphone signal: (a) TSA, (b) FFT of TSA.

Fig. 4.74, Fig. 4.75, Fig. 4.76 and Fig. 4.77 show the effect of capacity and concave distance variation over the TSA behaviour.

It is shown that at high capacities the TSA of the threshing microphone signal is less sensitive to the variations of the concave distance. In fact the amplitude of the peaks due to the rasp bar effects is not affected by any variation. On the other hand, the TSA of the vibration signal is sensitive to the concave distance variation: the effect of the friction elements become to be neglecting at higher concave distances. At higher concave distances the amplitude of the peaks due to friction element interactions become comparable with the amplitude of the peaks due to the rasp bar effects. These peaks decrease in amplitude as the concave distance increases.

At low concave distances the peaks due to the friction elements are clearly recognizable within the TSA signal.

At low capacities both microphone and accelerometer signal TSA's change their behaviour switching from 25 to 35 mm concave distances. The peaks due to the rasp bar actions show the same amplitude for 13 mm and 25 mm and significantly decrease at 35 mm.

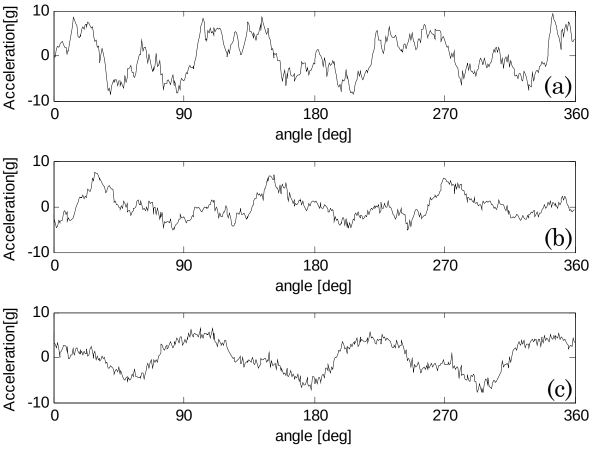

Fig. 4.74 – TSA of the concave middle tangential vibration signal at 90 ton/h capacity: (a) 5 mm, (b) 13 mm, (c) 25 mm concave distances.

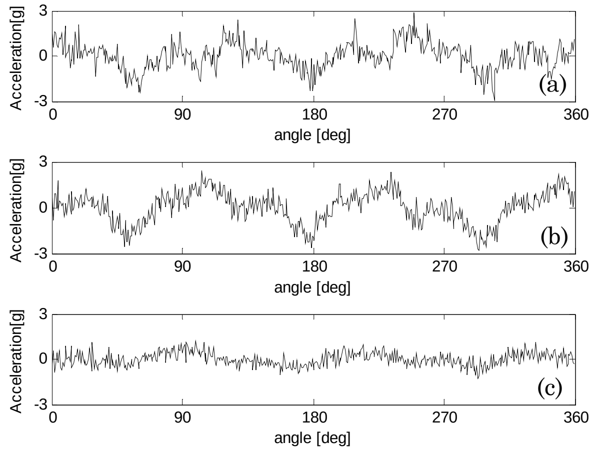

Fig. 4.75 – TSA of the concave middle tangential vibration signal at 51 ton/h capacity: (a) 5 mm, (b) 13 mm, (c) 25 mm concave distances.

It is not possible to separate the effects of the rasp bars from the effects of the friction elements at higher concave distances.

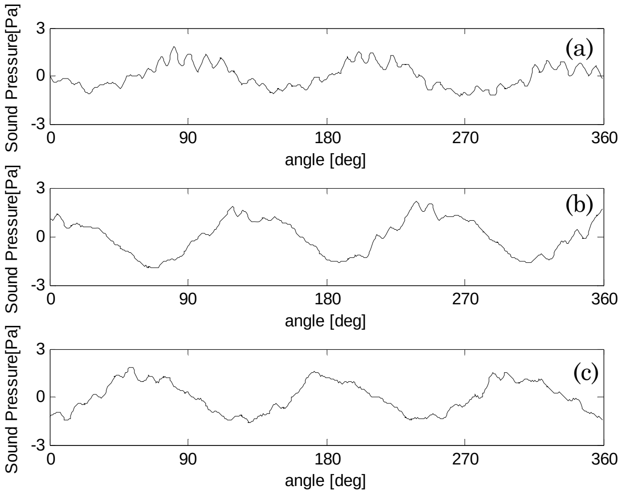

Fig. 4.76 – TSA of the threshing microphone signal at 90 ton/h capacity: (a) 5 mm, (b) 13 mm, (c) 25 mm concave distances.

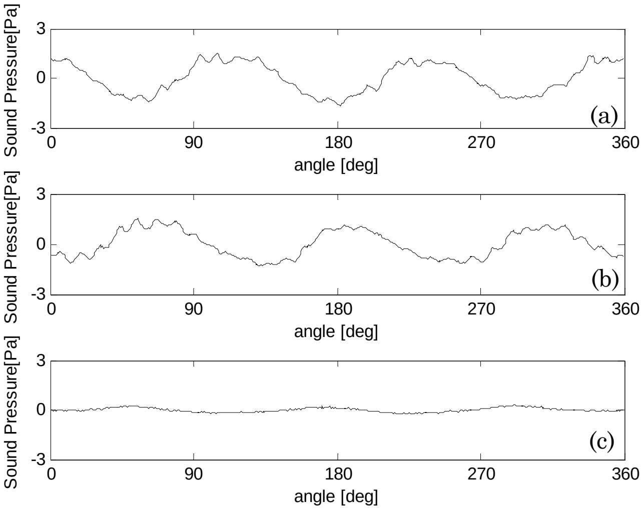

Fig. 4.77 – TSA of the threshing microphone signal at 51 ton/h capacity: (a) 5 mm, (b) 13 mm, (c) 25 mm concave distances.

The Skewness of the PM has been calculated in order to investigate if some correlations exist between the irregularities of the rotor speed and the concave distance variations: no significant results have been obtained.

Since its capability in detecting both rasp bar and friction element interactions the accelerometer signal can be considered as the most reliable in evaluating the local phenomena happening between the rotor and the concave.

Chapter 5
CONCLUSIONS

The topic of this thesis is the development and the implementation of advanced vibration processing techniques for machine condition monitoring and diagnostics with two fields of applications: the quality control of I.C. engines by means of cold tests, and the monitoring and control of harvesting processes. In the first field, the use of several signal processing tools as a means for the monitoring and the diagnosis of assembly faults in diesel engines through the cold test technology has been evaluated. In the second field, the problem of analysing the existing relationships between the harvesting process of a non-conventional harvesting machine and its vibration response have been discussed.

In Chapter 2 a general overview of the theoretical background of all the techniques adopted in this thesis has been presented. The choice of the proper domain of analysis and the proper techniques has been made with the aim to apply the correct technique, by taking into account the nature of the signal in hand.

Concerning time domain analysis the capabilities of some metrics that reflect energy (RMS), peakedness (Crest Factor, Temporal Kurtosis and Impulse Factor) and regularity (Approximate Entropy) of a time series have been evaluated. Furthermore the transformation of a time series in a dot polar graph for pattern recognition purposes (SDP method) has been presented as a reliable tool to detect the presence of a faulty condition in a fast and intuitive way. Another approach based on the analysis of the Instantaneous Angular Speed (IAS) of the machine shaft, obtained by using an encoder signal has also been evaluated. In the particular case of I.C. engines, the IAS is closely related to the fluctuations of the total power acting on the crankshaft. Therefore, it can be considered a potential tool to detect faults related to the pressurization of the cylinders and impacts affecting the crankshaft. Moreover the use of the analytic signal in order to derive the amplitude and frequency modulations of a time domain series, has been outlined. The time-frequency behaviour of a signal has been studied in depth by using the Wigner Ville Distribution (WVD) and Continuous Wavelet Transform (CWT) pointing out the main advantages and drawbacks of both distributions. Moreover the effects of different types of mother wavelet and the purification method in the CWT calculation have been discussed in order to improve its resilience to background noise and its ability in detecting transients and separate close frequencies. All these CWT improvements have been evaluated by means of simulated signals. The CWT discrete version, the so-called Discrete Wavelet Transform (DWT), has been outlined in order to highlight its capabilities in decomposing a signal in different components called approximations and details. In this sense the DWT algorithm can be used as a filter-bank in order to quickly calculate the Temporal Kurtosis of a signal at different scales (frequencies), with the aim of extracting the frequency band mainly characterised by impulsive components. Finally some aspects of the deterministic/stochastic decomposition of a time signal following the cyclostationary theory have been outlined.

Chapter 3 has addressed the use of several signal processing tools for the monitoring and the diagnosis of assembly faults through cold test technology. Three types of faults are considered: rod screws incorrectly pre-loaded, rod without the bearing cap and counter-rotating masses mounted with a phase lag. All these faults cause incorrect engine operations and hits. Firstly, the experimental apparatus concerning the vibration tests has been introduced. Then, the dynamic analysis of a single-cylinder engine has been carried out in order to calculate the piston rod forces against the crankpin. Subsequently a vibration signal model for this type of fault has been introduced. It deals with the cyclostationary model proposed by Antoni in which the signal is subdivided into two main parts: deterministic and non-deterministic. Finally, the acceleration signals acquired from the engine block during a cold test cycle at the end of the assembly line have been analyzed.

For quality control purposes in order to obtain reliable thresholds for the pass/fail decision, a method based on the image correlation of Symmetrized Dot Patterns (SDP) has been proposed. This method visualizes vibration signals in a diagrammatic representation in order to quickly detect the faulty engines in cold tests.

Then, the fault identification has been discussed on the basis of the cyclostationary modelling of the signals. The first-order cyclostationarity is exploited through the analysis of the Time Synchronous Average (TSA). Subsequently, the residual signal has been evaluated by subtracting the TSA from the synchronized signal. Therefore, the second-order cyclostationarity analysis has been developed by means of the Wigner-Ville Distribution (WVD), Wigner-Ville Spectrum (WVS) and Mean Instantaneous Power (MIP). Moreover, Continuous Wavelet Transform (CWT) has been presented and compared with the WVD and WVS. Concerning the faults related to the rod, the analysis carried out on the residual signals shows the presence and the location of the assembly fault. In particular the mean instantaneous power, evaluated over the residual signal, is strongly influenced by the fault location. However, in order to confirm the detection ability of the mean instantaneous power, the WVD and WVS have been also computed here. The CWT (with Impulse mother wavelet) of both TSA and residual signals has also been calculated, showing a less definite angular localisation of the fault than WVD and WVS. In order to improve its angular resolution and its resilience to background noise the choice of the Morlet mother wavelet and the use of two novel methods (i.e. correlation-based purification and TDAS methods) have been evaluated. Finally the capabilities of the Instantaneous Angular Speed signal in detecting the two faults related to the rod have been discussed.

After the analysis performed in Chapter 3 it can be concluded that:

- vibration measurements obtained from diesel engine cold tests can be useful in detecting assembly faults at the end of the production line;
- the percentage of common white pixels between two images obtained using SDP, can be considered as a reliable option for monitoring purposes in order to obtain reliable thresholds for the pass/fail decision;
- the WVS, combining the advantages of the best time-frequency resolution and the cyclic averaging power of the autocorrelation function can be considered the best representation of the time-frequency response within an engine cycle;
- the residual signal is able to give satisfactory indications concerning assembly fault localisation;
- the mean instantaneous power (MIP) can be considered as a powerful and simple tool in vibration based diagnostics; in fact, it is of easy numerical implementation, so interesting results can be obtained without the use of other time frequency techniques of more difficult implementation; the MIP allows accurate detection and localization of the two considered faults related to the piston rod;
- the fault concerning the counter-rotating masses mounted out-of-phase has been detected by the strong increase of the second order component and its harmonics in the TSA;
- concerning CWT representation, the Morlet mother wavelet gives a lower frequency resolution but a better temporal localisation of the time-frequency map, while the use of the coefficient correlation method does not improve the time localisation of the principal engine events; the TDAS method allows some improvements in terms of noise reduction to be obtained and is already able to indicate the fault location, taking advantages of the higher wavelet transformation resolution due to the higher number of samples processed;
- the time synchronous average of the IAS signal is not effective to point out hits or cylinder pressure variations caused by the two faults affecting the piston rod; the residual signal of the torsional

acceleration can be analysed in order to detect some irregularities linked to faulty conditions.

Concerning this first part, further work is needed in order to verify the validity of the above-mentioned procedures in the diagnostics of other kinds of assembly faults. Moreover the capabilities of the implemented techniques applied to microphone signals can also be verified.

Chapter 4 has dealt with the extraction of several features from vibration and microphone signals acquired from the threshing unit of a harvesting machine and the evaluation of their effectiveness in obtaining useful information for the condition monitoring and control of the threshing process. Appropriate features have been extracted from the time domain signals in order to explain the mechanism of the noise and vibration generation during the threshing process. Some correlations between these features and some operational parameters (i.e. capacity, concave distance and rotor speed) have been obtained with the aim of determining the crop distribution is influenced by these parameters. Furthermore, the use of these features to predict some threshing efficiency variables (i.e. total loss, separation and threshing losses, integrity of the kernels, distribution of the crop over the threshing zone) has been discussed. The Discrete Wavelet Transform (DWT) has been used to filter the original signal and its capability in extracting impulsive components from the signal has been verified. Finally, the link between the operational parameters and the rasp bar actions (i.e. mechanical parts fixed to the rotor and used to reinforce the threshing action) have been accurately investigated by means of the angular domain analysis of the vibration signals measured from the rotor concave.

Based on the analyses described above, it is possible to answer the questions posed in Chapter 1:

- the concave middle accelerometer signal is most closely correlated to the threshing process: its spectrum shows the main contributions of the different excitations;
- good correlations have been obtained for the concave middle radial signal, calculating the trends of kurtosis, approximate

entropy and sound quality metrics vs. operational and efficiency parameters; these metrics can be assumed as good indexes that explain the crop distribution between the rotor and the concave and, consequently, the efficiency of the process;

- the features obtained are well-correlated to the sources of excitations, so the vibration signal is able to describe the threshing process physically;
- the DWT technique seems well suited to determine the frequency range with the highest Temporal Kurtosis value (TK); after filtering the raw concave vibration signal the existing correlations between the TK and concave distance are independent of capacity;
- concerning angular domain analysis, the TSA of the concave middle tangential signal is able to visualise the interactions not only between the rasp bars and the concave, but also between the friction elements and the concave itself;
- the Phase Modulation (PM) of the TSA can be considered as a useful tool to visualise the speed rotor irregularities that can influence crop distribution and, consequently, the quality of the threshing process.

Concerning the second part of the thesis, further research could regard the exact determination of the regression model existing between the vibro-acoustic features and the efficiency parameters. Moreover, other experiments could be performed by varying the crop type and the other operational parameters that affect the threshing performances, such as cylinder diameter, concave length and number of rasp bars.

References

[1] Braun S, J. 1986, *Mechanical Signature Analysis*. Academic Press, London.

[2] Collacot R. A. 1979, *Vibration Monitoring and Diagnostic*. Wiley, New York.

[3] Mitchell J., S. 1981, *Machinery Analysis and Monitoring*. Penn Well Books, Tulsa,.

[4] Wowk V. 1991, *Machinery Vibration Measurement and analysis*. McGrae Hill.

[5] Natke H. G., Cempel C. 1977, *Model-aided Diagnosis of Mechanical Systems: Fundamental Detection, Localisation, Assessment*. Springer Verlag, Berlin.

[6] Lyon R. 1987, *Machinery noise and diagnostics,* Butterworths, Boston.

[7] Jardine, A. et al.., 2006, A review on machinery diagnostics and prognostics implementing condition-based manteinance. *Bulletin of the American Meteorological Society, 20(2006).*

[8] Martin, N., 2007, Advanced Signal Processing and condition monitoring session, keynote address. in *Proceedings of the Second World Congress on Engineering Asset Management and the Fourth International Conference on Condition Monitoring 2007, Harrogate, UK, 11-14 June 2007.*

[9] McFadden P.D. 1987, Examination of a technique for the early detection of failure in gears by signal processing of the time domain average of the meshing vibration*, Mechanical Systems and Signal Processing, 1:173–183.*

[10] McFadden P.D. 1986, Detecting fatigue cracks in gears by amplitude and phase demodulation of the meshing vibration.

Journal of Vibration, Acoustics, Stress, and Reliability in Design, 108:165–170.

[11] W. J. Wang and P. D. McFadden, Application of wavelets to gearbox vibration signals for fault detection, *Journal of Sound and Vibration, 192:927–939, 1996.*

[12] Randall R. B. A new method of modelling gear faults, *Journal of Mechanical Design, 104:259–267, April 1982.*

[13] Randall R. B., Antoni J., and Chosaard S. The relationship between spectral correlation and envelope analysis in the diagnostics of bearing faults and other cyclostationary machine signals, *Mechanical Systems and Signal Processing, 15 (5):945–962, 2001.*

[14] Dalpiaz G., Rivola A. Rubini R. 2000. Effectiveness and Sensitivity of Vibration Processing Techniques for Local Fault Detection in Gears. *Mechanical Systems and Signal Processing*, 14(3), 387-412.

[15] Rubini R., Meneghetti U. 2001. Application of the envelope and wavelet transform analyses for the diagnosis of incipient faults in ball bearing, *Mechanical System and Signal Processing*, 15(2), 287-302.

[16] El-Wardanay T.I., Gao D., Elbestawi M. A., 1996. Tool condition monitoring in drilling using vibration signature analysis. *International Journal of Machine Tools and Manufacture*, 36(6), 687-711.

[17] Jantunen E., 2002. A summary of methods applied to tool condition monitoring in drilling, *International Journal of Machine Tools and Manufacture,* 42, 997-1010.

[18] Rehorn Adam G., Sejdic E,, Jiang J., 2006. Fault diagnosis in machine tools using selective regional correlation, *Mechanical Systems and Signal Processing* 20, 1221-1238.

[19] Kimmich F., Schwarte A., Isermann, R. 2005. Fault detection for modern Diesel engines using signal and process model-based methods. *Control Engineering Practice,* 13, 189-203.

[20] Thomas J., Dubuisson B., Dillies-Peltier M. A. 1997, Engine Knock Detection from Vibration Signals using Pattern Recognition. *Meccanica*, 32, 431-439.

[21] Molinaro F., Castanie F., 1995. Signal processing pattern classification techniques to improve knock detection in spark ignition engines, *Mechanical Systems and Signal Processing*, 9(1), 51-62.

[22] Li W., Gu F., Ball A. D., Leung A. Y. T., and Phipps C. E., 2001, A study of the noise from diesel engines using the Indipendent Component Analysis, *Mechanical Systems and Signal Processing* 15(6) 1165-1184

[23] Antoni J., Daniere J. and Guillet, G. 2002. Effective vibration analysis of ic engines using cyclostationarity. Part I-A methodology for condition monitoring, *Journal of Sound and Vibration*, 257(5), 815-837.

[24] Antoni J., Daniere J. and Guillet G. 2002. Effective vibration analysis of ic engines using cyclostationarity. Part II-New results on the reconstruction of the cylinder pressures, *Journal of Sound and Vibration*, 257(5), 839-856.

[25] Konig D., Boheme F., 1994. Application of cyclostationary and time-frequency signal analysis to car engine diagnosis. In *Proceedings of IEEE International Conference on Acoustic, Speech and SignalProcessing*, Vol. 4, pp. 149-152.

[26] Zouari R., Antoni J., Ille J. L., Willaert M., Watremetz M., Sidahmed M., 2006. Cyclostationarity modelling of reciprocating compressors and valve fault detection. In *Proceedings of the ISMA 2006, Leuven, Belgium.*

[27] Mahjoob M. J., Zamanian A., 2006. Vibration Signature Analysis for Engine Condition Monitoring and Diagnosis. *In* Proceedings of ISMA2006, 18-20 September 2006 Leuven, Belgium.

[28] Da Wu J., Chen Chen J. 2006. Continuous wavelet transform technique for fault signal diagnosis of internal combustion engines, *NDT&E International*, 39, 304-311.

[29] Geng, Z., Chen, J., Barry Hull, J. 2003. Analysis of engine vibration and design of an applicable diagnosing approach, *International Journal of Mechanical Sciences,* 45, 1391-1410.

[30] Tse, P.W., Yang, W., Tam, H. Y. 2004. Machine fault through an effective exact wavelet analysis, *Journal of Sound and Vibration*, 277, 1005-1024.

[31] Liu, B. and Ling, S. F., 1999. On the selection of informative wavelets for machinery diagnosis, *Mechanical Systems and Signal Processing*, 13(1), 145-162.

[32] Geveci, M., Osburn, AW, Franchek MA 2005 An investigation of crankshaft oscillation for cylinder health diagnostics, *Mechanical Systems and Signal Processing,* 19 (5), 1107-1134.

[33] Yang, J., Pu, L., Wang, Z., Zhou, Y. and Yan, X. 2001. Fault detection in a diesel engine by analysing the instantaneous angular speed, *Mechanical Systems and Signal Processing*, 15(3), 549-564.

[34] CNH, “Non conventional harvesting machines – User manual”.

[35] Koen Maertens, “An intelligent feeding system for combine harvesters”, *Internal report CNH* (Zedelgem, Belgium).

[36] Bendat J. S., Piersol A. G., 1971, *Random data: analysis and measurement procedures*, Wiley, New York.

[37] Shin K., Hammond J., 2008, *Fundamentals of signal processing for sound and vibration engineers*, Wiley.

[38] Randall, R. B., 1987, *Frequency analysis,* Bruel & Kjaer.

[39] Hammond, J. K., White, P. R1996, The analysis of non-stationary signals using time-frequency methods, *Journal of Sound and Vibration, Vol. 190(3), pp. 419-447.*

[40] Sun Q. et al., 2004, Pattern Recognition for Automatic Machinery Fault Diagnosis, *Journal of Vibration and Acoustics*, *Vol. 126.*

[41] Pincus M., 1991, Approximation Entropy as a measure of system complexity”, in *Proc. Natl. Acad. Sci. USA*, Vol. 88, pp. 2297-2301.

[42] Yan R., Gao R. X., 2007, Approximate Entropy as a diagnostic tool for machine health monitoring, *Mechanical System and Signal Processing*, *Vol. 21, pp. 824-839.*

[43] Taiyong W. et al., Machinery fault diagnosis based on chaotic oscillator and approximate entropy, *in Proceedings of the Second World Congress on Engineering Asset Management and the Fourth International Conference on Condition Monitoring 2007,* Harrogate, UK, 11-14 June 2007.

[44] Wismer J., Time Domain Averaging Combined with Order Tracking, in *Application Note*, Bruel & Kjaer, Denmark.

[45] Fyfe K. R., Munck D. S., Analysis of computed order tracking, *Mechanical System and Signal Processing*, *Vol. 11(2), pp. 187-205.*

[46] Combet F., Gelman L. 2007, An automated methodology for performing time synchronous averaging of a gearbox signal without speed sensor, *Mechanical System and Signal Processing, 21(2008), 2590-2606.*

[47] Halim B. et al., 2008, Time domain averaging across all scales: A novel method for detection of gearbox faults, *Mechanical System and Signal Processing,* 22(2008*), pp. 261-278.*

[48] Mucchi, E., Vecchio, A., 2008, Acoustical signature analysis of a helicopter cabin in steady-state and run up operational conditions, *Proceedings of ISMA2008, Leuven, Belgium, September 15-17.*

[49] Wu, J. D., Chuang, C. Q., 2005, Fault diagnosis of internal combustion engines using visual dot patterns of acoustic and vibration signals. *NDT&E International, 38, 605-614.*

[50] Shibata, K., Takahashi, A., Shirai, T. 2000, Fault diagnosis of rotating machinery through visualisation of sound signal. *Mechanical Systems and Signal Processing, 14(2), 229-241.*

[51] Gonzalez, R., Woods, R. and Eddins, S., 2004. *Digital Image Processing Using Matlab*. Prentice Hall.

[52] Li, H., Gu, F., Harris, G., Ball, A., Nick Bennettb, Travis, K., 2005, The measurement of instantaneous angular speed, *Mechanical Systems and Signal Processing, 19(2005), 786-805.*

[53] Gu, F., Yesilyurt, I., Lia, Y., Harris, G., Ball, A., 2006, An investigation of the effects of measurement noise in the use of instantaneous angular speed for machine diagnosis, *Mechanical Systems and Signal Processing, 20(2006), 1444-1460.*

[54] Stander C., J., Heyns, P. J., 2005, Instantaneous angular speed monitoring of gearboxes under non-cyclic stationary load conditions, *Mechanical Systems and Signal Processing, 19(2005), 817-835.*

[55] Randall R. B., 2002, State of the art in monitoring rotating machinery. *Proceedings of ISMA2002, Leuven, Belgium, September 16-18, pp. 1457-1478.*

[56] Van der Auweraer, H., et al., 1992, “Spectral estimation of time-variant signal”, in *Proceedings of ISMA17 International Conference on Noise and Vibration Engineering, Leuven, Belgium, pp. 207-223.*

[57] Van der Auweraer, H., et al., 1992, “Analysis of non-stationary noise and vibration signals”, in *Proceedings of ISMA17 International Conference on Noise and Vibration Engineering, Leuven, Belgium, pp. 385-405.*

[58] Torrence, C., 1998, A Pratical Guide to Wavelet Analysis. *Bulletin of the American Meteorological Society, 79(1).*

[59] Peng, Z.,K., Chu, F. L., 2003, Application of the wavelet transform in machine condition monitoring and fault diagnostics: a review with bibliography, *Mechanical Systems and Signal Processing 18(2004), 199-221.*

[60] Newland, E., 1994, Wavelet Analysis, Part I: Theory, *Journal of Sound and Vibration 116(1994), 409-416.*

[61] Newland, E., 1994, Wavelet Analysis, Part II: Wavelet Maps, *Journal of Sound and Vibration 116(1994), 417-425.*

[62] Mallat, S., A wavelet tour of signal processing. Academic Press, 1999.

[63] Lin, J., Zuo, M., J., 2003, Gearbox fault diagnosis using adaptive wavelet filter, *Mechanical Systems and Signal Processing 17(6), 1259-1269.*

[64] Boulahbal, D., Golnaraghi M., F., Ismail, F., 1999, Amplitude and phase wavelet maps for the detection of cracks in geared systems, *Mechanical Systems and Signal Processing 13(3), 423-436.*

[65] Baydar, N., Ball, A., 2003, Detection of gear failures via vibration and acoustic signals using wavelet transform, *Mechanical Systems and Signal Processing 17(4), 787-804.*

[66] Meltzer, G., Dien, N., P., 2004, Fault diagnosis in gears operating under non-stationary rotational speed using polar wavelet amplitude maps, *Mechanical Systems and Signal Processing 18(2004), 985-992.*

[67] Wang, W., J., 1995, Application of orthogonal wavelets to early gear damage detection, *Mechanical Systems and Signal Processing 9(5), 497-507.*

[68] Li, J., Ma, J., 1997, Wavelet decomposition of vibrations for detection of bearing-localized defects, *NDT & International 30(3), 143-149.*

[69] Mahjoob, M. J., Zamanian, A., 2006. Vibration Signature Analysis for Engine Condition Monitoring and Diagnosis. *In* Proceedings of ISMA2006, 18-20 September 2006 Leuven, Belgium, pp. 885-895.

[70] Da Wu, J., Qin Chuang, C., 2005. Fault diagnosis of internal combustion engines using visual dot patterns of acoustic and vibration signals. *NDT&E International 38, 605-614.*

[71] Papoulis, A., 1962, *The Fourier Integral and its applications*. McGraw-Hill, New York.

[72] Wang, W. J., McFadden, P. D., 1996, Application of wavelets to gearbox vibration signals for fault detection, *Journal of Sound and Vibration, 192:927–939, 1996.*

[73] Berri, S., Klosner, J., M., 1999, A new strategy for detecting gear faults using denoising with the orthogonal Discrete Wavelet Transform (ODWT), *in Proceedings of the 1999 ASME Design Engineering Technical Conferences, September 12-15, 1999, Las Vegas, Nevada.*

[74] Lin, J., 2001, Feature extraction of machine sound using wavelet and its application in fault diagnosis, *NDT & International 34(2001), 25-30.*

[75] Smith, C., Akujuobi C., Hamory P., Kloesel K., 2006, An approach to vibration analysis using wavelets in an application of aircraft health monitoring, *Mechanical Systems and Signal Processing 21(2007), 1255-1272.*

[76] D' Elia, G., 2008, *Ph.D. Thesis in Applied Machines,* Fault detection in rotating machines by vibration signal processing techniques*, Universita' di Bologna, Italy.*

[77] Schukin, E.L., Zamaraev, R.U., Schukin, L.I., 2004. The optimization of wavelet transform for the impulse analysis in vibration signals. *Mechanical Systems and Signal Processing, 18, 1315-1333.*

[78] Yang, W., 2007. A natural way for improving the accuracy of the continuous wavelet transform. *Journal of Sound and Vibration, 306, 928-939.*

[79] Tse, P., Yang W., Tam, H. Y., Machine fault diagnosis through an effective exact wavelet analysis, 2004, *Mechanical Systems and Signal Processing, 277(2004), 1005-10024.*

[80] Xiaoli L., 1999, On line detection of the breakage of small diameter drills using current signature wavelet transform. *International Journal of Machine Tools & Manufacture.*

[81] Addison P. S., 2002, *The Illustrated Wavelet Transform Handbook,* Istitute of Physics Publishing, Philadelphia.

[82] Delvecchio, S., Dalpiaz, G., Mucchi, E., 2007, Condition monitoring of marine couplings through vibration analysis techniques, in *Proceedings of the Second World Congress on Engineering Asset Management and the Fourth International Conference on Condition Monitoring 2007, Harrogate, UK, 11-14 June 2007.*

[83] Pachori, R. B., Sircar, P., A new technique to reduce cross terms in the Wigner Distribution. In *Digital Signal Processing, 17:466–474, 2007.*

[84] Gardner, W. A., Cyclostationarity in Communications and Signal Processing, IEEE Press, 1994.

[85] Bonnardot, F., Boustany, R., Ibrahim, A., Sabri, K., Antoni, J., El Badaoui M., Don't ignore non-stationarity: use it to advantage. In *Proceedings of the ISMA 2006, Leuven, Belgium.*

[86] Randall, R. B., Antoni, J., Chobsaard, S., The relationship between spectral correlation and envelope analysis in the diagnostic of bearing faults and other cyclostationary machine signals, *Mechanical Systems and Signal Processing, 15(5), 945–962.*

[87] Konig, D., Boheme, F., 1994. Application of cyclostationary and time-frequency signal analysis to car engine diagnosis. In *Proceedings of IEEE International Conference on Acoustic, Speech and Signal Processing, Vol. 4, 149-152.*

[88] Zouari, R., Antoni, J., Ille J. L., Willaert, M., Watremetz, M., Sidahmed, M., 2006. Cyclostationarity modelling of reciprocating compressors and application to valve fault detection. In *Proceedings of the ISMA 2006, Leuven, Belgium.*

[89] Antoni, J., Bonnardot, F., Raad, A., El Badaoui, M., 2004, Cyclostationary modelling of rotating machine vibration signals, *Mechanical Systems and Signal Processing, 18(6), 1285–1314.*

[90] Antoni, J., 2007, Cyclic spectral analysis in practise, *Mechanical Systems and Signal Processing, 21(2007), 597-630.*

[91] McCormick, A. C., Nandi, A., K., 1998, Cyclostationarity in rotating machine vibrations, *Mechanical Systems and Signal Processing, 12(2), 225–242.*

[92] Antoni, J., 2000, *Ph.D. Thesis*, Contribution of Angular Sampling and Cyclostationarity to the Vibration Analysis and Diagnosis of IC Engines. *National Polytechnic Institute of Grenoble (in French).*

[93] Antoni, J., Randall, R. B., 2006, The spectral kurtosis: application to the vibratory surveillance and diagnostics of rotating machines, *Mechanical Systems and Signal Processing 20 (2) (2006) 308–331.*

[94] Vrabie, V. D., Granjon, P., Serviere, P., 2003, Spectral kurtosis: from definition to application, in *IEEE-EURASIP, Workshop on Nonlinear Signal and Image Processing, Grado, Italy, 2003, June 8–11.*

[95] Vrabie, V. D., Granjon, P., Maroni, C., Benoit, L., 2004, Application of spectral kurtosis to bearing fault detection in induction motors, *in Proceedings of Surveillance 5 Cetim, Senlis, October, 11-13 2004.*

[96] Antoni, J., 2006, The spectral kurtosis: a useful tool for characterising non-stationary signals, *Mechanical Systems and Signal Processing 20 (2006) 282–307.*

[97] De la Rosa, J., Munoz, A. M., 2008, Higher order cumulants and spectral kurtosis for early detection of subterranean termites, *Mechanical Systems and Signal Processing 22 (2008) 279–294.*

[98] Antoni, J., 2007, Fast computation of the kurtogram for the detection of transient faults, *Mechanical Systems and Signal Processing, 21 (2007) 108–124.*

[99] Antoni, J., 2005, Blind separation of vibration components: Principles and demonstrations, *Mechanical Systems and Signal Processing (Ed. Elsevier) 19 (2005) 1166–1180.*

[100] Xianhua, L., Randall, R. B., 2005, Blind source separation of internal combustion engine piston slap from other measured vibration signals, *Mechanical Systems and Signal Processing (Ed. Elsevier) 19 (2005) 1196-1208.*

[101] LMS International, *Hands-on Offline RPM Extraction Rev 7A.*